Magnetic interactions in martensitic Ni-Mn based Heusler systems

Fakultät für Physik

der Universität Duisburg-Essen

(Campus Duisburg)

zur Erlangung des akademischen Grades eines

Doktors der Naturwissenschaften (Dr. rer. nat.)

genehmigte Dissertation von

Seda Aksoy, M. Sc.

aus Ankara

Abstract

In this work, magnetic, magnetocaloric and structural properties are investigated in Ni-Mn-based martensitic Heusler alloys with the aim to tailor these properties as well as to understand in detail the magnetic interactions in the various crystallographic states of these alloys. We choose $Ni_{50}Mn_{34}In_{16}$ as a prototype which undergoes a martensitic transformation and exhibits field-induced strain and the inverse magnetocaloric effect. Using the structural phase diagram of martensitic Ni-Mn-based Heusler alloys, we substitute gallium and tin for indium to carry these effects systematically closer to room temperature by shifting the martensitic transformation. A magneto-calorimeter is designed and built to measure adiabatically the magnetocaloric effect in these alloys.

The temperature dependence of strain under an external magnetic field is studied in $Ni_{50}Mn_{50-x}Z_x$ (Z: Ga, Sn, In and Sb) and $Ni_{50}Mn_{34}In_{16-x}Z_x$ (Z: Ga and Sn). An argument based on the effect of the applied magnetic field on martensite nucleation is adopted to extract information on the direction of the magnetization easy axis in the martensitic unit cell in Heusler alloys. Parallel to these studies, the structure in the presence of an external field is also studied by powder neutron diffraction. It is demonstrated that martensite nucleation is influenced by cooling the sample under a magnetic field such that the austenite phase is arrested within the martensitic state.

The magnetic interactions in $Ni_{50}Mn_{37}Sn_{13}$ and $Ni_{50}Mn_{40}Sb_{10}$ are characterized by using neutron polarization analysis. Below the martensitic transformation temperature, M_s, an antiferromagnetically correlated state is found. Ferromagnetic resonance experiments are carried out on $Ni_{50}Mn_{37}Sn_{13}$ and $Ni_{50}Mn_{34}In_{16}$ to gain more detailed information on the nature of the magnetic interactions. The experimental results in $Ni_{50}Mn_{40}Sb_{10}$ show good agreement with those of density functional theory calculations.

The effect of hydrostatic pressure on the structural and magnetic properties of $Ni_{50}Mn_{50-x}In_x$ ($x=$ 15 and 16) and $Ni_{50}Mn_{40}Sb_{10}$ is studied by temperature-dependent magnetization, calorimetry and polarized neutron scattering experiments. When a magnetic field is applied, M_s of $Ni_{50}Mn_{34}In_{16}$ shifts to lower temperatures by about 10 KT^{-1}, whereas, an applied pressure shifts M_s to higher temperatures by about 4 K $kbar^{-1}$. Polarization analysis shows that antiferromagnetic correlations are particularly enhanced in $Ni_{50}Mn_{34}In_{16}$ on applying pressure.

Kurzzusammenfassung

In dieser Arbeit wurden die magnetischen, magnetokalorischen sowie die strukturellen Eigenschaften Ni-Mn- basierender Heusler-Legierungen mit martensitischer Umwandlung untersucht. Ziel der Arbeit war es, die physikalischen Eigenschaften gezielt durch Modifikationen der Legierungszusammensetzung zu beeinflussen und ein Verständnis der zugrundeliegenden magnetischen Wechselwirkungen in verschiedensten kristallographischen Phasen zu erlangen. Als Ausgangspunkt wurde die Legierung $Ni_{50}Mn_{34}In_{16}$ gewählt. Im martensitischen Zustand wird eine magnetfeldinduzierte Rückumwandlung beobachtet, die mit Dehnungen und einem inversen magnetokalorischen Effekten einhergehen. Unter Benutzung des strukturellen Phasendiagrammes martensitischer Ni-Mn-basierender Heusler-Legierungen wurde Indium durch Gallium und Zinn ersetzt. Ziel war es, die in $Ni_{50}Mn_{34}In_{16}$ beobachteten Umwandlungstemperaturen und die damit einhergehenden Effekte zu Temperaturen nahe Raumtemperatur zu verschieben. Die unter adiabatischen Bedingungen bestimmten magnetokalorischen Eigenschaften wurden mit Hilfe eines neu konzipierten Magnetokalorimeters bestimmt.

Ferner wurden Legierungen der Konzentrationsreihen $Ni_{50}Mn_{50-x}Z_x$ (Z: Ga, Sn, In and Sb) und $Ni_{50}Mn_{34}In_{16-x}Z_x$ (Z: Ga and Sn) hinsichtlich der Temperaturabhängigkeit der Dehnung unter dem Einfluss externer Magnetfelder untersucht. Hierbei wurde der Einfluss des Magnetfeldfeldes auf die Nukleation martensitischer Domänen ausgenutzt. So konnten Informationen über die Richtung der leichten Achse der Magnetisierung erhalten werden. Ergänzend dazu wurden im Detail die Kristallstrukturen unter dem Einfluss eines Magnetfeldes mit Neutronen-Pulverdiffraktometrie untersucht. Hierdurch konnte gezeigt werden, dass die Austenitphase durch Kühlen im Magnetfeld in ihrer Umwandlung gehemmt ist und die Nukleation des Martensits unterdrückt wird.

Mit Hilfe der Analyse polarisierter Neutronen wurden für die Legierungen $Ni_{50}Mn_{37}Sn_{13}$ und $Ni_{50}Mn_{40}Sb_{10}$ die magnetischen Wechselwirkungen untersucht. Es zeigte sich, dass knapp unterhalb der martensitischen Umwandlungstemperatur M_s ein antiferromagnetisch korrelierter Zustand vorliegt. Um weitere detaillierte Informationen über die Natur der magnetischen Wechselwirkungen zu erlangen, wurden für $Ni_{50}Mn_{37}Sn_{13}$ und $Ni_{50}Mn_{34}In_{16}$ Untersuchungen mit ferromagnetischer Resonanz durchgeführt. Damit sind die experimentell gefundenen Ergebnisse in guter Übereinstimmung mit Dichtefunktionaltheorierechnungen, die für die Legierung $Ni_{50}Mn_{40}Sb_{10}$ angefertigt wurden.

Des Weiteren wurden die Auswirkungen hydrostatischer Drücke auf die strukturellen und magnetischen Eigenschaften der Legierungen $Ni_{50}Mn_{50-x}In_x$ (x=15 and 16)

sowie $Ni_{50}Mn_{40}Sb_{10}$ untersucht. Hierzu wurde als Funktion der Temperatur die Magnetisierung und die Wärmetönung bestimmt sowie die Analyse polarisierter Neutronen durchgeführt. Bei Anlegen eines Magnetfeldes wurde für $Ni_{50}Mn_{34}In_{16}$ eine Verschiebung der M_s-Temperatur von -10 KT^{-1} beobachtet. Im Gegensatz dazu verschieben hydrostatische Drücke M_s mit +4 K kbar^{-1} zu höheren Temperaturen und stabilisieren den martensitischen Zustand. Die Analyse polariserter Neutronen zeigte, dass hydrostatische Drücke antiferromagnetische Korrelationen begünstigten.

List of abbreviations

A_f	austenite finish temperature
A_s	austenite start temperature
AF	antiferromagnet or antiferromagnetic
bcc	body-centered cubic
bct	body-centered tetragonal
B_{res}	resonance field ($B_{res} = \mu_0 H_{res}$)
DFT	density functional theory
DSC	differential scanning calorimetry
EDX	energy dispersive X-ray analysis
FC	field-cooled
fcc	face-centered cubic
FH	field-heated
FI	ferrimagnetic
FM	ferromagnetic
FMR	ferromagnetic resonance
M_f	martensite finish temperature
M_s	martensite start temperature
MCE	magnetocaloric effect
MR	magnetoresistance
NSF	non-spin-flip
MSME	magnetic shape memory effect
PM	paramagnetic
R_F	flipping ratio
SF	spin-flip
SMA	shape memory alloys
SME	shape memory effect
SPODI	structure powder diffractometer
SQUID	superconducting quantum interference device
T_C^A	Curie temperature of the austenite phase
T_C^M	Curie temperature of the martensite phase
T_P	premartensitic transition temperature
XRD	X-ray diffraction
ZFC	zero-field-cooled
ZFH	zero-field-heated

List of symbols

a	lattice constant
C	heat capacity
$d\sigma/d\Omega$	differential scattering cross-section
e	elementary charge ($= 1.602{\times}10^{-19}$ C)
e/a	valance electron concentration
H	magnetic field strength
P	polarization vector
q	scattering wave vector
S	entropy
α	shear angle
γ	gyromagnetic ratio
G	Gibb's free energy
$\Delta l/l$	relative-length-change
ΔT_{ad}	adiabatic temperature change
ΔS	isothermal entropy change
ϵ	strain
K	magnetic anisotropy
μ	magnetic moment (μ_B/atom)
μ_B	Bohr magnetron ($= 9.274096{\times}10^{-24}$ J/T)
μ_0	vacuum permeability ($=4\pi \times 10^{-7}$ H/m)
σ_{tw}	twinning stress
σ^{coh}	coherent scattering cross-section (Bragg scattering)
σ^{n}	nuclear spin-incoherent scattering cross-section
σ^{m}	magnetic scattering cross-section
χ''	imaginary part of the ac susceptibility
ω	angular frequency
ω/γ	isotropic resonance field

Contents

1. Introduction

Heusler alloys are named after the German mining engineer and chemist Friedrich Heusler who discovered ferromagnetism in Cu-Mn-Al in which the constituent elements are non-ferromagnetic. Heusler alloys are ternary intermetallic compounds with the stoichiometry X_2YZ, known as "full-Heusler" with $L2_1$ cubic structure, and with the stoichiometry XYZ, known as "half-Heusler" with $C1_b$ crystal structure. Off-stoichiometric compositions in many cases are also referred to as Heusler alloys. In this thesis, the magnetic and structural properties of Ni-Mn-based full-Heusler and off-stoichiometric Heusler alloys will be considered. In full-Heusler alloys, when the Y atom is Mn, the resulting alloy is magnetic. In such Mn-based Heusler alloys, X sublattices are occupied by transition elements, and Z can be one of the elements in group IIIA-VA of the periodic table. At off-stoichiometric compositions, Ni-Mn-based Heusler alloys undergo a martensitic transformation from a cubic austenite phase to a phase of lower crystallographic symmetry.

Some martensitic Heusler alloys can exhibit the magnetic shape memory effect (MSM). In such alloys, an external magnetic field applied in the martensitic state leads to large strains. Such shape memory alloys are promising *smart* materials for technological applications, and recent developments on actuators and sensors emphasize their importance even stronger. Since the discovery of magnetic shape memory in the martensitic Ni_2MnGa Heusler alloy in 1996 [1,2], Ni-Mn-based Heusler alloys have attracted much interest. In Ni-Mn-Ga, the strength of the magnetoelastic coupling in the martensitic state is responsible for large strains in the order of 10% [3], which is considerably larger than those in piezoceramics and magnetostrictive materials showing strain of about 0.2% on applying an electric or magnetic field.

Initial studies on structural and magnetic properties of off-stoichiometric Heusler alloys $Ni_2Mn_{1-x}Z_x$ (Z: In, Sn) were investigated in detail by T. Krenke within the scope of a Ph.D. study [4]. Many of these alloys undergo martensitic transformations and exhibit various magnetic-field-driven properties such as magnetic superelasticity and the magnetocaloric effect [5,6]. Further investigations showed that $Ni_2Mn_{1-x}Sb_x$ alloys are also martensitic and show similar effects [7]. These effects in Heusler-based systems are related to field-induced magneto-structural transformations, in which the structural and magnetic degrees of freedom are coupled to one another.

Magnetic superelasticity is observed when the martensitic transformation temperature shifts to lower temperatures under an applied magnetic field. Application of

magnetic field produces large strains which are caused by field-driven transitions from the matrensitic to the austenitic state.

In 1997, the discovery of the giant magnetocaloric effect (MCE) at room temperature in $Gd_5Si_2Ge_2$ [8] offered a promising development of economical and enviromental-friendly magnetic refrigerants working near room temperature. The refrigerant operates on the principle that the application of a magnetic field adiabatically causes the sample to warm. More recently, the so-called *inverse* MCE has been observed near room temperature in martensitic Ni-Mn-Sn Heusler alloys [9] which cool in a magnetic field applied in the martensitic state.

The development of materials that exhibit large magnetoresistance (MR) is important for many technological applications. Strong changes in the magnetization and in the electrical resistivity are found around the martensitic transformation in Ni-Mn-based ferromagnetic shape memory alloys. In 2006, a large MR effect of about 60% was reported at room temperature [10]. At temperatures lower than room temperature, in the martensitic state, this value increases up to 80%. Several publications can be found that deal with the MR effect in Ni-Mn-based Heusler alloys [11–13].

In addition to their technological relevance, martensitic Heusler alloys are particularly interesting for fundamental investigations on the interplay between their complex crystal structures and their magnetism. Most of the novel properties of martensitic Heusler alloys are related to the martensitic transformation. This naturally stimulates interest in understanding the magnetism of these materials particularly in the transformation region. The observation of exchange-bias in Ni-Mn-based Heusler alloys led to more focus on research on magnetic properties. The presence of exchange-bias suggests that antiferromagnetic coupling is to be expected in the martensitic state although, until now, no significant proof about the nature of magnetic interactions in the martensitic state has been provided [14–16].

To understand the mechanism of these materials and to design magnetic shape memory materials a priority program supported by the Deutsche Forschungsgemeinschaft (SPP1239) and entitled "Change of microstructure and shape of solid materials by external magnetic fields" has been established in 2006 [17]. A close interdisciplinary collaboration is communicated within this program under three main topics: Fundamentals, bulk materials and applications, films and microsystems. The present thesis is prepared within a subproject under fundamentals, and the task is to investigate magnetic, magnetoelastic and dynamic properties of newly designed martensitic Heusler

alloys.

The work presented in this thesis is a study of magnetic, magnetocaloric and structural properties of Ni-Mn-based Heusler alloys. In Section 2, we give a brief introduction on the fundamental background of martensitic transformations, the magnetic shape memory effect and structural properties of Heusler alloys. The magnetocaloric effect is described within thermodynamics. The experimental methods and a short overview of different experimental setups used in this work are described in Section 3. Section 4 presents the experimental results, which are discussed under four main topics. In the first part, methods for tailoring the properties of martensitic Heusler alloys are discussed. The second part deals with the effects of external magnetic field on strain in Ni-Mn-Z alloys (Z: Ga, In, Sn, Sb). Here, a method is presented to estimate the easy magnetization direction using polycrystalline samples, and also the results of neutron diffraction experiments under magnetic field and structural changes related to the applied field are presented and discussed. The third part presents the results on polarized neutron scattering and ferromagnetic resonance. The experiments are carried out to determine the nature of the magnetic interactions in the austenitic and martensitic states of Ni-Mn Heusler alloys. In the fourth part, we study the effect of pressure on the magnetic properties of martensitic Heusler alloys. In particular, we report on the results of pressure-dependent magnetization and polarized neutron experiments under pressure. A conclusion is provided in Section 5.

2.   Fundamental Background

2.1   Martensitic Transformations

Martensitic transformations are solid-state first order structural phase transformations which are displacive, diffussionless and dominated by the strain-energy arising from shear-like displacements. There is no long-range movement of the atoms. They move less than their interatomic distances maintaining their local neighborhood during the phase transition. The first studies on martensitic transformations were undertaken by Adolf Martens on steels at the end of the 19th century. The name "martensite" was used to describe the microstructure found in quenched steels. The gamma phase iron in steel above the critical eutectoid temperature was described as *austenite*, named after Sir William Chandler Roberts-Austen. Other than in steels, martensitic transformations occur in various types of materials such as nonferrous alloys, ceramics, minerals, polymers, etc. Martensite is also the description of the product phase of a martensitic transformation. During the formation of the new product phase from the parent phase (austenite), different regions of the material transform at high velocity so that the transformation occurs in general by nucleation and growth. During nucleation, a new phase develops within the austenite, and an interface is formed between the austenite and the martensite which is parallel to the habit plane and contains areas separated by dislocations or twin boundaries.

In some cases, a volume-change accompanies the phase transition, and this leads to large lattice distortions and tensions. Figure 2.1(a) shows a simple homogenous Bain deformation where the lattice deformation proceeds from fcc to bcc (or bct). This deformation involves the smallest principle strains of about 20% contraction along the z-direction and 12% expansion along x- and y-directions. The lattice distortion occurs by a shear mechanism and causes a degenerate martensitic structure with different oriented variants, known as twinning. Figure 2.1(b) and (c) show an inhomogenous shear performed by twinning and slip with a shear angle α, respectively.

A characteristic feature of a martensitic transformation is the transformation hysteresis. The temperature dependence of various physical parameters such as strain, magnetization, electrical conductivity etc., can be schematically described as in Fig. 2.2. On cooling, the martensitic start and finish temperatures, M_s and M_f, and on heating, the austenite start and finish temperatures, A_s and A_f can be identified as indicated in the graph. Austenite is represented as a square lattice and martensite as
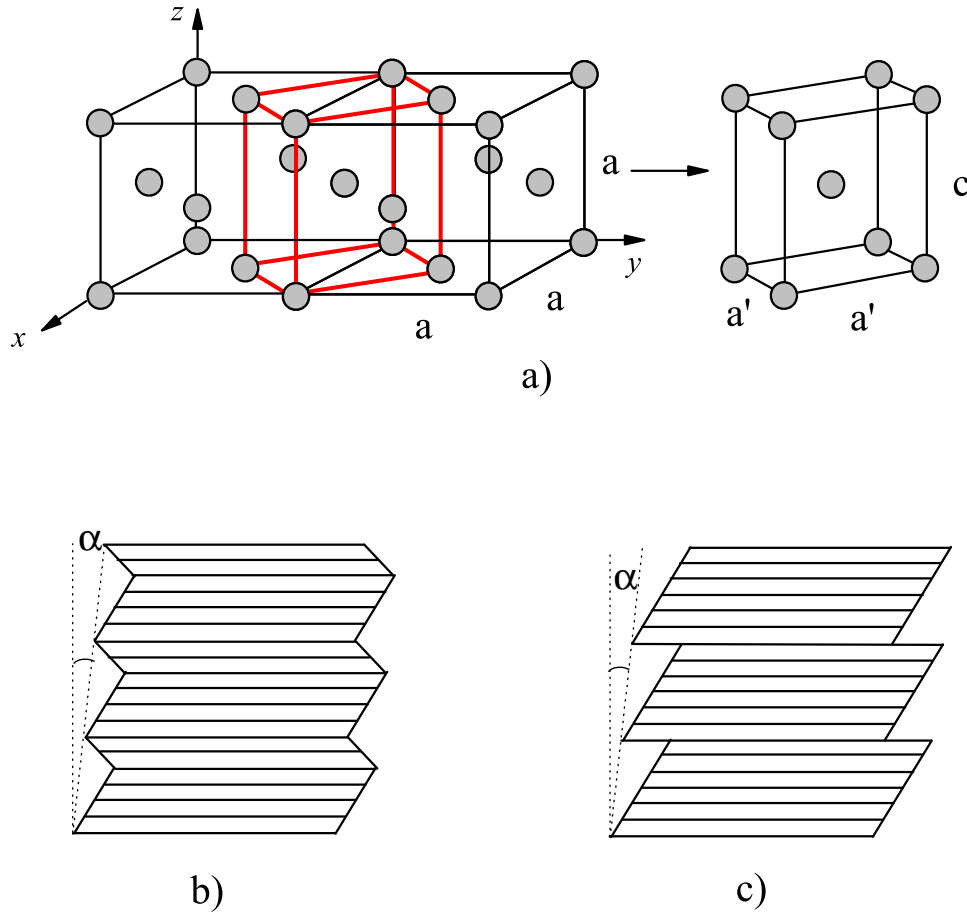
Figure 2.1: (a) The Bain distortion of martensite and the inhomogeneous shear performed by (b) twinning and (c) slip with an angle α.

a rhombic lattice derived from the distortion of austenite. The formation of martensite progresses between M_s and M_f, and in the reverse transformation, austenite formation progresses between A_s and A_f. The width of the hysteresis is given by the difference between A_f and M_s.

In general, the free energy difference at the martensitic transformation is given by,

$$\Delta G^{\text{A}\rightarrow\text{M}} = \Delta G_{\text{C}}^{\text{A}\rightarrow\text{M}} + \Delta G_{\text{NC}}^{\text{A}\rightarrow\text{M}} \tag{1}$$

where $\Delta G_{\text{C}}^{\text{A}\rightarrow\text{M}}$ and $\Delta G_{\text{NC}}^{\text{A}\rightarrow\text{M}}$ are the differences in the chemical free energy and the non-chemical energy, respectively. The latter consists of elastic strain and surface energies [18]. A and M denote austenite and martensite. In the case of twinning, a large part of the strain energy and the interfacial energy is stored elastically in a thermoelastic
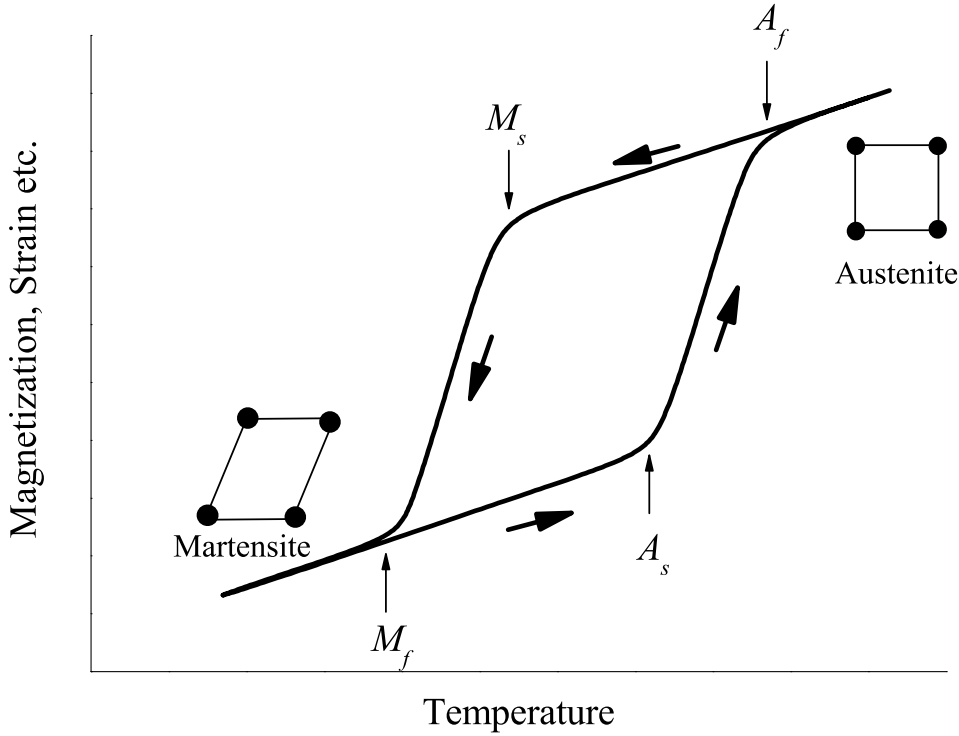
Figure 2.2: Temperature-dependent physical properties for the forward martensitic transformation on cooling and the reverse transformation on heating. Arrows show the direction of cooling and heating. The characteristic temperatures are indicated with vertical arrows: austenite start and finish temperatures, A_s and A_f, martensite start and finish temperatures, M_s and M_f.

transformation, in which case $\Delta G_{\mathrm{NC}}^{\mathrm{A}\rightarrow\mathrm{M}}$ dominates and gives a positive contribution to the total free energy.

Fig. 2.3 shows the temperature-dependence of the Gibb's free energy around a martensitic transformation. T_0 is the thermodynamic equilibrium temperature where the chemical free energies of martensite and austenite are equal. At $T > T_0$, austenite is stable thermodynamically relative to martensite, and at $T < T_0$, martensite is more stable. In the forward martensitic transformation region, $\Delta G^{A\rightarrow M} < 0$, and in the reverse transformation-region, $\Delta G^{M\rightarrow A} > 0$. The difference in free energies between austenite and martensite at M_s is indicated by $\Delta G_{M_s}^{A\rightarrow M}$. The Gibb's free energy of the martensite phase is less then that of the austenite phase below T_0.
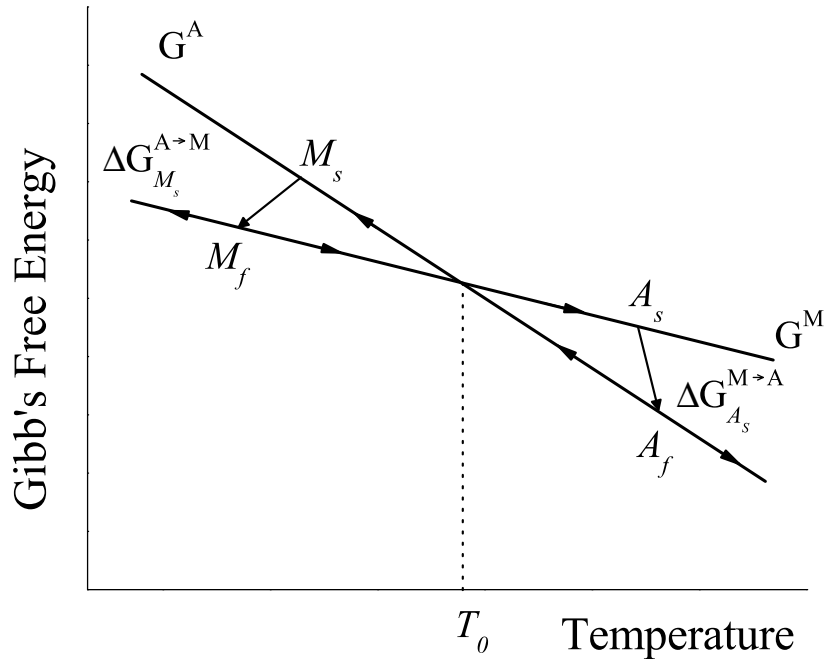
Figure 2.3: Schematic diagram of the Gibb's free energy of martensite (G_M) and austenite (G_A) in the martensitic transformation region.

2.2   Magnetic Shape Memory Effect

The shape memory effect (SME) occurs when a material is deformed mechanically in the martensitic state and regains its original shape when it is heated up to a higher temperature within the austenitic state. Materials known as shape memory alloys (SMA) are able to recover their original shape that they had before the deformation. When the deformation is caused by magnetic field rather than external stress, the materials are named magnetic shape memory alloys.

The magnetic shape memory effect (MSME) occurs in the ferromagnetic martensite phase when an external magnetic field is applied. The martensite phase consisting of multi-variant twin-related domains has a large magneto-crystalline anisotropy, and under an applied field, the structure can be strongly affected so that twins can rearrange or detwinning can occur. These magnetically induced changes can lead to a shape-change of the material. This is shown schematically in Fig. 2.4. When the temperature is lowered to below M_f, the martensitic transformation takes place, and when the tem-
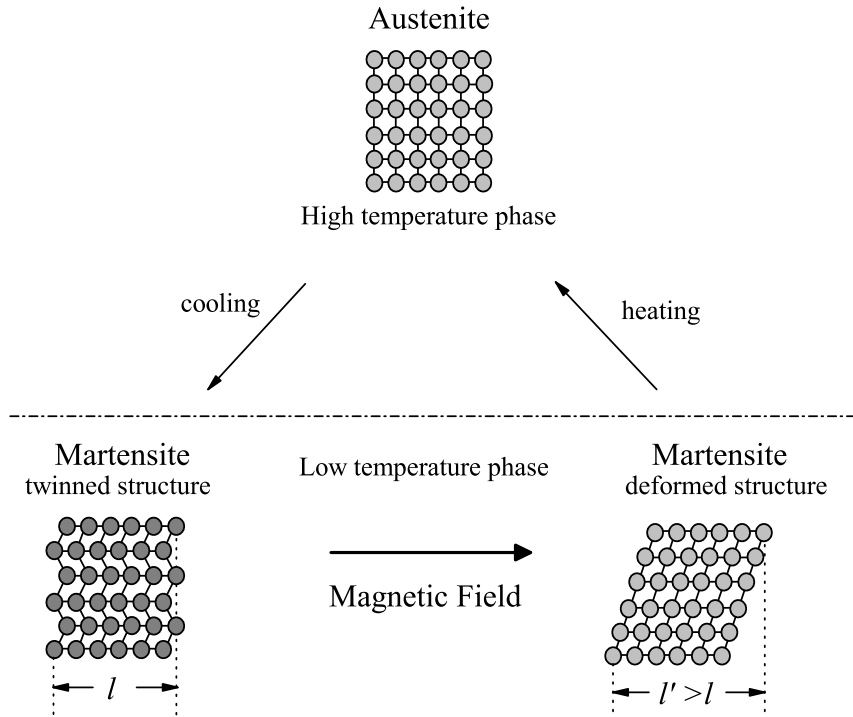
Figure 2.4: Schematic representation of the magnetic shape-memory effect.

perature is raised to above A_f, the reverse martensitic transformation occurs. When a magnetic field is applied to a twin-related martensitic structure for which the magnetocrystalline anisotropy energy of the material is high, the magnetic moments rotate together with the structure to align the easy-axis along the field direction, and the mobile twin boundaries move. As a result, a single variant is formed, and the length of the material increases from l to l'. If the field direction is reversed, the sample regains its original shape with the twinned structure. This is called MSME. On the other hand, when the deformed sample is heated to the austenitic state, the shape is recovered by the reverse martensitic transformation as in the conventional SME.

Basically, a magnetic field induces stress on the twin boundaries as a result of the difference in the Zeeman energies, $\Delta M \cdot H$, between the two variants. Here H is the internal magnetic field and M is the magnetization. To obtain strain, the magnetic anisotropy should be greater than the Zeeman anisotropy energy density difference $K \geq (\Delta M \cdot H)$. If $(\Delta M \cdot H) \gg K$, the magnetic moments in the two variants align with the field and the energy difference vanishes. Under external stress and in a saturating
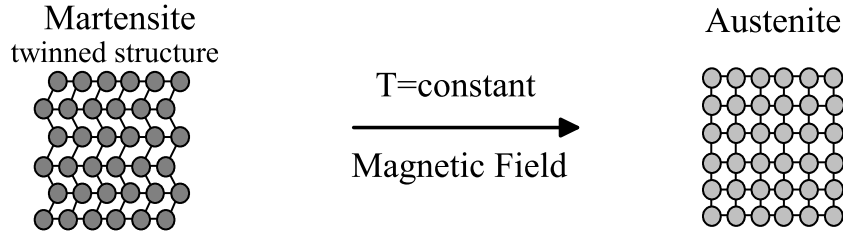
Figure 2.5: Schematic representation of magnetic-field-induced reverse martensitic transformation.

magnetic field, the magnetically induced stress is expressed as [19,20],

$$\sigma_{mag} = \frac{K}{\varepsilon_0} \geq \sigma_{tw} + \sigma_{ext}, \tag{2}$$

where σ_{tw} is the twinning stress and σ_{ext} is the external stress. σ_{ext} is applied in the direction perpendicular to the magnetic field direction. ε_0=1-c/a is the tetragonal distortion where a and c are the lattice parameters of the tetragonal martensite phase. According to equation 2, when the magnetic stress is larger than the zero-field σ_{tw}, the large magnetic field-induced strain can be observed as a result of the higher magnetic anisotropy energy. When the anisotropy is weak, the Zeeman energy difference across the twin boundary is small, and only limited strain can be achieved.

Field-induced strain does not occur only by twin boundary motion. When a material undergoes a structural transformation under an applied external field, large strains can also be obtained. The magnetic-field-induced reverse martensitic transformation is illustrated in Fig. 2.5. When a magnetic field is applied in the martensitic state at a temperature close to A_s, the martensite structure transforms to austenite at constant temperature and, in most cases, it is accompanied by a length-change. This effect is known as magnetic superelasticity (also referred to as pseudo-elasticity). When the magnetic field is removed, the structure reverts to martensite, and the strain is recovered.

The magnetic shape memory effect was first observed in a non-stoichiometric Ni-Mn-Ga single crystal showing 0.2% strain [1]. Later, with single variant Ni_2MnGa crystals, up to 10% strain has been reached at room temperature [21–23]. Compared to these values, the magnetostrictive material "Terfenol-D" ($Tb_{0.33}Dy_{0.67}Fe_2$) shows a

field-induced strain of about 0.24% [24], and industrially used piezoceramics show 0.1% strain [25].

The field-induced reverse martensitic transformation and magnetic superelasticity have been previously reported for polycrystalline $Ni_{50}Mn_{34}In_{16}$ [5]. In this material, applying a magnetic field at 180 K, which is close to A_s, induces a reverse structural transformation. The material partially transforms to austenite at 5 T and 0.15% strain is obtained as a result of the reverse transformation. When the magnetic field is removed, the strain is recovered.

2.3   Structural Properties of Ni-Mn-based Heusler Alloys

In general, the occurrence of the MSME is strongly related to the crystallographic structure in the martensitic state, and there are several related studies on the structure of Ni-Mn-based Heusler alloys. These alloys have a cubic $L2_1$ structure in the austenitic state and display a sequence of intermediate modulated martensite structures appearing at $T < M_s$ with $(c/a) < 1$; and non-modulated tetragonal structures with $c/a > 1$ [26]. On solidifying, Ni_2MnZ (Z: Ga, In, Sn, Sb) Heusler alloys form a disordered bcc phase (A2), and on cooling, they transform to a partially ordered intermediate B2 phase where the Ni atoms occupy the corners of the cubic cell and the Mn and Z atoms occupy randomly the body-centered position. On further cooling, the structure transforms to the $L2_1$ phase, where the Ni atoms occupy the same sublattice, and the other atoms occupy the body centered position with similar atoms as second nearest neighbors. The B2$\rightarrow L2_1$ transition temperature is around 1070 K for Ni_2MnGa.

Fig. 2.6 shows the $L2_1$ structure for Ni_2MnGa with a unit cell parameter a. If the alloy composition is off-stoichiometric ($Ni_{50}Mn_{50-x}Ga_x$) and the alloy undergoes a martensitic transformation, the martensite phase can take up various modulated or non-modulated structures as a result of the decrease of symmetry. The structure depends on the composition of the alloy. At low x, the $L2_1$ structure generally transforms to the $L1_0$ tetragonally distorted structure which can be visualized to occur through a Bain lattice distortion. In the $L1_0$ state, the c-axis of the unit cell is longer than the a'-axis, $(c/a') > 1$ as shown in Fig. 2.6. A variety of modulated martensitic structures have been observed as well as the non-modulated $L1_0$ structure at higher x concentrations [26–29]. In $Ni_{50}Mn_{50-x}Z_x$ (Z: Ga, In, Sn) alloys, the modulated structures are 10M (or 5-layered) and 14M (or 7-layered) monoclinic, but in $Ni_{50}Mn_{50-x}Sb_x$, the 4O orthorhombic structure is observed instead of 10M. These modulated structures are shown in Fig. 2.7
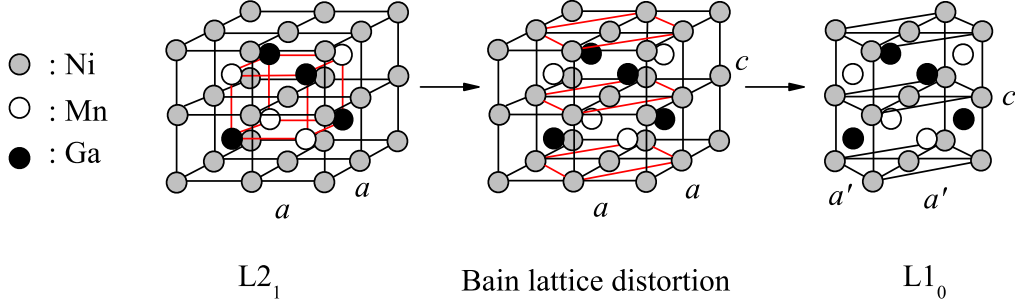
Figure 2.6: The austenitic L2$_1$ and non-modulated L1$_0$ martensitic structure of Heusler alloys for the case of Ni$_2$MnGa. Light grey: Ni; white: Mn; black: Ga. In the L2$_1$ structure, Ni atoms occupy the corners of the unit cell, and the Mn and Ga atoms occupy the body-centered-cubic positions. The L1$_0$ structure is obtained from the L2$_1$ structure, and in the new periodic order, Mn and Ga atoms occupy face-centered positions.

which are formed by shearing the (110) planes along the [1$\bar{1}$0] direction, and the crystal structure can be described either as a long period stacking of close-packed (110) planes or as the periodic shuffling of (110) planes along [1$\bar{1}$0] direction [27,28].

The phase diagram of off-stoichiometric Heusler alloys are shown in Fig. 2.8 for (a) Ni-Mn-Ga, (b) Ni$_{50}$Mn$_{50-x}$In$_x$, (c) Ni$_{50}$Mn$_{50-x}$Sn$_x$ and (d) Ni$_{50}$Mn$_{50-x}$Sb$_x$ [30]. The structural (M_s) and magnetic transition temperatures are plotted as a function of e/a. T_C^A and T_C^M are the Curie temperatures of the austenite and martensite phases, respectively. Above T_C^A, all systems are paramagnetic (PM). As the concentration of the Z-element decreases, ferromagnetic (FM) exchange weakens, and eventually vanishes. M_s increases linearly with increasing e/a (decreasing x) in all systems, and the slope of the curve increases from Ni-Mn-Ga to Ni$_{50}$Mn$_{50-x}$Sb$_x$ (Fig. 2.8 (a)-(d)). The smaller closed circles in Fig. 2.8 (a) indicate the premartensitic transformation temperature T_P which increases linearly with increasing e/a.

In Fig. 2.8 (a)-(c), the structure develops as cubic→10M→14M→L1$_0$ with increasing e/a. In Fig. 2.8 (d), the martensitic state is observed in a narrower e/a-range where mixed 4O and 7-fold modulated structures are found [31–34]. However, some studies report the martensitic structure of Ni$_{50}$Mn$_{50-x}$Sb$_x$ as 10M-modulated [35]. At lowest Z concentrations, the structure is tetragonal non-modulated L1$_0$ in all systems.

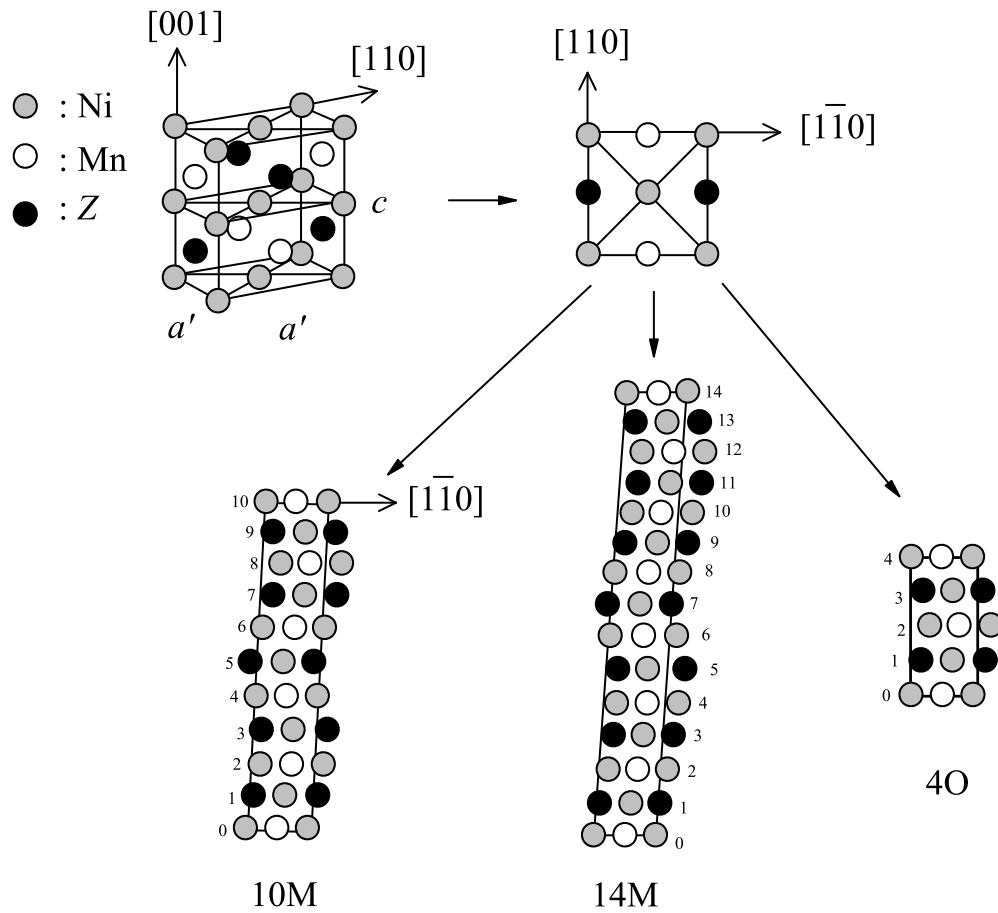**Figure 2.7**: The observed modulated 10M (5M), 14M (7M) monoclinic and 4O orthorhombic martensitic structures in $Ni_{50}Mn_{50-x}Z_x$ (Z: Ga, In, Sn and Sb) alloys. Light grey: Ni; white: Mn; black: Z. The tetragonal non-modulated unit cell with lattice parameters a' and c becomes modulated by shearing or shuffling of the (110) planes along the $[1\bar{1}0]$ direction.
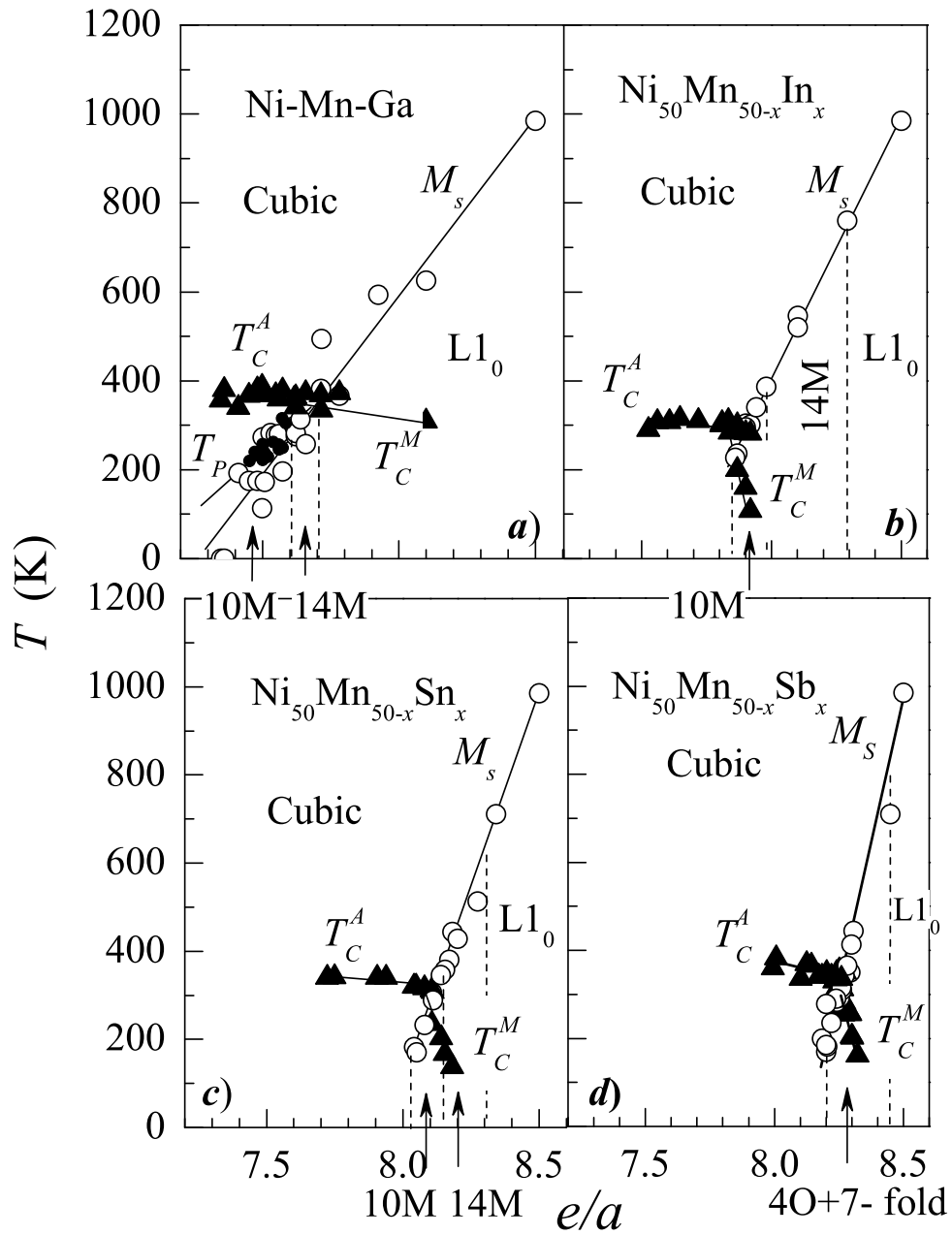
Figure 2.8: Phase diagram of Ni-Mn-Z Heusler alloys with Z as (a) Ga, (b) In, (c) Sn and (d) Sb. The triangles and the circles represent the magnetic and martensitic transformation temperatures respectively. The crystal structure changes with composition and the regions related to the different structures are separated by dashed lines [30].

2.4   Application of Magnetic Shape Memory Alloys

MSM materials have recently been used as actuators to produce mechanical motion
and force. Manufacturing automation, microsurgical instruments, micro-sensors [36],
micro-actuators such as micro-valves [37], and stepper motors are potential application
areas of MSM actuators. Since the material produces motion without any additional
component, the material itself acts as a machine. The structure of a basic MSM actuator
is presented in Fig. 2.9. Typically, the actuating material is aligned with its short c-axis
(easy magnetization axis) along the direction of pre-stress in zero-magnetic field. A
magnetic field is subjected to the MSM material. When the magnetic field is applied
perpendicular to the c-axis, the twin variants reorient such that the short c-axis rotates
parallel to the field direction. This leads to an elongation of Δl.

Magnetic-field-induced strains in MSM single crystalline Ni-Mn-Ga alloys have
reached values of ∼10%, and the response time is less than a millisecond. For this
reason, the Ni-Mn-Ga single crystals are so far the most investigated prototypical mag-
netic actuating materials. The achievable strain is over 4% in grain-oriented polycrystals
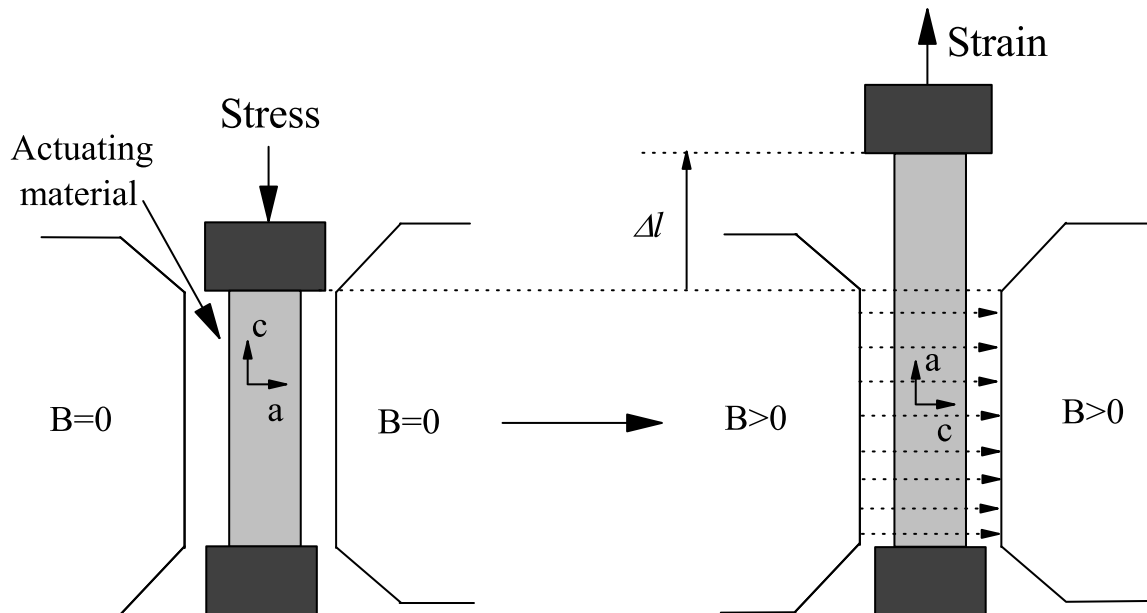
Figure 2.9: Schematic view of a single crystalline magnetic shape memory actuator.

[38]. Ni-Mn-Ga composites [39,40], fibers [41] and textures [42] are also investigated as alternatives to expensive single crystals to overcome some disadvantages related to brittleness, preparation difficulties, and cost. Recently, polycrystalline Ni-Mn-Ga foams have been found to exhibit high magnetic-field-induced strains which are related to the pore size of the foams. When the pore size is smaller than the grain size, a MFIS around 9% is achieved [43]. Magnetic field-induced reorientation has been found in Ni-Mn-Ga free-standing thin films [44–46]. These are expected to find potential applications for linear actuators, sensors and micromotors [47]. Since the new Heusler alloys such as Ni-Mn-In exhibit magnetic superelasticity in the martensitic state, they have also become good candidates for the actuating technology [48].

MSM alloys have also been considered as magnetic refrigerator materials. These alloys exhibit large magnetocaloric effects, and in the following section, the details of this effect is discussed.

2.5   Magnetocaloric Effect (MCE)

Most Ni-Mn-based Heusler alloys undergo a second-order magnetic phase transition at T_C^A and a first-order martensitic phase transition below M_s. Accordingly, they exhibit two types of MCE; a conventional MCE around T_C^A and an inverse MCE around M_s. These two effects are discussed.

2.5.1   Conventional MCE

In general, the MCE is a change of magnetic entropy and temperature of a magnetic material under application of a magnetic field. The MCE was discovered by Warburg in 1881 in iron, which was found to warm under an applied magnetic field [49]. The reversible temperature change caused by magnetizing a paramagnet was first demonstrated by Langevin [50]. Afterwards, adiabatic demagnetization using paramagnetic salts were used to reach low temperatures in the mK range [51–53].

In the process of adiabatic demagnetization for a paramagnet, the entropy can be considered as a sum of two contributions: Entropy related to magnetic ordering and entropy related to lattice vibrations. In the paramagnetic state at T_0, all magnetic moments are aligned randomly by thermal agitation in the absence of a magnetic field. When a magnetic field is applied isothermally, the magnetization increases with preferred orientation of the magnetic moments along the field direction, so that the entropy related to magnetic ordering decreases, and the total entropy decreases since the temperature remains constant. Subsequent removal of the magnetic field under adiabatic conditions raises magnetic disorder to preserve the total entropy of the system. The vibrational entropy decreases causing the temperature of the system to decrease to T_1. In this case, the adiabatic temperature change is defined as $\Delta T_{ad}=T_0\text{-}T_1$.

The MCE occurs around temperatures where rapid changes in the magnetization with respect to temperature are observed. As in PM salts at low temperatures, such rapid changes can be found around first and second-order phase transitions at practically any temperature. Here, the MCE around a second-order phase transition is considered firstly since it resembles the case of the MCE in a PM salt discussed above.

In second-order phase transitions, the first derivative of the thermodynamic potential with respect to temperature or magnetic field gives continues functions, and there is no latent heat related to the transition. The temperature dependence of the total entropy $S(T)$ of a FM material is shown schematically in Fig. 2.10 for a second-order transition
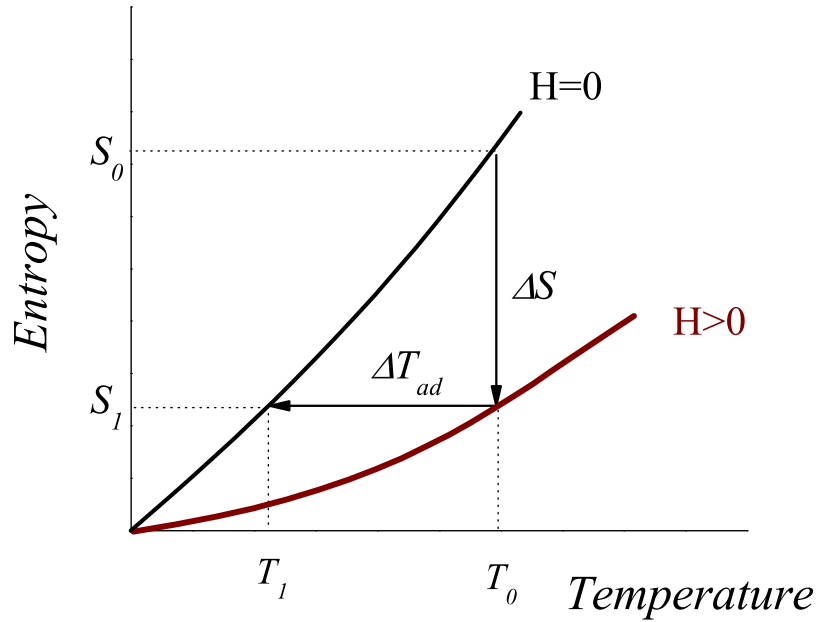
Figure 2.10: Schematic representation of the temperature dependence of the total entropy of a ferromagnetic material in zero-field and under an applied field. The entropy decreases by ΔS on applying a field isothermally, and adiabatic demagnetization leads to a temperature-decrease, ΔT_{ad}.

for $H = 0$ and at $H > 0$. The isothermal application of a magnetic field decreases the entropy from S_0 to S_1 and the adiabatic removal of the magnetic field causes a temperature change from an initial temperature T_0 to a final temperature T_1. ΔT_{ad} and ΔS are shown in Fig. 2.10. The magnetocaloric properties of a magnetic material can be characterized by the magnitude of ΔS and ΔT_{ad}.

The total entropy of a magnetic material, considering the pressure p, the absolute temperature T, and the magnetic field H as independent thermodynamic variables, can be written as [54,55],

$$S(p, T, H) = S_m(p, T, H) + S_{lat}(p, T) + S_e(p, T), \tag{3}$$

where S_m is the magnetic entropy, S_{lat} is the lattice entropy and S_e is the electronic entropy. S_m strongly depends on the magnetic field, while, usually, S_{lat} and S_e are magnetic-field-independent. The full differential of the total entropy in a closed system

is given by,

$$dS(p, T, H) = \left(\frac{\partial S}{\partial p}\right)_{T,H} dp + \left(\frac{\partial S}{\partial T}\right)_{p,H} dT + \mu_0 \left(\frac{\partial S}{\partial H}\right)_{p,T} dH. \quad (4)$$

At constant pressure and temperature, the total entropy changes only with magnetic field so that,

$$dS(p, T, H)_{p,T} = \mu_0 \left(\frac{\partial S}{\partial H}\right)_{p,T} dH. \quad (5)$$

The relation between the temperature derivative of the magnetization and the field derivative of the entropy is given by the Maxwell relation,

$$\left(\frac{\partial M(p, T, H)}{\partial T}\right)_{p,H} = \left(\frac{\partial S(p, T, H)}{\partial H}\right)_{p,T}. \quad (6)$$

The integral of Eq. 6 for an isothermal (and isobaric) process gives,

$$\Delta S_m(T, \Delta H) = \mu_0 \int_{H_1}^{H_2} \left(\frac{\partial M(T, H)}{\partial T}\right)_{p,H} dH, \quad (7)$$

where the magnetic field varies from H_1 to H_2 ($\Delta H = H_2 - H_1$).

Under adiabatic and isobaric conditions ($dS = dp = 0$), Eq. 4 is given by

$$dT = -\mu_0 \left(\frac{\partial T}{\partial S}\right)_H \left(\frac{\partial S}{\partial H}\right)_T dH. \quad (8)$$

The heat capacity C is defined by $C = dQ/dT$ where dQ is the heat quantity changes the system temperature by dT. Using the second law of thermodynamics, C can be written as $C = T(dS/dT)$. When this equation is used in Eq. 8 together with Eq. 6, the temperature change can be written as,

$$dT = -\mu_0 \left(\frac{T}{C}\right) \left(\frac{dM}{dT}\right)_T dH. \quad (9)$$

By integrating Eq. 9, the adiabatic temperature change ($\Delta T_{ad} = T_0 - T_1$) can be calculated using the relation,
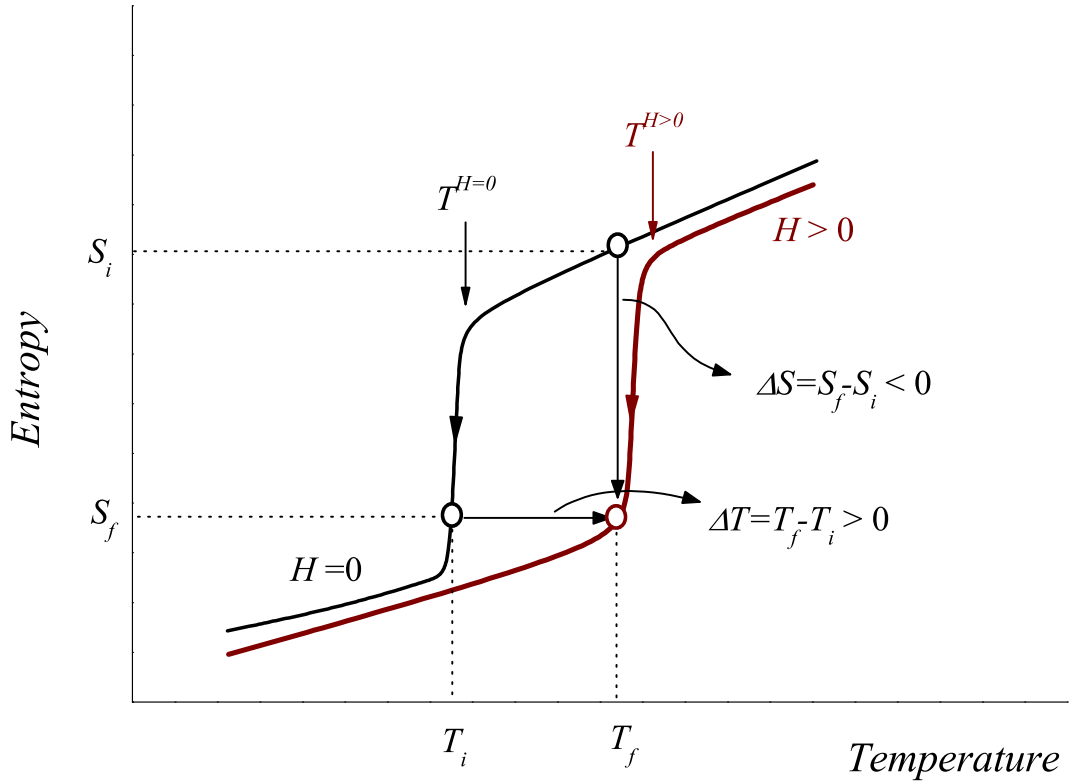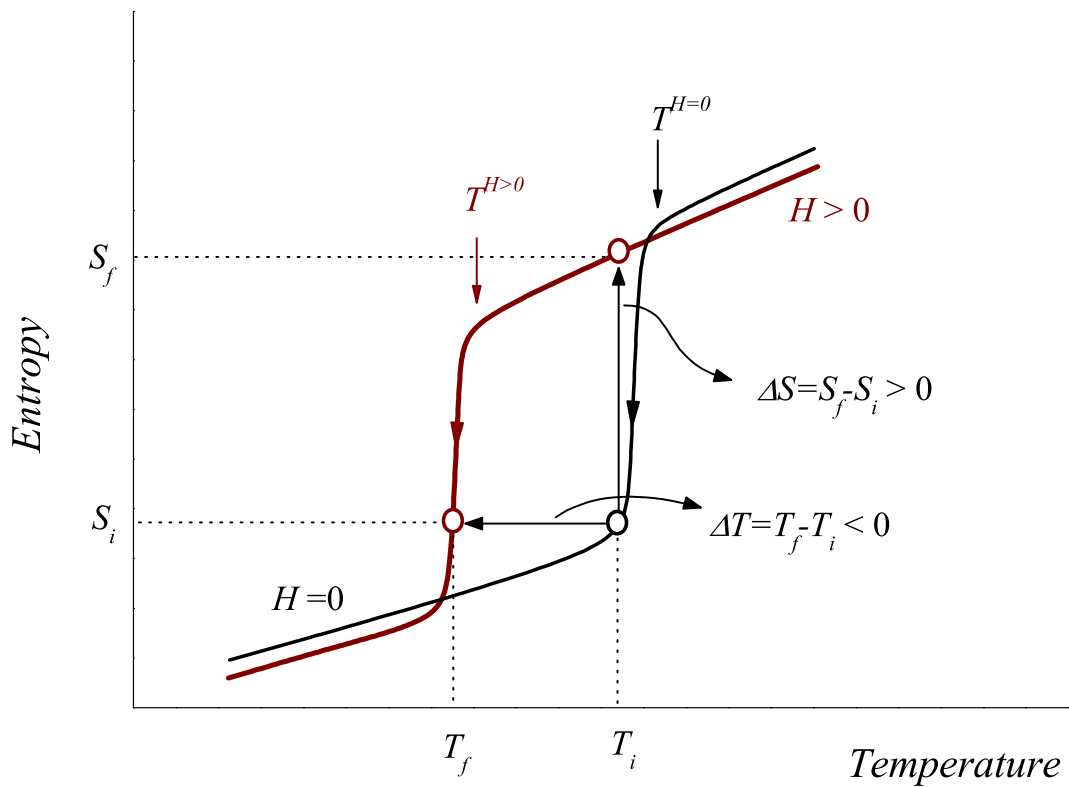
Figure 2.11: Schematic representation of the temperature dependence of the total entropy in $H = 0$ and $H > 0$ of a material which exhibits the conventional magnetocaloric effect around a first-order transformation. When a magnetic field is applied isothermally at T_f, the entropy decreases from S_i to S_f. When a magnetic field is applied adiabatically at T_i, the temperature increases by a value of ΔT.

$$\Delta T_{ad}(T, \Delta H)_{\Delta H} = -\mu_0 \int\limits_{H1}^{H2} \left(\frac{T}{C(T,H)} \right)_{p,H} \left(\frac{\partial M(T,H)}{\partial T} \right)_{p,H} dH. \tag{10}$$

In first-order phase transitions, the first derivative of the thermodynamic potential varies discontinuously. There is a jump at the transition temperature in the entropy or in the magnetization because of the presence of latent heat [56,57]. Figure 2.11 shows schematically $S(T)$ for a first-order transition under $H = 0$ and $H > 0$, whereby an application of a magnetic field shifts the transition temperature to higher values. $T^{H=0}$ and $T^{H>0}$ are indicated as the transition temperatures at $H = 0$ and $H > 0$ respectively.

The enthalpy E of the first-order transition increases the total entropy by a value of $\Delta E / T^{H=0}$ at $H = 0$ (or $\Delta E / T^{H>0}$ at $H > 0$). The jumps at the transition temperatures resulting from the transition enthalpy causes a large change in the entropy.

In Ni-Mn-based Heusler alloys, a typical prototype for the MCE is the Ni-Mn-Ga system. Ferromagnetic $Ni_{50}Mn_{50-x}Ga_x$ Heusler alloys exhibit a second-order transition at T_C^A which varies between 315 and 380 K according to Fig. 2.8(a). The martensitic transformation varies in the range $175 \leq M_s \leq 220$ K depending on the composition. A large $\Delta S = -20.7$ Jkg^{-1}K^{-1} has been observed in $Ni_{54.5}Mn_{20.5}Ga_{25}$ at 333 K under a 1.8 T magnetic-field-change [58]. At a slightly different composition, $Ni_{52.6}Mn_{23.1}Ga_{24.3}$, a MCE of similar magnitude was reported close to room temperature (301 K), under a 5 T magnetic-field-change [59]. An optimum value of MCE for the Ni-Mn-Ga is obtained when M_s and T_C^A coincide [60].

2.5.2   Inverse MCE

Figure 2.12 shows schematically $S(T)$ for $H = 0$ and $H > 0$, whereby applying a magnetic field shifts the transformation temperature to lower temperatures and gives rise to the inverse MCE. $T^{H=0}$ and $T^{H>0}$ are indicated as the transition temperatures at $H = 0$ and $H > 0$ respectively. The austenite-to-martensite transformation paths at $H = 0$ and $H > 0$ are shown, and the transformation hysteresis is omitted for clarity. At temperatures well within austenitic and martensitic states, $S_{H=0}(T) > S_{H>0}(T)$, whereas within the temperature range of the shift, $S_{H=0}(T) < S_{H>0}(T)$ so that when a magnetic field is applied at T_i, the entropy increases from S_i to S_f. When a magnetic field is applied adiabatically at T_i, the temperature decreases from T_i to T_f. This means that the magnetic field can cause the material to release heat so that $\Delta S > 0$ and $\Delta T_{ad} < 0$. This is known as the inverse MCE.

Further investigations on Heusler alloys led to the discovery of a MCE in Ni_2MnGa that has a positive ΔS with a value 10.7 Jkg^{-1}K^{-1} [61]. More recently, other Ni-Mn based Heusler alloys such as Ni-Mn-In [5,62,63], Ni-Mn-Sn [9], and Ni-Mn-Sb [34,35] have also shown large inverse MCE.

Figure 2.12: Schematic representation of the temperature dependence of the total entropy in $H = 0$ and $H > 0$ of a material which exhibits the inverse magnetocaloric effect around a first-order transformation. When a magnetic field is applied at T_i, the entropy increases from S_i to S_f. When a magnetic field is applied adiabatically at T_i, the temperature decreases by a value of ΔT.

3.   Experimental Methods

3.1   Sample Preparation

Approximately 3 g polycrystalline alloys were prepared in an arc-melting furnace under argon atmosphere in a water cooled Cu crucible. The components used were high purity elements (Nickel: 99.99%, Manganese: 99.99%, Tin: 99.99%, Indium: 99.99%, Antimony: 99.999%, Gallium: 99.99%). The melting process was repeated 5-6 times to attain homogeneous compositions. The ingots were encapsulated under argon in a quartz glass and annealed at 1073 K for 2 hours followed by quenching in ice-water. The chemical compositions of the alloys were determined by energy dispersive x-ray photoluminescence analysis (EDX) using scanning electron microscopy. For the analysis, one surface of the alloys was polished with 1200 grid SiC abrasive, and the average compositions of the alloys were determined from three different areas (250μm $\times$ 250μm). The resulting compositions were used to calculate the valance electron concentration (e/a) which is the concentration weighted sum of the number of 3d and 4s electrons of Ni and Mn and the number of 4s and 4p electrons of the Z element (Z: Ga, In, Sn and Sb). The values are listed in Tab. 3.1 and Tab. 3.2 for ternary and quaternary Heusler alloys respectively.

3.2   Calorimetric Studies

The method of differential scanning calorimetry (DSC) allows to determine M_s, M_f, A_s, A_f, the transformation enthalpy (H), and the entropy (S). For the DSC measurements, one side of the samples was polished with 1200 grid SiC abrasive to insure proper thermal contact. The measurements were carried out in the temperature range $120 \leq T \leq 830$ K in a standard calorimeter MDSC 2920 (TA Instruments) at Barcelona University, Spain. The cooling and heating rates were 2-5 K/min. A second high-sensitivity calorimeter [64] was used for measuring in the temperature range $100 \leq T \leq 350$ K for determining of the transformation parameters. The heating and cooling rates in these measurements were 1-2 K/min.

3.3   Magnetization Measurements

The magnetization as a function of temperature $M(T)$ in external magnetic fields of 5 mT and 5 T and the magnetization as a function of magnetic field $M(H)$ up to 5 T

Sample	at% Ni	at% Mn	at% Z	e/a
$Ni_{50}Mn_{27}Ga_{23}$	49.6	27.3	23.1	7.564
*$Ni_{50}Mn_{34}In_{16}$	50.3	33.7	16.0	7.869
*$Ni_{50}Mn_{34}In_{16}$-N	49.7	34.3	16.0	7.851
$Ni_{50}Mn_{35}In_{15}$	48.5	36.4	15.1	7.851
$Ni_{50}Mn_{35}In_{15}$-P	49.5	35.5	15.0	7.885
$Ni_{50}Mn_{35}In_{15}$-F	49.2	35.4	15.4	7.860
$Ni_{50}Mn_{35}Sn_{15}$	49.8	34.7	15.5	8.029
*$Ni_{50}Mn_{35}Sn_{15}$-N	49.6	35.1	15.3	8.029
$Ni_{50}Mn_{37}Sn_{13}$	49.9	37.0	13.1	8.104
$Ni_{50}Mn_{36}Sb_{14}$	50.3	35.9	13.8	8.233
$Ni_{50}Mn_{37}Sb_{13}$	49.6	37.3	13.1	8.226
$Ni_{50}Mn_{40}Sb_{10}$	50.3	39.6	10.1	8.307

Table 3.1: Concentrations of the $Ni_{50}Mn_{50-x}Z_x$ (Z : Ga, In, Sn, Sb) alloys determined by EDX analysis and their valence electron concentrations (e/a). F, N and P refer to the alloys which were used in ferromagnetic resonance, neutron scattering experiments, and polarized neutron scattering under pressure, respectively. The samples marked with an asteriks have been introduced by T. Krenke [4].

Sample	at.-% Ni	at.-% Mn	at.-% In	at.-% Z	e/a
$Ni_{50}Mn_{34}In_{14}Ga_2$	49.7	34.0	14.1	2.2	7.839
$Ni_{50}Mn_{34}In_{12}Ga_4$	50.9	33.5	11.6	4.2	7.909
$Ni_{50}Mn_{34}In_{15}Sn_1$	51.7	32.1	15.0	1.2	7.915

Table 3.2: Concentrations of quaternary alloys $Ni_{50}Mn_{34}In_{16-x}Z_x$ (Z: Ga and Sn) determined by EDX analysis and their valance electron concentrations (e/a).

were carried out in a SQUID (Superconducting Quantum Interference Device) MPMS XL magnetometer (Quantum Design). For the $M(T)$ measurements, the sample was cooled down in a zero-field-cooled state (ZFC) from 380 K to 5 K in the absence of a magnetic field and measured under an applied field up to 380 K. Then, without removing the external field, the data were taken on decreasing temperature from 380 K to 5 K, namely field-cooled (FC), and again, from 5 K to 380 K, the magnetization was measured on increasing temperature (field-heated; FH).

Magnetic susceptibility measurements were carried out in an AC susceptometer

(LakeShore 7120A at Barcelona University, Spain) in the temperature range $150 \leq T \leq 320$ K on cooling and heating. The working parameters were 500 Am^{-1} (6.28 Oe) applied field and 389 Hz frequency.

Magnetization measurements under pressure up to 10 kbar were performed in a SQUID magnetometer equipped with a pressure cell in the temperature range 5-340 K and in fields up to 5 T at IFW, Dresden.

3.3.1   Calculation of entropy change

In this work, the entropy change ΔS is determined by numerical integration using Eq. 7 from isothermal field-dependent magnetization measurements $M(H)$. Numerical integration of Eq. 7 is performed by using the trapezoidal rule [65], so that

$$\Delta S(T_{av}) = \mu_0 \frac{\delta H}{2\delta T} \left(\delta M_1 + 2\sum_{k=2}^{n-1} \delta M_k + \delta M_n \right).$$

(11)

Here, $\Delta S(T_{av})$ is proportional to the enclosed area between two measured field dependent magnetization isotherms at T_0 and T_1, and T_{av} is the average temperature $(T_1+T_0)/2$ in a magnetic field changing from H_1 to H_2 at a constant step δH. δT is the temperature difference between the two isotherms, and n is the number of measured data points from H_1 (first M_1) to H_2 (last M_n).

The accuracy of ΔS depends on the accuracy in the differentials of the measured magnetization, temperature and magnetic field (δM, δT and δH). The relative error in the determination of $\Delta S(T)$ is 3-10% [66,67].

3.4   Adiabatic Magneto-calorimeter

The adiabatic magneto-calorimeter is designed for measuring the adiabatic temperature change ΔT_{ad} directly. When the magnetocaloric material is subjected to a magnetic field, its temperature changes from an initial temperature T_i to a final temperature T_f, and ΔT_{ad} is the difference between T_f and T_i under an adiabatic magnetic field change $\Delta H = H_f - H_i$.

A schematic drawing of the magneto-calorimeter used in the present experiments is shown in Fig. 3.1. The whole apparatus is placed into a helium cryostat which incorporates a superconducting magnet delivering fields up to 5 T. The sample is hung with
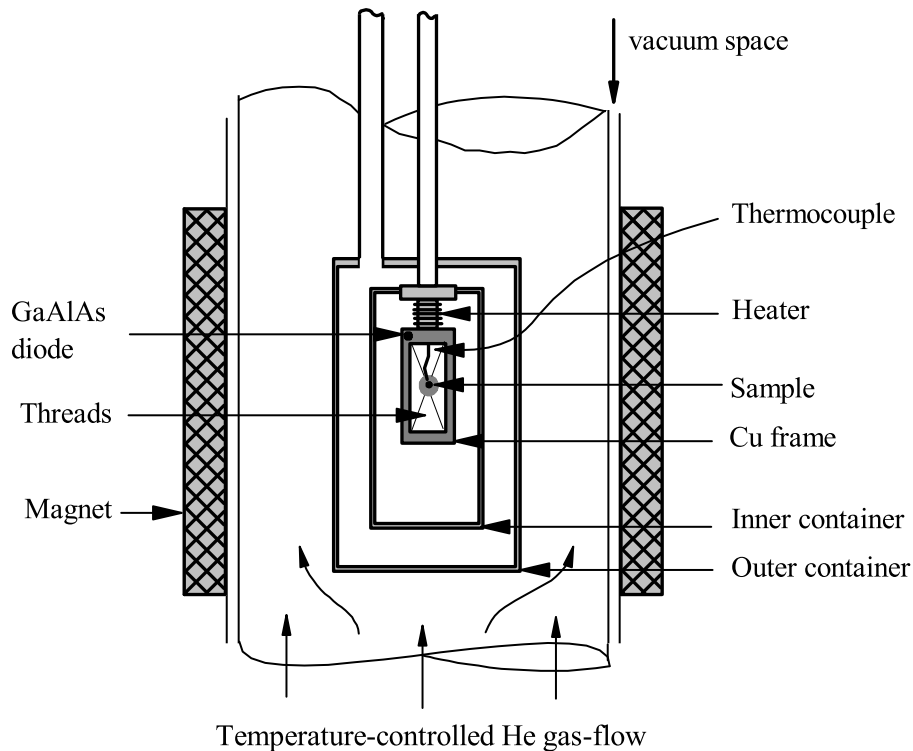
Figure 3.1: Schematic drawing of the low temperature part of the experimental setup for adiabatic temperature-change measurements using a differential thermocouple.

threads from the copper frame located in the inner container, which can be evacuated or filled with exchange gas. The space between the inner and outer containers is evacuated to obtain adiabatic conditions during a measurement. To heat or cool the sample to a desired temperature, this space is filled with exchange gas, and it is evacuated again before a measurement. A heater is located on the copper frame in the inner container. A calibrated and nearly field-insensitive GaAlAs diode thermometer (LakeShore TG-120-P) and the heater are used to measure and control the temperature of the copper frame. One leg of a differential thermocouple (copper-constantan) is placed into a drilled hole in the button-like sample weighing around 4 g. The other leg is referenced to 0° C. Prior to the measurement the exchange gas in the inner container is evacuated. The outer container remains under vacuum to prevent heat exchange with the environment
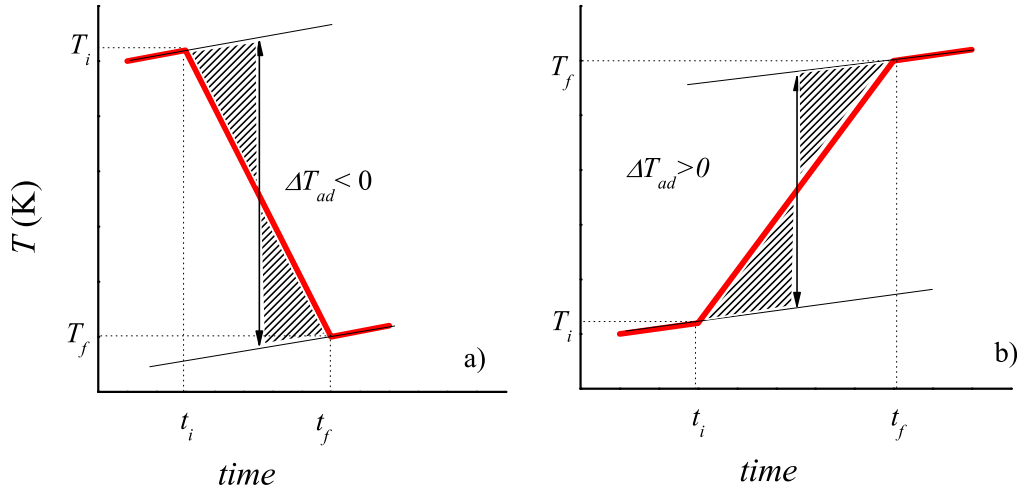
Figure 3.2: Determination of ΔT_{ad} (a) in an inverse and (b) a conventional magnetocaloric sample.

so that the conditions are adiabatic. This setup allows to determine the temperature change caused by applying or removing a magnetic field.

Fig. 3.2(a) and (b) show schematically the monitoring of the temperature in time before and after a magnetic field is applied to samples showing inverse and conventional magnetocaloric effects, respectively. The temperature of the calorimeter is monitored during the pre-measurement phase $t < t_i$, and, at a temperature T_i, a magnetic field is applied. The temperature is recorded as the magnetic field reaches its set value at $t = t_f$ and is further monitored for $t > t_f$. To correct for non-adiabatic conditions, the time dependence of T are extrapolated linearly and ΔT_{ad} is estimated by selecting equal shaded areas.

3.5   Strain Measurements

The thermal expansion and magnetostrictive properties of the alloys have been examined using strain gauges. The gauge consists of a parallel coiled wire encapsulated in epoxy. The type of strain gauge used was SK-00-031CF-120 (Vishay). The strain $\Delta l/l$ is directly proportional to the relative change in the resistance $\Delta R/R$ through the relationship

$$\frac{\Delta l}{l} = GF \cdot TO \cdot \frac{\Delta R}{R}, \tag{12}$$

where the gauge factor (GF) and the thermal output (TO) are intrinsic parameters of the strain gauge. The temperature dependence of GF and TO are supplied by the producer. Slices from the samples with a thickness of about 1 mm were used in the strain measurements. Both sides of the sample were polished with 1200 grid SiC abrasive. The strain gauges were fixed onto the slices using a low temperature epoxy resin (M-bond 610-1 Adhesive Single Mix Kit by Vishay). The resistance of the strain gauge was measured with the four-point method.

Temperature-dependent strain measurements at constant magnetic field up to 5 T in a temperature range of $100 \leq T \leq 300$ K and magnetic-field-dependent strain measurements at constant temperature were carried out. The samples were first cooled to $T < M_f$ without magnetic field and then heated up to the desired temperature where the magnetic field was applied. The relative length change is given by $\Delta l/l = (l - l_0)/l_0$, where l_0 is the length at room temperature. In magnetic field dependent strain measurements the strain is defined as $\Delta l/l = (l_h - l_0)/l_0$. Here, l_0 is the length in the absence of field and l_h is the length in the presence of field. Details of the strain gauge geometry are given in reference [4].

3.6   Elastic Neutron Scattering

The SPODI spectrometer is a thermal, high resolution structural powder diffractometer at the Forschungs-Neutronenquelle Heinz-Maier Leibnitz (FRM-II), Munich, Germany [68]. Figure 3.3 shows a schematic view of the spectrometer. The detector array consists of 80 position-sensitive ^{3}He dedector tubes with fixed collimators. The collimators with 10′ horizontal divergence are located in front of each detector. The detectors span an angular range of $2\theta= 160°$, and the scattering range of each detector is 2°. The data collection is performed with a step-width of $\Delta(2\theta) = 0.05°$. The vertical focusing monochromator consists of 17 Ge crystals with (551) orientation. The experiments have been performed with a neutron wavelength λ=1.549 Å. We used a closed-cycle cryostat and a superconducting magnet in the sample environment. The cryostat operates from 4 to 450 K, and the magnet can reach up to 5 T.

The powder alloys were placed in a thin-walled vanadium container and pressed with a cadmium-roller. For each alloy, diffraction data were collected in the angular range $5° \leq 2\theta \leq 155°$ at 300 K and 5 K under zero-magnetic-field and under a 5 T cooling-

secondary
collimators
(5',10',20')

Monochromator
Ge(551)

He^3 detectors

$2\theta=155^o$

Neutron
Beam

Sample

Magnet

Collimators
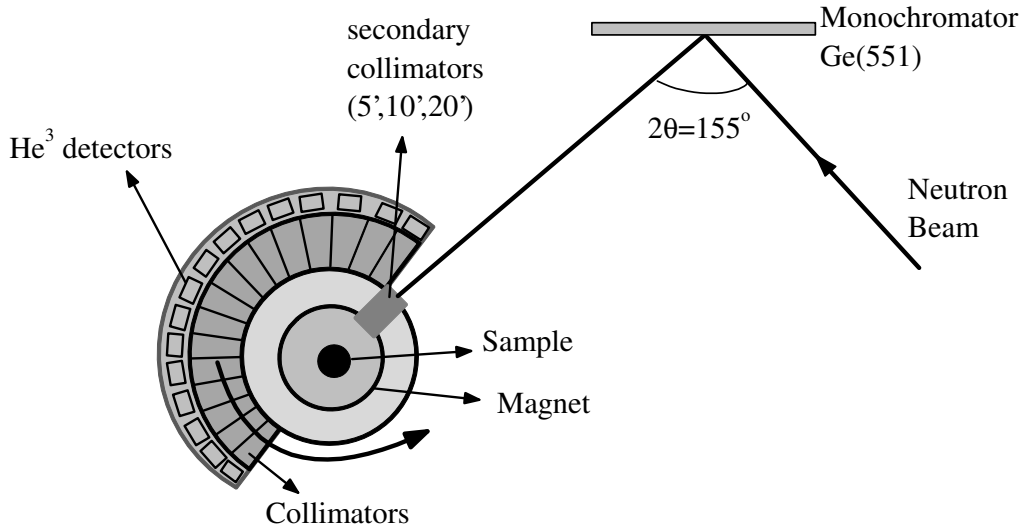
Figure 3.3: Layout of the powder diffractometer SPODI at the FRM-II reactor, Munich.

field. All diffraction patterns were analyzed using the Fullprof Suit program, and the estimated errors for lattice parameters are about ±0.0030 Å.

3.7   The D7 Polarized Neutron Spectrometer

D7 is a long-wavelength diffuse scattering spectrometer at the ILL, Grenoble, France [69]. Figure 3.4 shows a schematic view of the spectrometer. Neutrons from the cold neutron source are monochromated by a focusing pyrolitic graphite monochromator crystal array. The take-off angle from the monochromator crystal is $2\theta= 92.3°$, and the wavelength is 4.8 Å. Neutrons are polarized by a supermirror bender polarizer and spins can be flipped using a Mezei π-spin-flipper [70,71]. The polarized neutron flux is 1.8×10^6 cm^{-2}s^{-1}. Neutrons enter a neutron guide field of around 1 mT and then interact with the sample which is placed in the center of 3 orthogonal XYZ field coils. Some of the scattered neutrons are flipped by the sample and enter the detector banks with an array of supermirror analyzers.

The D7 spectrometer provides the opportunity to separate nuclear-coherent (Bragg) $\sigma^{coh} \equiv (d\sigma/d\Omega)_{coh}$, nuclear spin-incoherent $\sigma^n \equiv (d\sigma/d\Omega)_n$ and magnetic $\sigma^m \equiv (d\sigma/d\Omega)_{mag}$ scattering differential cross-sections experimentally using full 3-directional
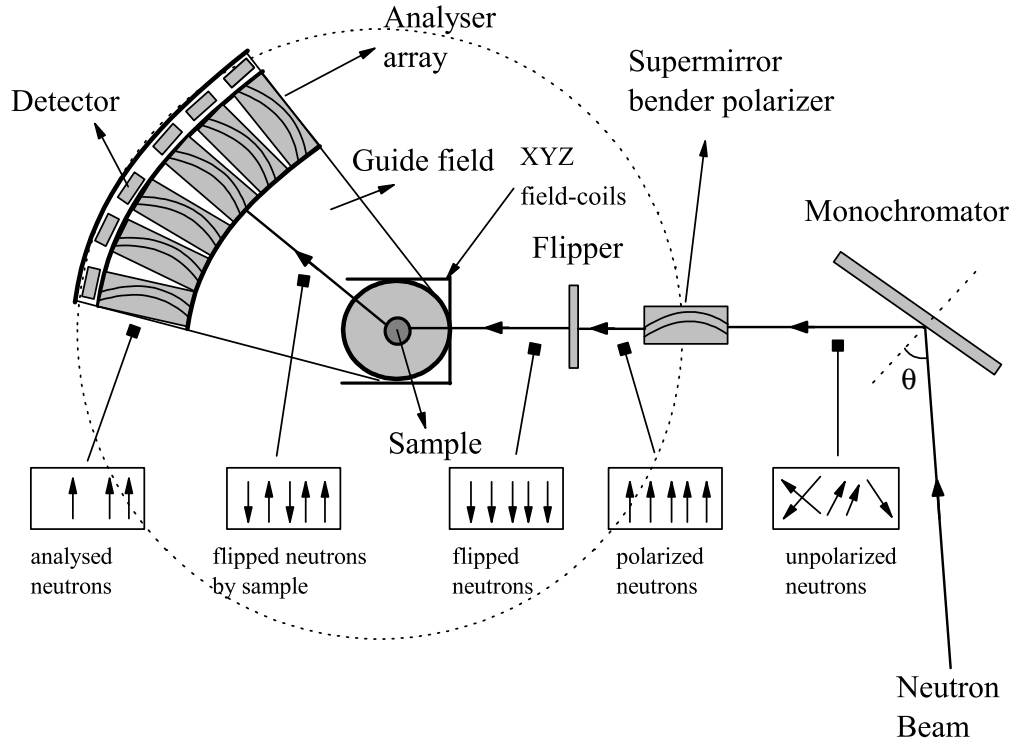
Figure 3.4: Schematic view of the D7 spectrometer at ILL, Grenoble.

XYZ polarization analysis [72,73]. In addition to the differential cross-sections, the flipping ratio (R_F) of the neutrons traversing the sample is also measured. R_F is defined as the ratio of the number of spin-up ($n_\uparrow$) to spin-down ($n_\downarrow$) eigenstates and is a measure of the neutron depolarization.

$$R_F = \frac{1 + n_\uparrow}{1 + n_\downarrow}. \tag{13}$$

In a sample where the net magnetization is zero, the neutron polarization state and, thus, R_F is not affected by the sample. However, in a sample with FM domains, a neutron spin will experience a torque causing it to precess around the magnetization direction of the FM domains that are inhomogeneously distributed across the beam profile. This causes a non-adiabatic depolarization of the neutron state with a resultant drop in R_F. The depolarization measurement is, therefore, a very sensitive tool for the determination of ferromagnetic domain formation.

Annealed powder-samples (about 3 g) are used for the polarization analysis experi-
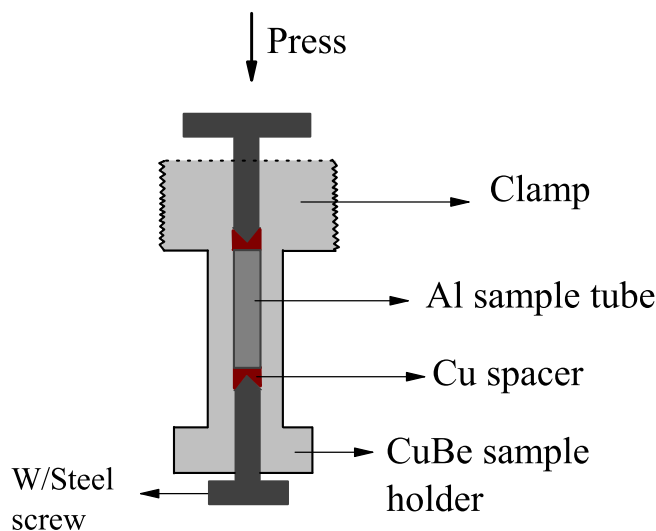
Figure 3.5: Schematic view of the pressure cell.

ments. The particle size of the powder is about 10 μm. The cross sections are corrected for detector efficiency and calibrated via a vanadium sample. Vanadium has a very small coherent and a large nuclear spin-incoherent scattering cross section (0.0184 and 5.187 barn respectively) and, thus, its scattering is isotropic. The analyzer efficiency is corrected via a quartz glass sample. Having no nuclear spin, quartz glass gives only coherent diffuse scattering. All data analysis are carried out using the program LAMP (Large Array Manipulation Program) provided by the ILL.

Polarized neutron scattering measurements under hydrostatic pressure were performed on the D7 spectrometer using a clamp-type pressure cell shown schematically in Fig.3.5. The powder sample is encapsulated inside an Al sample holder. The cell is then pressed and clamped. To achieve hydrostatic conditions we use fluorinert (FC-87) as the pressure transmitting medium. Flourinert contains no hydrogen so that it is used conveniently in high-pressure neutron diffraction experiments [74].

3.7.1 Polarization Analysis

To separate the nuclear and magnetic scattering from the total scattering, two measurements, spin-flip (SF) and non-spin-flip (NSF), are performed with the polarization sequentially along the x, y and z axis. The incident neutrons are polarized in the z-
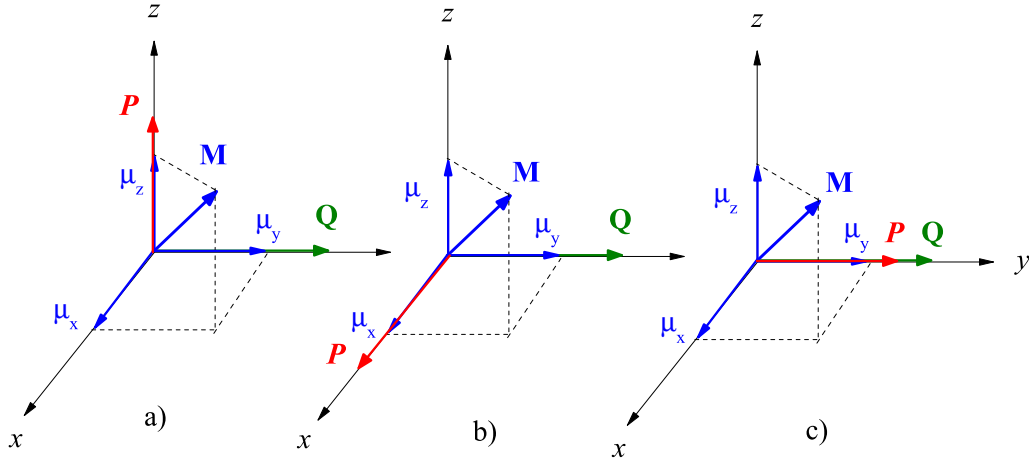
Figure 3.6: The geometry of the XYZ neutron polarization analysis experiment with initial polarization, **P**, (a) in the z-direction, (b) in the x-direction and (c) in the y-direction. The scattering wavevector, **Q**, is chosen to be in the y-direction. **M** indicates the magnetization vector with components μ_x, μ_y and μ_z.

direction, and with the spin turner coils, the polarization of the neutrons can be rotated in the x and y directions.

The polarization vector P along each axis is plotted in Fig. 3.6. The rotation of P perpendicular or parallel to the scattering vector leads to different scattering conditions [75]. The basic scattering conditions are listed below followed with an example.

- Coherent nuclear scattering (σ^{coh}) is always NSF scattering.

- The magnetic scattering and the nuclear-spin incoherent scattering (σ^m and σ^n) are NSF if the effective spin components are along the neutron polarization direction, and the scattering is SF if the effective spin components are perpendicular to the polarization direction.

- If the neutron polarization is along the scattering vector, then all magnetic scattering is SF scattering.

- If the magnetization vector is along the scattering vector, no SF scattering is observed.

Figure 3.6 shows the magnetization vector of the nuclear or the electronic moment $\vec{\mu}$ (whichever one being in question), the scattering vector **Q** and the polarization vector

P. **Q** is chosen in the y-direction. The unit vectors of the Cartesian coordinates are given as $\hat{x}$, $\hat{y}$, and $\hat{z}$. If for example, **P** is parallel to $\hat{z}$, **P** $\parallel$ $\hat{z}$ (Fig.3.6(a)), SF scattering occurs from the nuclear spin components perpendicular to **P** (σ_x^n and σ_y^n) and from the magnetization components perpendicular to the **P** (σ_x^m). No SF scattering occurs along the y-direction because **Q** $\parallel$ $\mu_y\hat{y}$. NSF scattering is caused by the nuclear spin and magnetic components parallel to **P** ($\sigma_z^n + \sigma_z^m$).

$$\mathbf{P} \parallel \hat{z} \quad \text{SF:} \quad \sigma_x^m + \sigma_x^n + \sigma_y^n = \sigma^m + 2\sigma^n$$
$$\text{NSF:} \quad \sigma_z^m + \sigma_z^n + \sigma^{coh} = \sigma^m + \sigma^n + \sigma^{coh}$$

Similarly, for **P** $\parallel$ $\hat{x}$ and **P** $\parallel$ $\hat{y}$ one has:

$$\mathbf{P} \parallel \hat{x} \quad \text{SF:} \quad \sigma_z^m + \sigma_z^n + \sigma_y^n = \sigma^m + 2\sigma^n$$
$$\text{NSF:} \quad \sigma_x^m + \sigma_x^n + \sigma^{coh} = \sigma^m + \sigma^n + \sigma^{coh}$$
$$\mathbf{P} \parallel \hat{y} \quad \text{SF:} \quad \sigma_x^m + \sigma_z^m + \sigma_x^n + \sigma_z^n = 2\sigma^m + 2\sigma^n$$
$$\text{NSF:} \quad \sigma_y^n + \sigma^{coh} = \sigma^n + \sigma^{coh}$$

In this manner, it is possible to separate the magnetic and nuclear magnetic scattering components from the total scattering. Detailed formulations of the separation of cross sections can be found in Appendix A1.

3.8   Ferromagnetic Resonance

Ferromagnetic resonance (FMR) is a spectroscopic technique of probing the magnetization of ferromagnetic materials by detecting the precessional motion of the magnetization in an external magnetic field. The magnetic field exerts a torque on the magnetization which causes the magnetic moments of electrons to precess. The magnetic sample is mounted in a microwave resonant cavity fixed at a high frequency (GHz) between the poles of the electromagnet while the magnetic field is swept. When measuring the absorption of the microwave by the magnetic material, the resonance field is found at maximum absorption. The measured FMR signal is proportional to the field derivative of the imaginary part of the transverse suseptibility ($\partial\chi"/\partial H$) [76–78]. From the resonance position, intensity and the line shape, it is possible to extract information on the magnetic interactions and magnetic anisotropy energies [79].
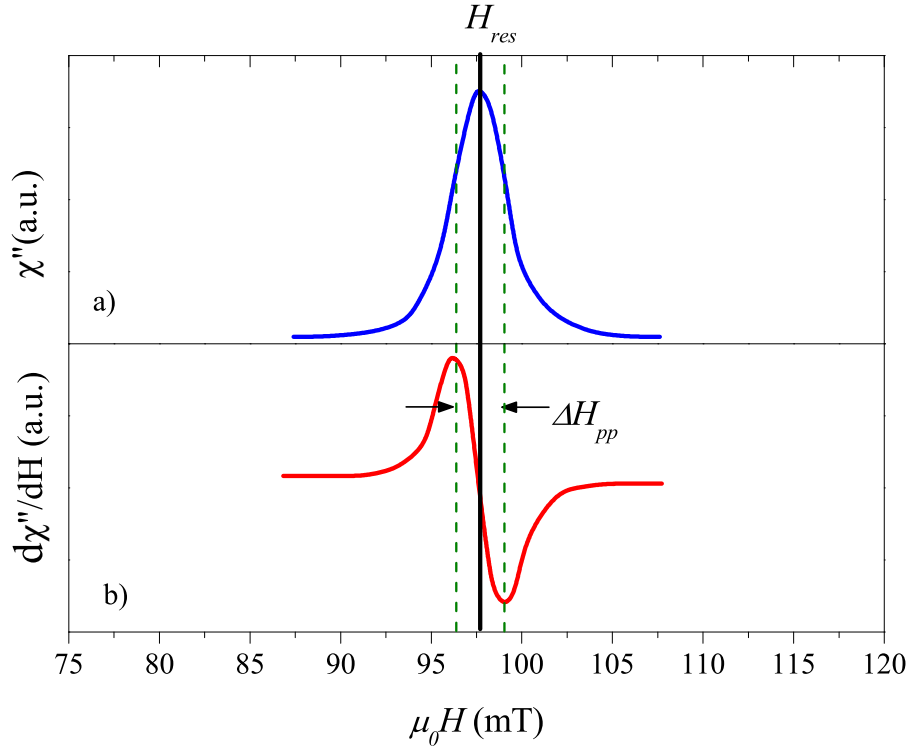
Figure 3.7: Schematic representation of (a) the transverse susceptibility and (b) the measured FMR signal.

FMR experiments were carried out at a microwave frequency of 9.29 GHz in the temperature interval $5 \leq T \leq 300$ K on powdered polycrystalline samples. The external magnetic field was swept up to 1.8 T and resonance spectra were recorded as a function of temperature. The external magnetic field was modulated at a frequency of 100 kHz using modulation amplitudes up to 3 mT. As an example, a schematic representation of a FMR spectrum is shown in Fig. 3.7. The dashed lines show the peak-to-peak width ΔH_{pp}, and the central line is placed at the position of the resonance field H_{res}.

The isotropic value of the resonance field is given as $\omega/\gamma \approx 330$ mT, where ω is the microwave frequency and γ is the gyromagnetic ratio. For a paramagnet, the resonance field is $H_{res} = \omega/\gamma$. For ferromagnetically coupled spins, H_{res} is located below ω/γ as a result of the anisotropy field which is randomly oriented over the polycrystalline FM material. When the material is antiferromagnetic, the spins are coupled by an exchange field and the resonance field is above ω/γ. Therefore, ferromagnetic resonance is a powerful method for investigating the magnetic interactions in martensitic Heusler alloys

for which mixed FM and AF coupling is expected to occur below and above M_s.

4. Results and Discussions

4.1 Tailoring Magnetic Properties of Martensitic Ni-Mn-based Heusler Alloys

Recently, much interest has developed in the study of quaternary Ni-Mn-based Heusler systems, where either the transition metal or the group IIIA-VA p-element is substituted with another transition metal or another p-element [12,80–84]. The aim of substitution is to shift the transformation temperature to a desired temperature or to improve the properties related to the magnetocaloric effect, the magnetic shape memory effect, etc. and, thereby, to design new alloys. As a guide for a systematic substitution, one can make use of the diagram in Fig. 4.1 showing the valance electron concentration (e/a) dependence of M_s in Ni-Mn-Z Heusler alloys (Z: Ga, In, Sn and Sb) [85]. The e/a dependence of M_s is linear but the slope for each Ni-Mn-based series increases with respect to that of the Ni-Mn-Ga line with increasing number of p electrons of the Z-element. The different slopes could be related to the different atomic radii of the Z-elements. For example, by replacing Ga by In atoms with larger atomic radius ($r_{Ga}=$ 1.81×10^{-10} m and $r_{In}=$ 2.00×10^{-10} m), the covalent bonds between Ni 3d-states and In 4p-states can strengthen, and lead to a stabilization of the L2$_1$ structure. Therefore,
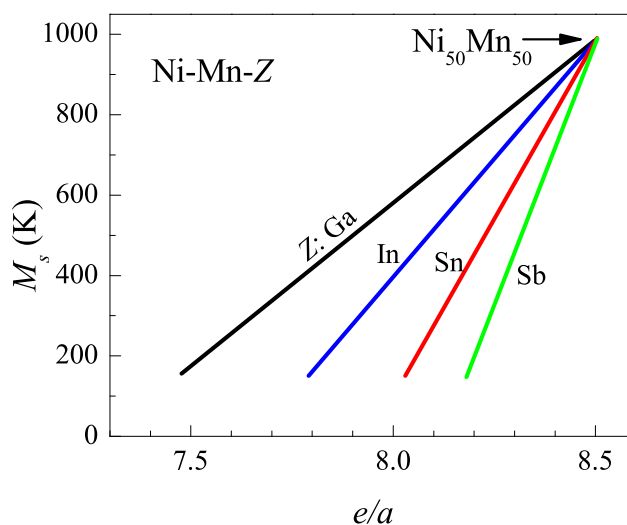
Figure 4.1: The dependence of M_s on the valance-electron-concentration for Ni-Mn-Z (Z: In, Sn and Sb) Heusler alloys.

at constant electron concentration, one can expect a lower M_s.

$Ni_{50}Mn_{34}In_{16}$ undergoes a martensitic transformation and exhibits large field-induced strains and the inverse magnetocaloric effect [5,86]. It would be desirable to bring these favorable properties close to room temperature for technological purposes. We use Fig. 4.1 as a guide for manipulating the properties of this material by replacing various Z-elements with one another, thereby controlling e/a. In and Ga are isoelectronic elements, whereas In, Sn and Sb are in the same period in the periodic table, and the number of p electrons increase from In to Sb. We choose two different paths to vary the properties:

1. M_s can be controlled not only by varying e/a, but also by holding e/a constant, such as by replacing In by Ga. In this case, M_s can be shifted to higher temperatures.

2. $Ni_{50}Mn_{37}Sn_{13}$ shows a large inverse MCE around room temperature. Therefore, Sn substitution for In in $Ni_{50}Mn_{34}In_{16}$, which increases e/a at constant M_s, can lead to an increase in the inverse MCE in this material without altering the working temperature.

In the following, the results of Ga and Sn substitutions in $Ni_{50}Mn_{34}In_{16}$ will be presented separately in two parts. The first parts deal with the magnetic characterization of the substituted samples and the magnetocaloric properties, and the second parts include the field-induced strain measurements. In the summary, Ga and Sn substitution will be compared.

4.1.1   Ga substitution: $Ni_{50}Mn_{34}In_{14}Ga_2$

Magnetic and magnetocaloric properties

Figures 4.2(a) and (b) show $M(T)$ under a 5 mT magnetic field measured in ZFC, FC and FH sequences for $Ni_{50}Mn_{34}In_{16}$ and $Ni_{50}Mn_{34}In_{14}Ga_2$. These samples are FM below T_C^A=308 K for $Ni_{50}Mn_{34}In_{16}$, and 293 K for $Ni_{50}Mn_{34}In_{14}Ga_2$. For $Ni_{50}Mn_{34}In_{16}$, the ferromagnetism extends down to M_s=243 K, below which the magnetization rapidly decreases. In the vicinity of this temperature, FC and FH-data show a narrow hysteresis which is associated with the martensitic transformation (Fig. 4.2(a)). Splitting between the ZFC and the FC data in the martensitic state is observed about $T_C^M \approx$225 K which is related to the strong magnetic anisotropy of the martensite phase and the pinning of

the FM spin configurations caused by coexisting AF exchange. On the other hand, M_s increases to 275 K for $Ni_{50}Mn_{34}In_{14}Ga_2$, and the FM austenite region becomes narrower than in the parent $Ni_{50}Mn_{34}In_{16}$ sample. However, T_C^M decreases to about 210 K.

FC-$M(T)$ measured in high magnetic fields of 5 T for $Ni_{50}Mn_{34}In_{16}$ and $Ni_{50}Mn_{34}In_{14}Ga_2$ are shown in Fig. 4.3(a). Open and closed symbols represent the data for $Ni_{50}Mn_{34}In_{16}$, coded as Ga0, and $Ni_{50}Mn_{34}In_{14}Ga_2$, coded as Ga2. The M_s as a function of applied magnetic field is plotted in Fig. 4.3(b). The slope of the lines representing the shift of M_s are estimated as $dM_s/dH \approx$ -6 KT^{-1} for $Ni_{50}Mn_{34}In_{16}$ and $dM_s/dH \approx$ -1 KT^{-1} for $Ni_{50}Mn_{34}In_{14}Ga_2$. $M(T)$ measured in 5 T and the hysteresis related to the martensitic transformation between FC and FH measurements can be seen in Fig. 4.4. The thermal hysteresis for $Ni_{50}Mn_{34}In_{14}Ga_2$ narrows with respect to that
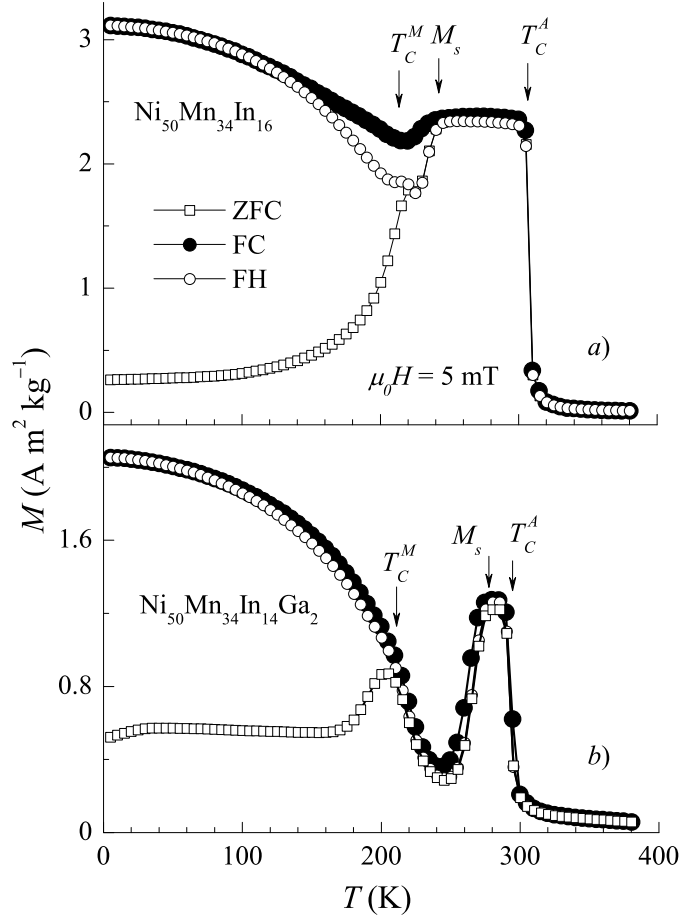
Figure 4.2: ZFC, FC, and FH $M(T)$ in 5 mT of (a) $Ni_{50}Mn_{34}In_{16}$ and (b) $Ni_{50}Mn_{34}In_{14}Ga_2$. Vertical arrows show T_C^A, M_s and T_C^M.
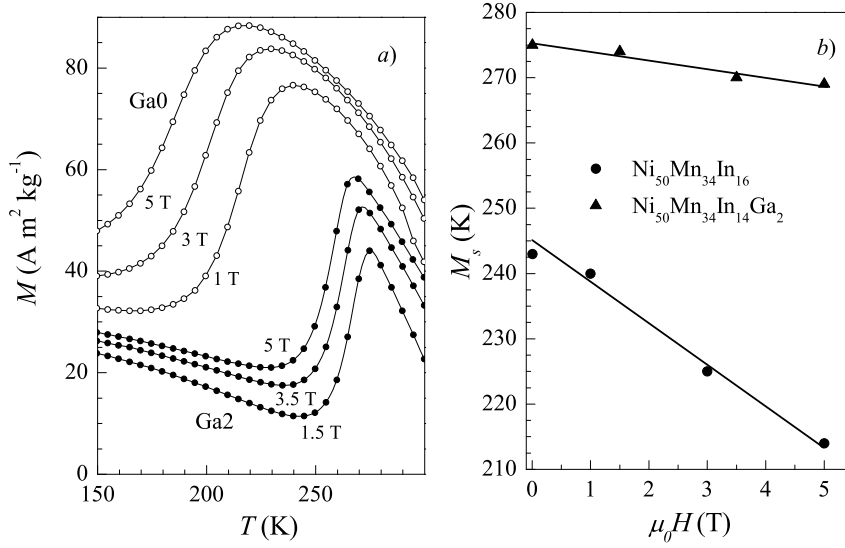
Figure 4.3: $M(T)$ for $Ni_{50}Mn_{34}In_{16}$ (Ga0), and $Ni_{50}Mn_{34}In_{14}Ga_2$ (Ga2), in high fields. (a) FC-$M(T)$ for $Ni_{50}Mn_{34}In_{16}$ and $Ni_{50}Mn_{34}In_{14}Ga_2$. (b) M_s as a function of external cooling field for $Ni_{50}Mn_{34}In_{16}$, and $Ni_{50}Mn_{34}In_{14}Ga_2$.

for $Ni_{50}Mn_{34}In_{16}$. On the other hand, the magnetization of $Ni_{50}Mn_{34}In_{14}Ga_2$ is lower than that of $Ni_{50}Mn_{34}In_{16}$ at 5 K. The saturation magnetization under 5 T magnetic field decreases by adding Ga from 47 Am^2kg^{-1} to about 34 Am^2kg^{-1}. The width of thermal hysteresis decreases from 25 K to 7 K.

The magnetization isotherms in the vicinity of M_s are shown in Fig. 4.5(a) and (b). The data shown with open red circles in both figures correspond to $M(H)$ for $T < M_s$, and the filled black circles correspond to $T > M_s$. $M(H)$ for $T < M_s$ shows metamagnetic behavior suggesting the presence of a field-induced transformation. $M(H)$ initially increases with increasing field until it reaches an inflection point at a critical field H_c. Above this point, $M(H)$ begins to increase faster with increasing magnetic field. For $Ni_{50}Mn_{34}In_{14}Ga_2$, the field-induced transformation begins to take place at lower fields than those needed for $Ni_{50}Mn_{34}In_{16}$, so that the sharp rise in $M(H)$ begins already below 1 T. The narrower hysteresis in $M(T)$ for $Ni_{50}Mn_{34}In_{14}Ga_2$ in Fig. 4.4 is the reason for the lower threshold of the transformation than for $Ni_{50}Mn_{34}In_{16}$.

The entropy change ΔS determined numerically from the $M(H)$-data using Eq. 11 in section 3 is shown in Fig. 4.6(a) and (b) for $Ni_{50}Mn_{34}In_{16}$ and $Ni_{50}Mn_{34}In_{14}Ga_2$, respectively. For both samples, $\Delta S(T)$ is positive below M_s (inverse MCE) and negative
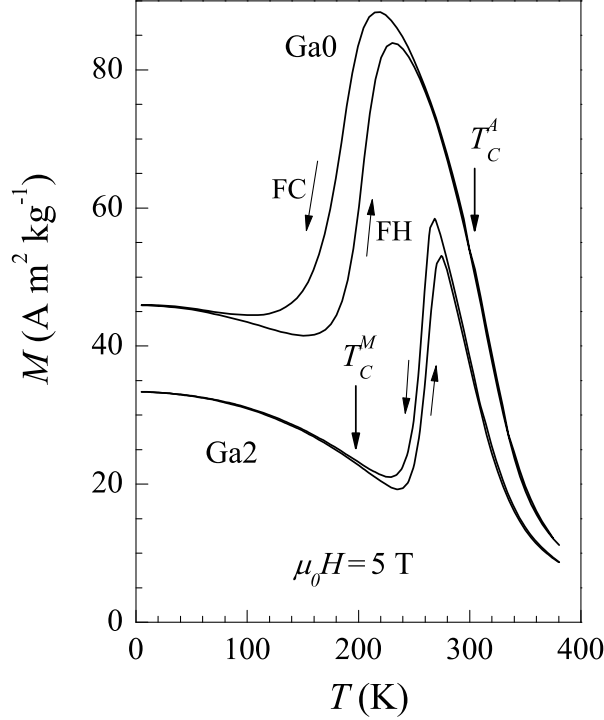
Figure 4.4: $M(T)$ for $Ni_{50}Mn_{34}In_{16}$ (Ga0) and $Ni_{50}Mn_{34}In_{14}Ga_2$ (Ga2) in the FC and FH states under 5 T applied field. The vertical arrows indicate T_C^A and T_C^M. Thermal hysteresis is narrower in $Ni_{50}Mn_{34}In_{14}Ga_2$.

around T_C^A (conventional MCE) with the crossover taking place at the temperature corresponding to M_s as shown in Fig. 4.6. The magnitude of the entropy-changes below M_s are almost equal for both samples with a maximum value of 8 Jkg^{-1}K^{-1} in 5 T applied field. Above M_s, ΔS of $Ni_{50}Mn_{34}In_{16}$ and $Ni_{50}Mn_{34}In_{14}Ga_2$ are about -5 Jkg^{-1}K^{-1} under 5 T.

The results of the direct measurements of the adiabatic temperature-change as a function of temperature, $\Delta T_{ad}(T)$, in a magnetic field are given in Fig. 4.7. Both samples cool on applying a magnetic-field below M_s and warm on applying a field around T_C^A. For $Ni_{50}Mn_{34}In_{16}$, the maximum ΔT below M_s is -2 K in 5 T, and around T_C^A, it is about 3.5 K (Fig. 4.7(a)). Each of these values are about 2 K for $Ni_{50}Mn_{34}In_{14}Ga_2$ in Fig. 4.7(b). The MCE above M_s is smaller than in $Ni_{50}Mn_{34}In_{16}$, and this is consistent with the smaller ΔS.
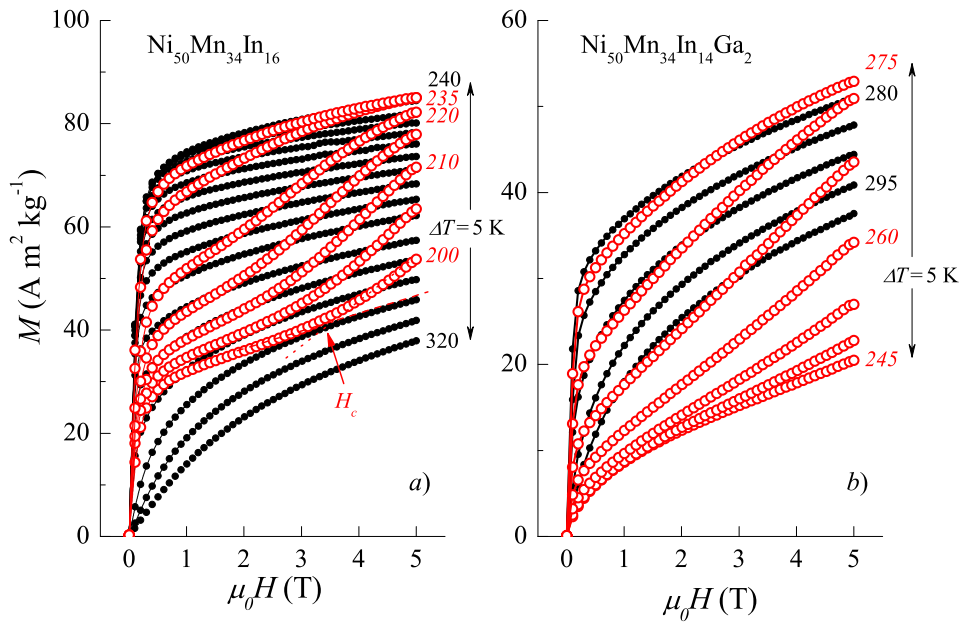
Figure 4.5: Magnetic-field dependence of the magnetization for (a) $Ni_{50}Mn_{34}In_{16}$ at $200 \leq T \leq 320$ K and (b) $Ni_{50}Mn_{34}In_{14}Ga_2$ at $245 \leq T \leq 300$ K in 5 K steps. Open red circles and filled circles are data measured $T < M_s$ and $T > M_s$ respectively. H_c is shown by arrow.
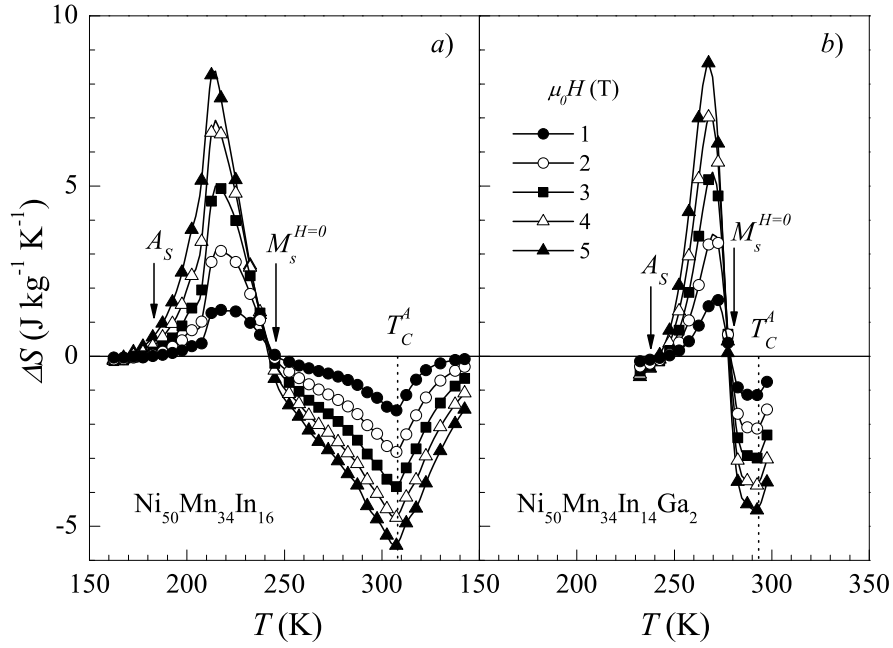
Figure 4.6: Temperature dependence of the isothermal entropy-change around the marten-sitic transformation and T_C^A for (a) $Ni_{50}Mn_{34}In_{16}$ and (b) $Ni_{50}Mn_{34}In_{14}Ga_2$.
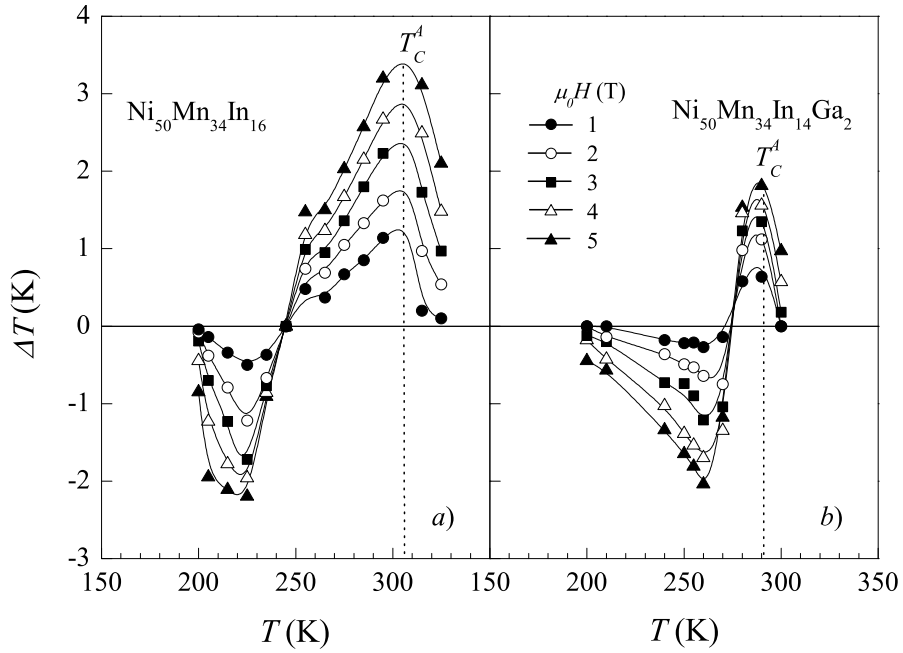
Figure 4.7: Temperature dependence of the adiabatic temperature-change ΔT_{ad} around M_s and at T_C^A in (a) $Ni_{50}Mn_{34}In_{16}$ and (b) $Ni_{50}Mn_{34}In_{14}Ga_2$.
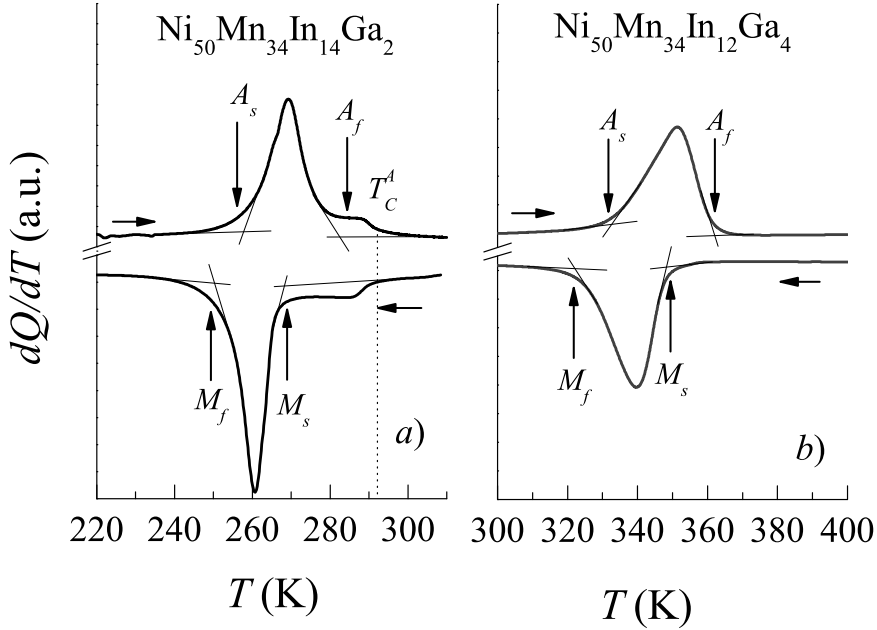
Figure 4.8: dQ/dT versus temperature for (a) $Ni_{50}Mn_{34}In_{14}Ga_2$ and (b) $Ni_{50}Mn_{34}In_{12}Ga_4$. Horizontal arrows indicate the direction of temperature change, and the vertical arrows show the locations of the characteristic temperatures.

The results of calorimetric measurements for $Ni_{50}Mn_{34}In_{14}Ga_2$ and $Ni_{50}Mn_{34}In_{12}Ga_4$ are plotted in Figs. 4.8(a) and (b), where the heating and cooling cycles are shown by arrows. The austenite to martensite transformation is exothermic, whereas the reverse transformation is endothermic ($dQ/dT > 0$). The martensitic transformation temperature shifts to higher temperatures when Ga substitution increases. The transition temperatures M_s, M_f, A_s and A_f are indicated with vertical arrows. These temperatures are estimated from the intersection points of the linearly extrapolated data. The values are listed in Table 4.1. In $Ni_{50}Mn_{34}In_{14}Ga_2$, the values are approximately the same as those obtained from $M(T)$. A further feature is observed in $Ni_{50}Mn_{34}In_{14}Ga_2$ at T_C^A.

$M(T)$ of $Ni_{50}Mn_{34}In_{12}Ga_4$ measured in 5 mT and 5 T is shown in Figs. 4.9(a) and (b). A broad magnetic transition occurs around $T_C^M = 135$ K, which is close to the temperature where the splitting of the FC and ZFC curves takes place. When a 5 T magnetic field is applied, a peak-like feature related to the martensitic transformation becomes visible as can be seen in Fig. 4.9(b). M_s being about 350 K according to Fig. 4.9(b), the $M(T)$-data indicate that the martensitic transformation occurs from a PM austenitic
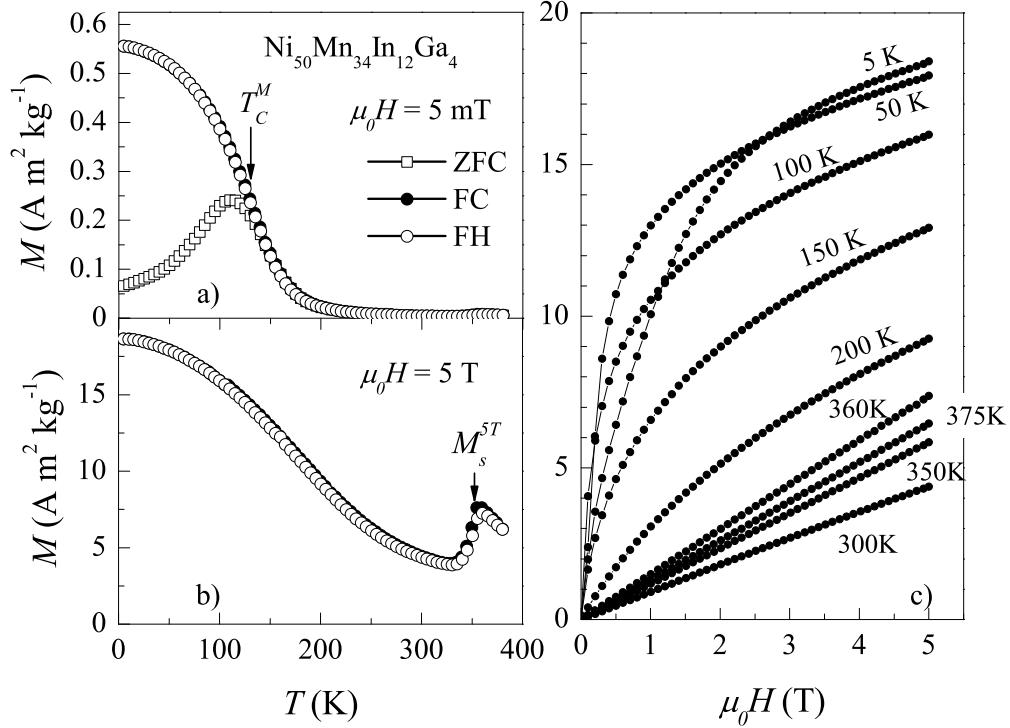
Figure 4.9: The magnetization of $Ni_{50}Mn_{34}In_{12}Ga_4$. (a) ZFC, FC, and FH $M(T)$ in 5 mT and (b) FC and FH $M(T)$ in 5 T (c) $M(H)$ at selected temperatures. Vertical arrows indicate T_C^M and M_s^{5T}.

to a PM martensitic state so that all characteristic temperatures cannot be precisely defined. The magnetization of the austenitic state is more enhanced than that in the martensitic state under 5 T. The temperature corresponding to the peak is at $M_s^{5T} =$ 350 K being close to the value obtained from DSC measurements, i.e. $M_s^{5T} \approx M_s^{H=0}$.

$M(H)$ measurements are shown at several temperatures in Fig. 4.9(c). $M(H)$ is linear at high temperatures in the PM state. In the martensitic transformation region,

Sample	$A_s^{DSC/M}$ (K)	$A_f^{DSC/M}$ (K)	$M_s^{DSC/M}$ (K)	$M_f^{DSC/M}$ (K)
$Ni_{50}Mn_{34}In_{14}Ga_2$	258/250	282/280	268/275	249/250
$Ni_{50}Mn_{34}In_{12}Ga_4$	334/-	358/-	347/$\sim$ 350	323/-

Table 4.1: Characteristic temperatures obtained from DSC and magnetization measurements for $Ni_{50}Mn_{34}In_{16-x}Ga_x$ ($x = 2$ and 4).

the magnetization decreases with decreasing temperature as can be seen from the slope of the 350 and 300 K-curves. For $T < 300$ K, $M(H)$ shows a curvature due to the presence of ferromagnetic short-range ordering. Below T_C^M, at 50 K, $M(H)$ initially rises rapidly but saturation is not reached, as is also the case at 5 K. The coexistence of AF interactions within the FM state is the origin of non-saturation (see Sec. 4.3.2).

Strain measurements

Another important property of $Ni_{50}Mn_{34}In_{16}$ is magnetic superelasticity [5]. As discussed in section 2.2, when a magnetic field is applied below M_s, the sample displays large strains. The magnetic-field-dependence of the strain $\Delta l/l(H)$ is shown in Fig. 4.10 for polycrystalline $Ni_{50}Mn_{27}Ga_{23}$, $Ni_{50}Mn_{34}In_{16}$ and $Ni_{50}Mn_{34}In_{14}Ga_2$ alloys at 240 K, 195 K and 265 K, respectively. These selected temperatures are just below A_s of each sample. The measurement sequences for each sample are indicated by arrows. The relative length-change was calculated with respect to the sample length at zero field l_0.

The application of a magnetic field to $Ni_{50}Mn_{27}Ga_{23}$ (Fig. 4.10(a)) causes a strain of about 0.04% in the initial curve. When the field is removed, the original value is not recovered. The residual strain is 0.03% in zero-magnetic field. Cycling the magnetic field leads to a small relative change of about 0.013% in 5 T, and the absolute strain remains almost constant at about 0.043%. This behavior is caused by field-induced twin boundary motion [1,87]. When a field is applied in the initial state, the strong magnetocrystalline anisotropy causes the rotation of the martensite variants leading to a length-change. The driving force for the rotation is provided by the difference in Zeeman energy of neighboring variants.

$\Delta l/l(H)$ for $Ni_{50}Mn_{34}In_{16}$ is seen in Fig. 4.10(b). The application of a magnetic field produces a length of about 0.14% in the initial curve. After the first field-cycle is completed, the strain reduces to about 0.12%. When the field is removed, the original strain is recovered each time. The magnetic field-induced strain is reversible when the magnetic field is cycled. The reorientation of variants in the martensitic state are not observed in $\Delta l/l(H)$ for this alloy. In $Ni_{50}Mn_{34}In_{16}$, the length change is caused by the crystallographic transformation from martensite to austenite with increasing field. The evolution of the neutron diffraction pattern with applied field taken at 180 K ($T < M_s$) shows that the external field drives the reverse martensitic transformation [5].

In Fig. 4.10(c), the strain increases rapidly to 0.11% for $Ni_{50}Mn_{34}In_{14}Ga_2$ in the initial curve. When the field is removed, the original strain is not recovered as in $Ni_{50}Mn_{27}Ga_{23}$,
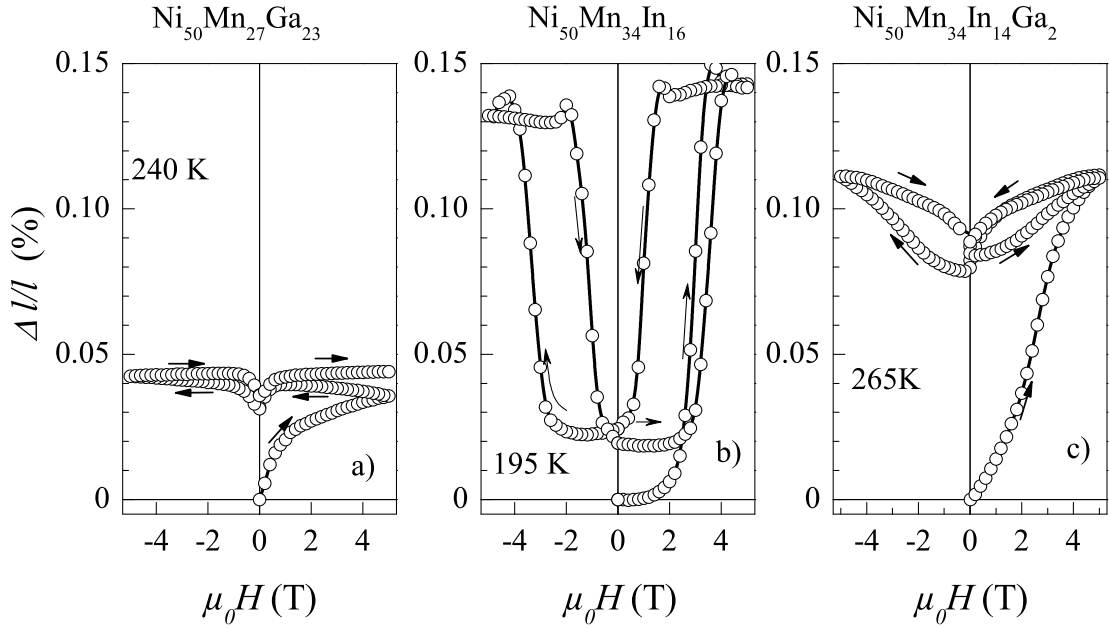
Figure 4.10: $\Delta l/l$ versus magnetic field up to 5 T for (a) $Ni_{50}Mn_{27}Ga_{23}$, (b) $Ni_{50}Mn_{34}In_{16}$ and (c) $Ni_{50}Mn_{34}In_{14}Ga_2$ at 240, 195, and 265 K, respectively. The data for $Ni_{50}Mn_{34}In_{16}$ are taken from [4].

and the residual strain is nearly 0.09%. The amount of maximum strain reduces to 0.03% after the field cycle is completed and then remains constant. The magnetic superelasticity weakens in $Ni_{50}Mn_{34}In_{14}Ga_2$ compared to that in $Ni_{50}Mn_{34}In_{16}$. However, the similarity of the initial increase in strain and its irreversibility on further cycling the field in $Ni_{50}Mn_{34}In_{14}Ga_2$ to that of $Ni_{50}Mn_{27}Ga_{23}$ suggests that twin boundaries become more mobile on small amounts of Ga substitution for In.

4.1.2   Sn substitution: $Ni_{50}Mn_{34}In_{15}Sn_1$

Magnetic and magnetocaloric properties

Fig. 4.11(a) shows the temperature dependence of the AC susceptibility $\chi(T)$ recorded in the range $150 < T < 300$ K on heating and cooling. Multiple peaks occur during the martensitic transition which is possibly associated with the occurrence of an inter-martensitic transformation or a secondary phase. From the cooling curves, $M_s \approx 244$ K and the secondary transformation temperature is about 228 K. The inset shows the

calorimetric curves dQ/dT on heating and cooling in the range $200 \leq T \leq 280$ K. The characteristic transition temperatures $M_s= 243$ K, $M_f= 226$ K, $A_s= 241$ K and $A_f= 253$ K are obtained from DSC measurements. The results of calorimetric measurements and $\chi(T)$ agree well and M_s remain almost constant by 1% Sn substitution for In while e/a increases. $M(T)$ for $Ni_{50}Mn_{34}In_{15}Sn_1$ in 5 mT is shown in Fig. 4.11(b). At high temperatures, in the austenitic state, the sample is paramagnetic and orders ferromagnetically at $T_C^A=305$ K and runs at the demagnetizing limit with decreasing temperature down to M_s. $M(T)$ indicates a higher value of $M_s=252$ K than DSC and $\chi(T)$. Below M_s, the austenite state loses its stability and $M(T)$ drops. On further cooling, the sample orders ferromagnetically at $T_C^M=225$ K. At this temperature, a large separation between ZFC and FC curves is observed as in $Ni_{50}Mn_{34}In_{15}Sn_1$.

The magnetization isotherms in the vicinity of M_s are shown in Figs. 4.12(a) and (b) for $Ni_{50}Mn_{34}In_{16}$ and for $Ni_{50}Mn_{34}In_{15}Sn_1$ respectively. The data shown with open red circles in both figures correspond to $M(H)$ for $T < M_s$ and indicate the presence of a field-induced transition. The filled circles correspond to $T > M_s$. In the range
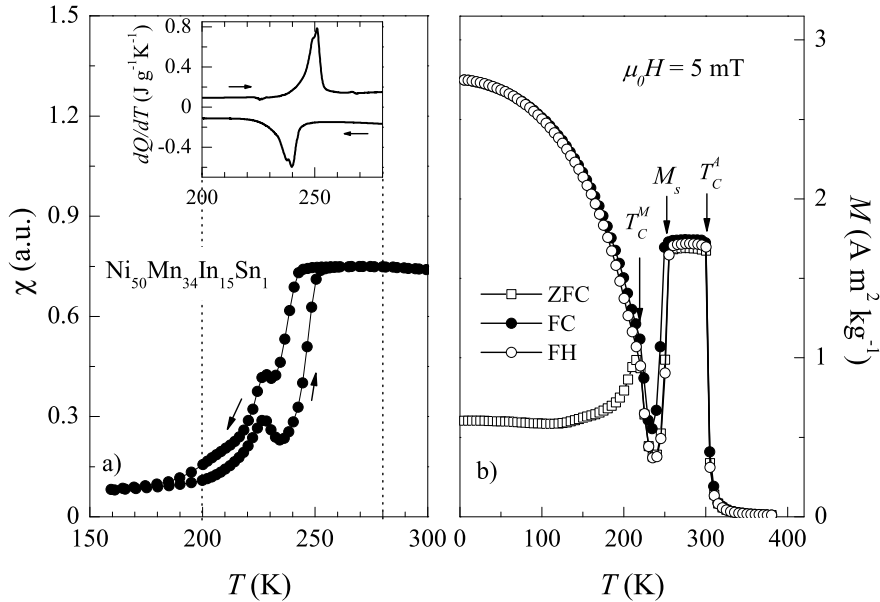
Figure 4.11: (a) Temperature dependence of the ac susceptibility and (b) ZFC, FC, and FH-$M(T)$ in 5 mT of $Ni_{50}Mn_{34}In_{15}Sn_1$. The inset shows dQ/dT versus temperature for $Ni_{50}Mn_{34}In_{15}Sn_1$ recorded on heating and cooling. Vertical arrows indicate the position of T_C^A, M_s, and T_C^M.

$M_s \leq T \leq T_C^A$, $M(H)$ does not saturate indicating that even in the austenitic state, the ferromagnetic state is not pure and incorporates non-ferromagnetic entities. The metamagnetic-like character of the feature in $M(H)$ at temperatures $T < M_s$ becomes more pronounced in $Ni_{50}Mn_{34}In_{15}Sn_1$.

The entropy change ΔS around M_s in $Ni_{50}Mn_{34}In_{15}Sn_1$ determined from $M(H)$ data is shown in Fig. 4.13(a). $\Delta S(T)$ is positive and shows an inverse MCE around $T < M_s$. The maximum entropy change for $Ni_{50}Mn_{34}In_{15}Sn_1$ is 20.6 $Jkg^{-1}K^{-1}$ which is reached already at 3 T, and does not change any further when the field is increased up to 5 T. This value is higher than that in $Ni_{50}Mn_{34}In_{16}$ for which $\Delta S = 8$ $Jkg^{-1}K^{-1}$ at 5 T. The rate of change of ΔS with respect to field up to 3 T is ~ 7 $Jkg^{-1}K^{-1}T^{-1}$ for $Ni_{50}Mn_{34}In_{15}Sn_1$ and ~ 2 $Jkg^{-1}K^{-1}T^{-1}$ for $Ni_{50}Mn_{34}In_{16}$.

The temperature dependence of ΔT_{ad} for $Ni_{50}Mn_{34}In_{15}Sn_1$ is shown in Fig. 4.13(b). The sample cools by about 6 K below M_s and warms by 2 K at room temperature
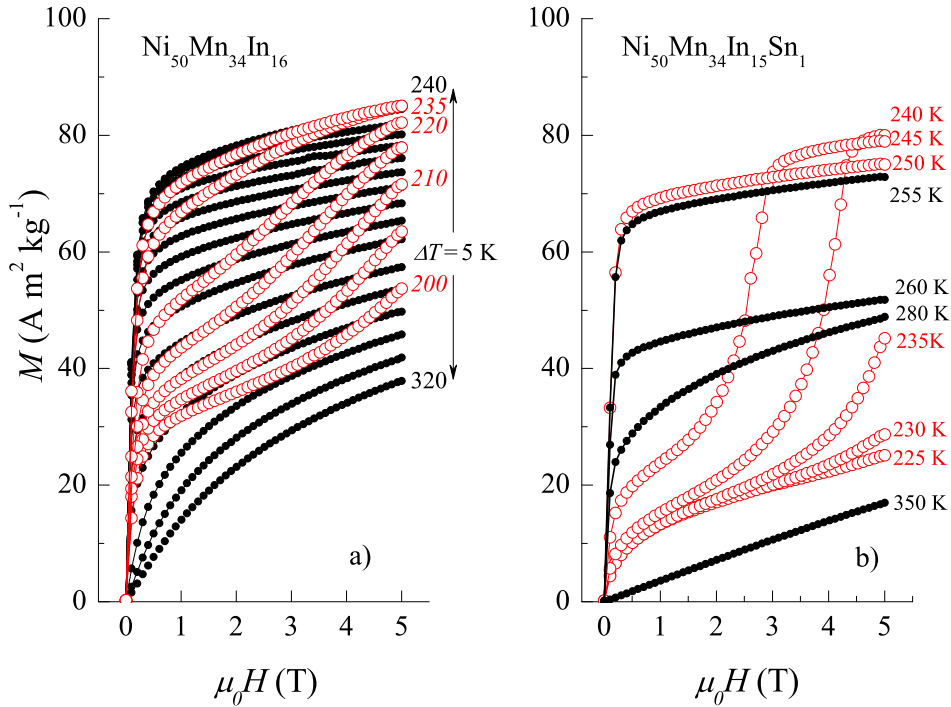
Figure 4.12: Magnetic-field-dependence of the magnetization for (a) $Ni_{50}Mn_{34}In_{16}$ at $200 \leq T \leq 320$ K in 5 K steps and (b) $Ni_{50}Mn_{34}In_{15}Sn_1$ at selected temperatures. Open circles (red) and filled circles are data for $T < M_s$ and $T > M_s$ respectively. The data for $Ni_{50}Mn_{34}In_{16}$ are shown again for comparison.
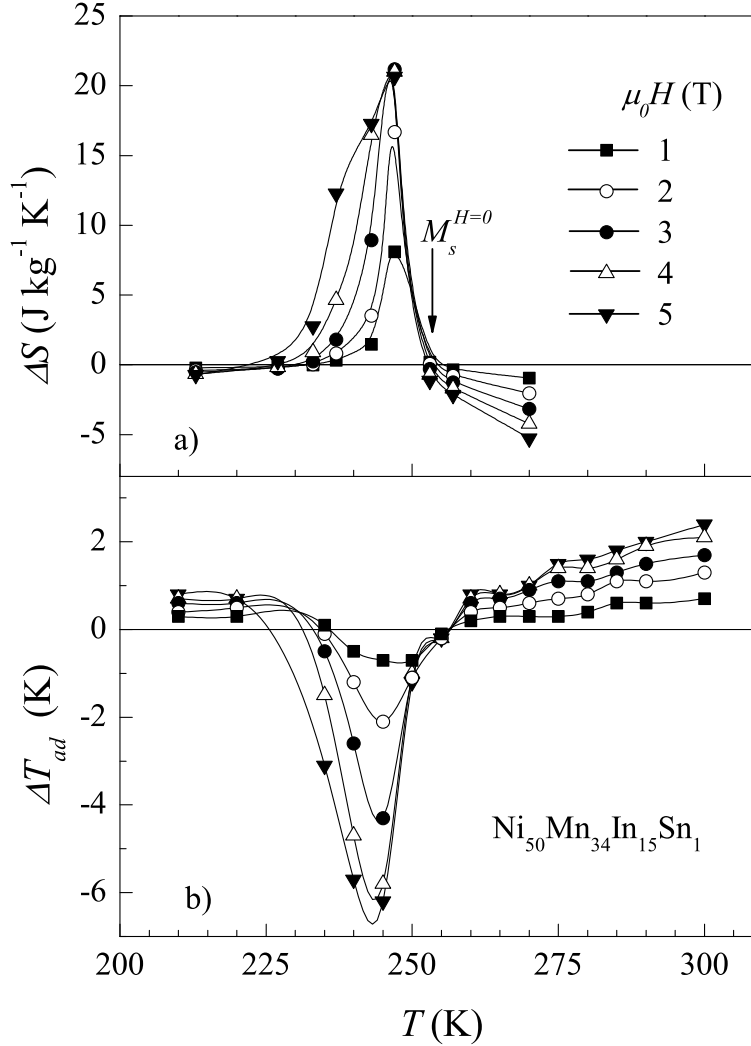
Figure 4.13: (a) $\Delta S(T)$ and (b) $\Delta T_{ad}(T)$ around M_s in $Ni_{50}Mn_{34}In_{15}Sn_1$.

under 5 T magnetic field, whereas in $Ni_{50}Mn_{34}In_{16}$, these values are 2 K and 3.5 K respectively (see Fig. 4.7(a)). The rate of change of the MCE with respect to field for the Sn-substituted sample is 1.2 KT^{-1} which is higher than that in $Ni_{50}Mn_{34}In_{16}$ (0.4 KT^{-1}). Further increase in Sn concentration suppresses the martensitic transformation.
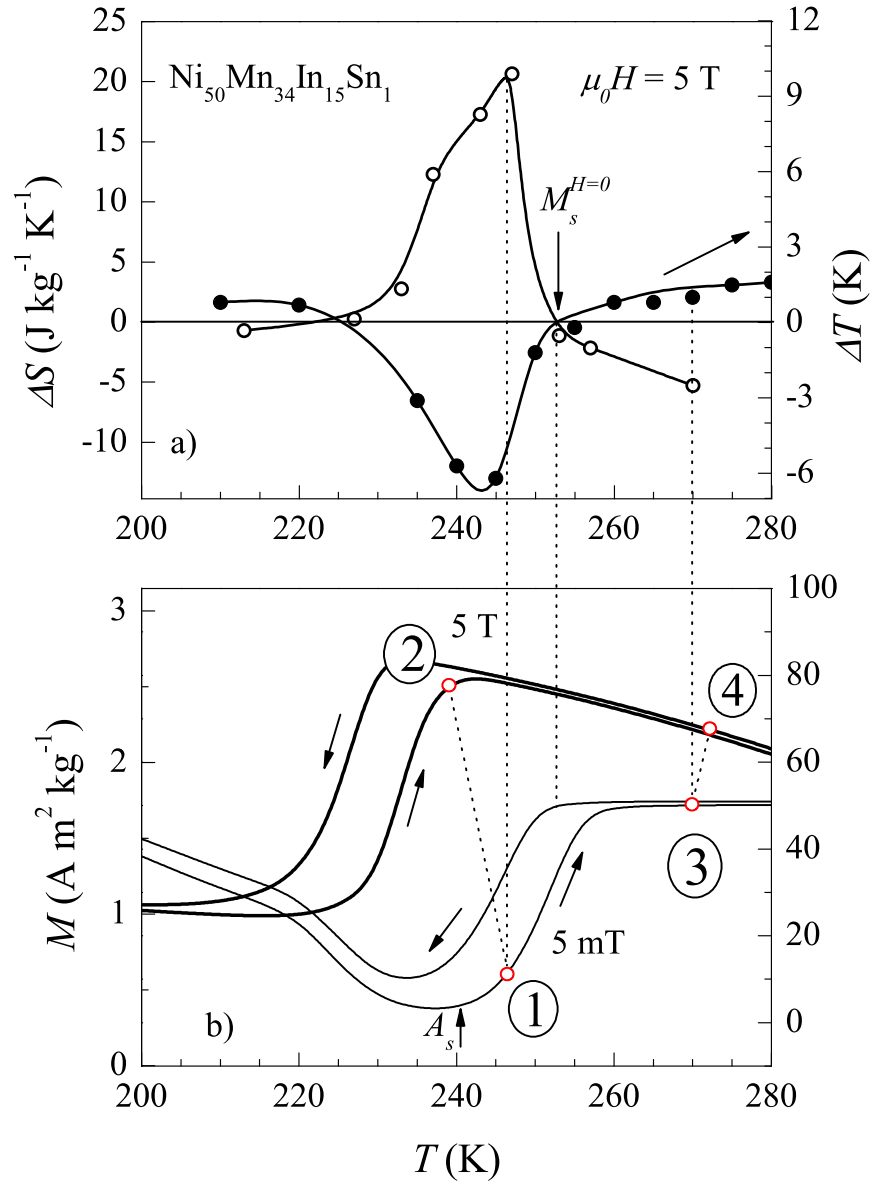
Figure 4.14: (a) The temperature dependence of $\Delta S(T)$ (open symbols) and $\Delta T(T)$ (filled symbols) in 5 T. (b) $M(T)$ in 5 mT and 5 T for $Ni_{50}Mn_{34}In_{15}Sn_1$. The encircled 1 and 3 represent two chosen initial states of the alloy before a field of 5 T is applied adiabatically. 2 and 4 are the final states with respect to $M(T)$ after a field of 5 T is applied.

The inverse magnetocaloric properties are strongly related to the shift of M_s in a magnetic field (see Fig. 2.12). Figure 4.14(a) shows $\Delta T_{ad}(T)$ and $\Delta S(T)$ for $Ni_{50}Mn_{34}In_{15}Sn_1$ under a 5 T magnetic-field-change. This material cools below M_s and warms above M_s when the magnetic field is applied adiabatically. $M(T)$ in applied fields of 5 mT and 5 T are shown in Fig. 4.14(b). The shift of M_s is about -20 K in 5 T with respect to $M(T)$. The maximum in $\Delta S(T)$ is located at a temperature slightly above A_s (point 1) in the 5 mT $M(T)$-data as shown by the vertical dotted line. Applying a 5 T magnetic field adiabatically at this temperature, where the sample contains mixed austenite and martensite phases, causes a decrease in temperature of about 6 K. This carries the state of the sample from point 1 to point 2 located in the 5 T-$M(T)$ curve where the sample is essentially austenite. The shift of M_s under an applied magnetic field is mostly responsible for the cooling as was modelled in Fig. 2.12. On the other hand, a field of 5 T applied adiabatically above M_s at point 3 leads to a 1 K rise within the austenitic state (point 4) caused by the conventional MCE. The crystallographic state of the sample does not change in this process. Accordingly, one can expect a maximum value of ΔT_{ad} equal to the value of the hysteresis shift (or M_s shift).

Strain measurements

The strain versus magnetic field measurements are shown in Fig. 4.15(a), (b) and (c) for $Ni_{50}Mn_{35}Sn_{15}$ [4], $Ni_{50}Mn_{34}In_{16}$ [4] and $Ni_{50}Mn_{34}In_{15}Sn_1$ alloys, respectively. The data for $Ni_{50}Mn_{34}In_{16}$ are shown again for comparison. $Ni_{50}Mn_{35}Sn_{15}$ shows a weak strain on applying a magnetic field in the martensitic state at 120 K (Fig. 4.15(a)). The relative length change is about 0.002%. The effect is reversible, and it is due to conventional magnetostriction. In $Ni_{50}Mn_{35}Sn_{15}$, a magnetic field of 5 T is not sufficient to induce a martensitic transition as it is for $Ni_{50}Mn_{34}In_{16}$ [86].

Fig. 4.15(c) shows the magnetic-field-dependence of the relative strain at 242 K for $Ni_{50}Mn_{34}In_{15}Sn_1$. The initial application of a magnetic field causes a 0.015% shrinkage of the sample up to 3 T. Afterwards, the length change increases rapidly. It reaches a maximum value of 0.075% in 4 T, and a further increase of the magnetic field up to 5 T causes a 0.015% decrease in the length change. When the field is decreased, the length change remains almost constant down to 2 T. At this field, the strain is recovered to a reversible value 0.075%. Only 1% Sn substitution for In in $Ni_{50}Mn_{34}In_{16}$ is sufficient to decrease strongly the value of the field-induced-strain. This is due to the fact that $Ni_{50}Mn_{35}Sn_{15}$ shows a weak strain associated with the magnetostriction of
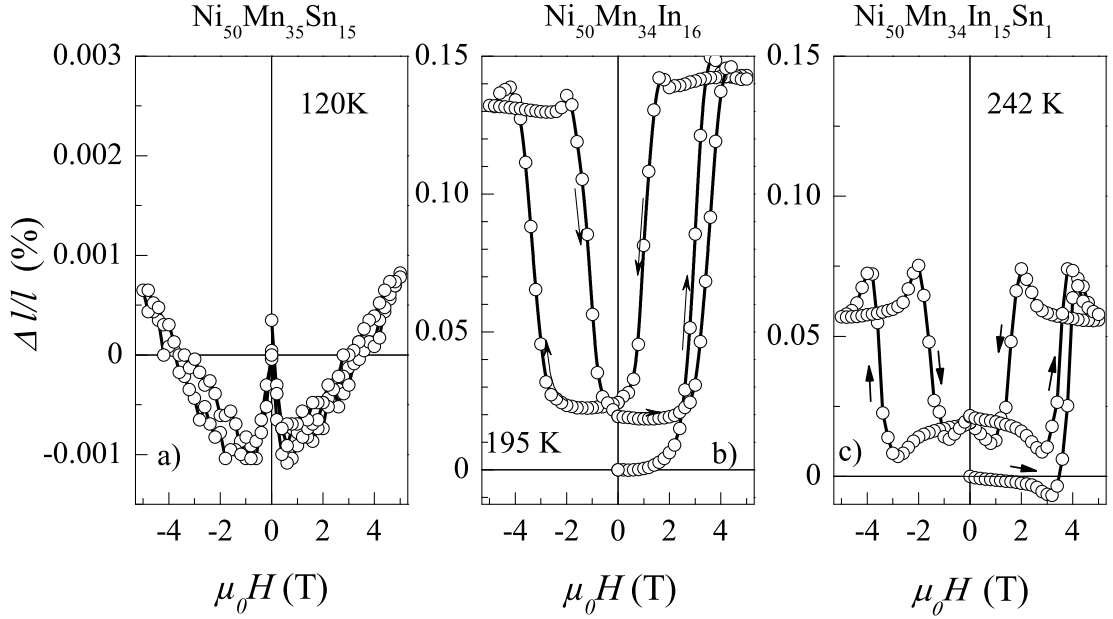
Figure 4.15: $\Delta l/l$ versus magnetic field up to 5 T for (a) $Ni_{50}Mn_{35}Sn_{15}$, at 120 K, (b) $Ni_{50}Mn_{34}In_{16}$ at 195 K and (c) $Ni_{50}Mn_{34}In_{15}Sn_1$ at 242 K, respectively. The graphs in (a) and (b) are taken from [4] for comparison.

the martensite. However, the magnetic superelasticity is preserved in $Ni_{50}Mn_{34}In_{15}Sn_1$, and the features in $\Delta l/l(H)$ around the maximum strain values stand out more in $Ni_{50}Mn_{34}In_{15}Sn_1$ than in $Ni_{50}Mn_{34}In_{16}$ (Fig. 4.15(b) and (c)).

The field dependence of magnetization of $Ni_{50}Mn_{34}In_{15}Sn_1$ for $0 \leq H \leq 5$ T at 245 K is shown in Fig. 4.16. The open circles show the initial curve, in which the metamagnetic transition is seen around 2.5 T. The metamagnetic transitions are observed in the main loop at 2.5 T and 1 T for the increasing-field and decreasing-field branches, respectively. The curves are symmetric around the origin. The features observed in Fig. 4.15(c) between 2 T and 4 T for the increasing-field branch can be related to the metamagnetic transitions in this magnetic field range. As in the case of $\Delta l/l(H)$, $M(H)$ also displays essentially no remanence and recovers its zero-field value.

4.1.3   Summary

The MCE in $Ni_{50}Mn_{34}In_{16}$ and its quaternary compounds $Ni_{50}Mn_{34}In_{14}Ga_2$ and $Ni_{50}Mn_{34}In_{15}Sn_1$ have been investigated. In $Ni_{50}Mn_{34}In_{16}$, $\partial M/\partial T < 0$ at T_C^A and
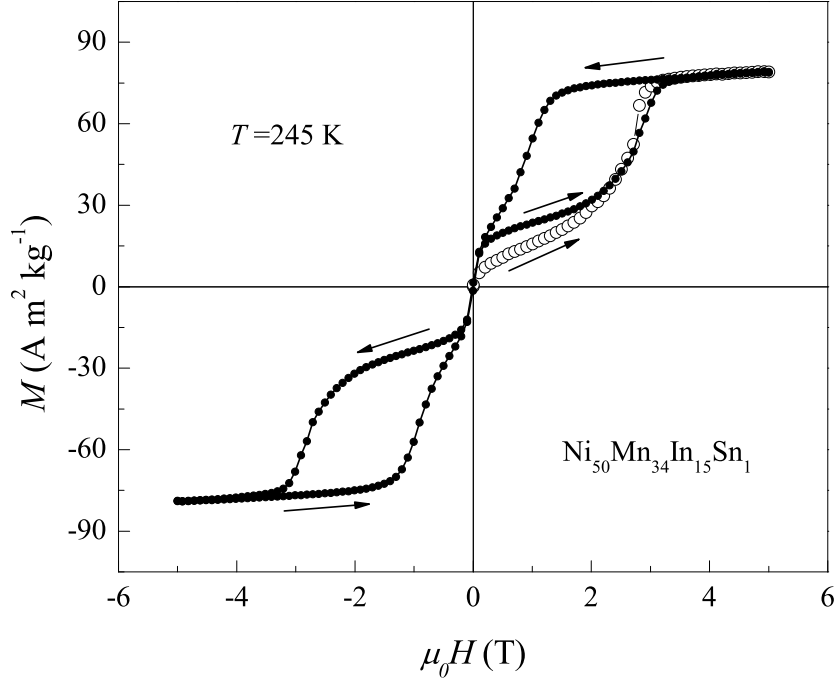
Figure 4.16: Magnetic hysteresis loop at 245 K for $Ni_{50}Mn_{34}In_{15}Sn_1$. The open circles indicate the initial curve.

$\partial M/\partial T > 0$ below M_s. According to Eq. 7, the conventional and the inverse MCE are observed around T_C^A and below M_s, respectively. The maximum in $\Delta T_{ad}(T)$ (or minimum in $\Delta S(T)$) and the minimum in $\Delta T_{ad}(T)$ (or maximum in $\Delta S(T)$) are related to the conventional MCE and the inverse MCE, respectively. In $Ni_{50}Mn_{34}In_{16}$, $\Delta S = -5$ $Jkg^{-1}K^{-1}$ at T_C^A and $\Delta S = 8$ $Jkg^{-1}K^{-1}$ below M_s under a 5 T magnetic field change. When a 5 T magnetic field is applied adiabatically at T_C^A, the sample warms about 3.5 K and cools 2 K when the field is applied below M_s (see figures 4.6 and 4.7).

Since $Ni_{50}Mn_{37}Sn_{13}$ exhibits a large inverse MCE, one can expect that Sn substitution in $Ni_{50}Mn_{34}In_{16}$ could enhance its inverse MCE . Indeed, when 1% Sn is substituted for In, ΔS increases from 8 to 21 J $kg^{-1}K^{-1}$ under 5 T magnetic field change below M_s, and the sample cools by about 6.5 K adiabatically. Therefore, the magnetocaloric properties are enhanced by Sn substitution; and by Ga substitution, M_s is shifted to around room temperature without altering ΔS (or ΔT_{ad}).

Fig. 4.17 shows the maximum in the inverse MCE represented by ΔS_{max} and ΔT_{ad}^{max}

as a function of magnetic field change $\mu_0 \Delta H$ in $Ni_{50}Mn_{34}In_{16}$, $Ni_{50}Mn_{34}In_{14}Ga_2$ and $Ni_{50}Mn_{34}In_{15}Sn_1$. For $Ni_{50}Mn_{34}In_{16}$ and $Ni_{50}Mn_{34}In_{14}Ga_2$, ΔS_{max} increases and ΔT_{ad}^{max} decreases with increasing $\mu_0 \Delta H$ in a similar manner. For $Ni_{50}Mn_{34}In_{15}Sn_1$, ΔS_{max} is significantly larger than in $Ni_{50}Mn_{34}In_{16}$. It increases rapidly up to 3 T, and above this value, ΔS_{max} is nearly independent of $\mu_0 \Delta H$ and remains constant up to 5 T. However, ΔT_{ad}^{max} continues to increase negatively above 3 T and reaches almost 7 K under 5 T (Fig. 4.17(b)).

Fig. 4.18 shows the conventional MCE around T_C^A in $Ni_{50}Mn_{34}In_{16}$, $Ni_{50}Mn_{34}In_{14}Ga_2$ and $Ni_{50}Mn_{34}In_{15}Sn_1$. ΔS increases negatively with almost linear behavior for all alloys with increasing $\mu_0 \Delta H$ with the slope being largest for $Ni_{50}Mn_{34}In_{15}Sn_1$. This shows
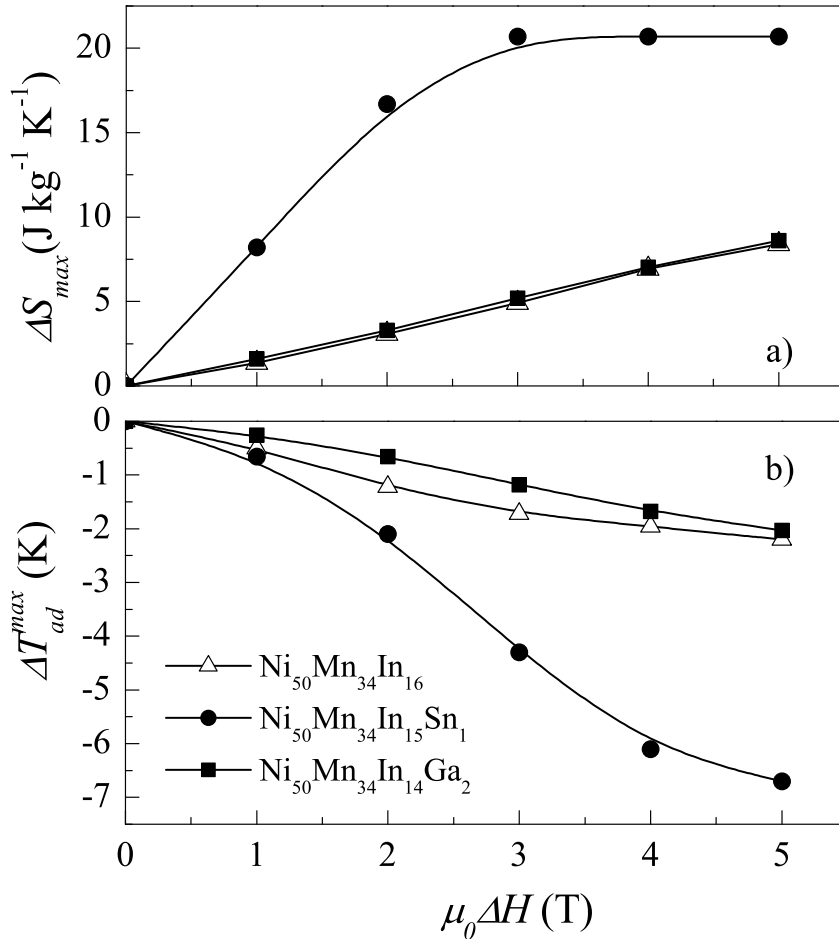
Figure 4.17: The field dependence of (a) ΔS and (b) ΔT_{ad} below M_s for $Ni_{50}Mn_{34}In_{16}$, $Ni_{50}Mn_{34}In_{15}Sn_1$ and $Ni_{50}Mn_{34}In_{14}Ga_2$.
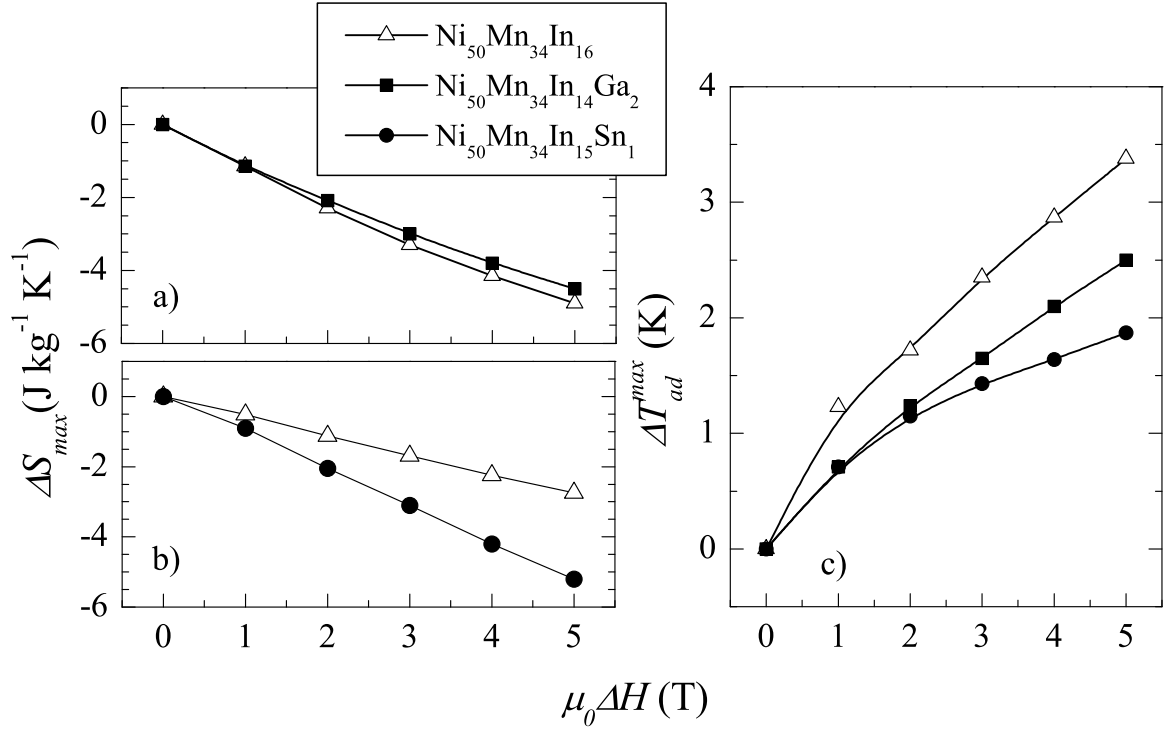
Figure 4.18: The field dependence of ΔS (a) at T_C^A, (b) at 270 K, and (c) the field dependence of ΔT_{ad} at T_C^A for $Ni_{50}Mn_{34}In_{16}$, $Ni_{50}Mn_{34}In_{15}Sn_1$ and $Ni_{50}Mn_{34}In_{14}Ga_2$.

that Sn substitution enhances also the conventional MCE just as it enhances the inverse MCE.

Fig. 4.18(c) shows ΔT_{ad}^{max} as a function of $\mu_0 \Delta H$, where it is seen that the samples warm on applying a magnetic field in the austenitic state. Substitution of Ga or Sn for In decreases ΔT_{ad}^{max} with respect to that for $Ni_{50}Mn_{34}In_{16}$. Particularly in $Ni_{50}Mn_{34}In_{15}Sn_1$, the expected ΔT_{ad}^{max} values are higher because of the higher negative ΔS_{max}. However, the measured ΔT_{ad} is lower than the values in $Ni_{50}Mn_{34}In_{16}$. At T_C^A, the transformation is second-order, and ΔT_{ad} is the difference between the total entropy curves for $H = 0$ and $H > 0$ at constant S. (see Fig. 2.10).

A relevant parameter characterizing magnetic refrigerator material is the refrigerant capacity q, which is a measure of heat transfer under an applied field and is calculated by integrating $\Delta S(T)$. Gd is presently the most suitable refrigerant material for which q=542 Jg^{-1}. In $Ni_{50}Mn_{34}In_{16}$, $q = 223$ Jg^{-1} and it decreases to 144 Jg^{-1} with 2% Ga substitution for In. In $Ni_{50}Mn_{34}In_{15}Sn_1$, q increases to 262 Jg^{-1}.

4.2 Effect of External Magnetic Field on the Structure of Heusler Alloys

The effect of an external magnetic field on the structure of Ni-Mn-Z Heusler alloys is studied, and the results are presented in the next two sections. In the following, the term cooling-field is used to refer to an external magnetic field that is applied in the austenitic state, after which the temperature is decreased to a value in the martensitic state. The temperature dependence of the strain $(\Delta l/l)(T)$ and the change of the crystallographic structure under an applied cooling-field are discussed. The latter is examined by neutron diffraction.

4.2.1 Strain under field: Estimation of the easy-axis of magnetization

Ni-Mn-based magnetic shape memory alloys show large magnetic-field-induced strains related to strong magneto-elastic coupling in the martensitic state. Such a large strain under a cooling-field has previously been observed in a single-crystalline Ni$_2$MnGa as shown in Fig. 4.19 [1]. In the martensitic state, twin variants align along their easy magnetization direction under an external cooling-field by the motion of the mobile twin-boundaries (see section 2.2), and this can result in large macroscopic strains. The alignment of the variants along the easy-axis (the short $c-$axis in Ni-Mn-Ga) under a magnetic field produces the large strain. We investigate the temperature dependence of the strain $\Delta l/l$ in constant cooling-field around the martensitic transformation.

Fig. 4.20 shows $(\Delta l/l)(T)$ measured under the cooling-fields of 0, 2 and 5 T for Ni$_{50}$Mn$_{50-x}Z_x$ ternary alloys where Z is Ga, In, Sn and Sb. The relative length-change $\Delta l/l$ is normalized to the value at 300 K. For Ni$_{50}$Mn$_{27}$Ga$_{23}$ shown in Fig. 4.20(a), a weak hysteretic feature is found in the temperature-range corresponding to the martensitic transition in the absence of a magnetic-field as in the case of the single crystal sample in Fig. 4.19. Substantial difference in the macroscopic dimensions between the austenitic and martensitic states is not found at M_s. A negligible change in volume of the unit cells of austenite and martensite was reported in diffraction experiments [88]. However, when the sample is cooled through M_s under 2 T, a large difference in the strain $\Delta\varepsilon\sim$ -0.4% between the austenitic and martensitic states occurs. Further increasing the cooling-field up to 5 T, causes only an insignificant further increase in $\Delta\varepsilon$.

Ni$_{50}$Mn$_{35}$Sn$_{15}$ undergoes a martensitic transformation at about 120 K. As seen in Fig. 4.20(b), cooling in the absence of a magnetic-field leads to a sudden drop in $\Delta l/l$

at M_s. This drop indicates that there is a volume difference between the austenitic and martensitic states. The presence of volume-change is also shown by temperature-dependent neutron diffraction experiments [88]. Cooling in the presence of a magnetic-field causes M_s (indicated by arrows) to drop at a rate of about -3 KT^{-1}. At the same time, the difference in strain between the austenitic and martensitic states increases with increasing magnetic field as in the case of $Ni_{50}Mn_{27}Ga_{23}$ in Fig. 4.20(a). Twin-boundary mobility in $Ni_{50}Mn_{35}Sn_{15}$ is weak, so that only little magnetic-field-induced strain ($\sim 10^{-5}$) is observed in fields up to 5 T (Fig. 4.15(a)). Therefore, the large change in strain ($\sim 10^{-3}$) between the austenitic and martensitic states should be related to the effect of the magnetic cooling-field providing a preferred orientation to the martensite
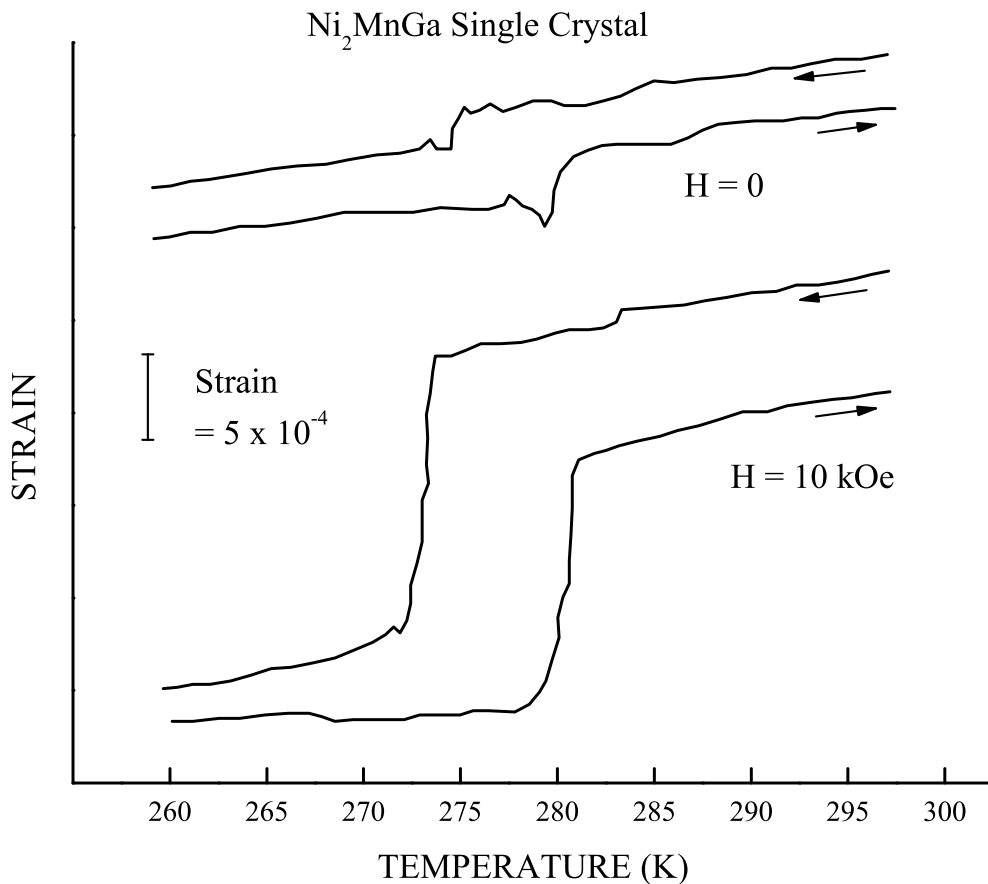
Figure 4.19: Strain as a function of temperature in zero field and in 10 kOe for single-crystalline Ni_2MnGa. The two curves have been displaced relative to each other along the strain axis for clarity. This figure is adapted from reference [1].
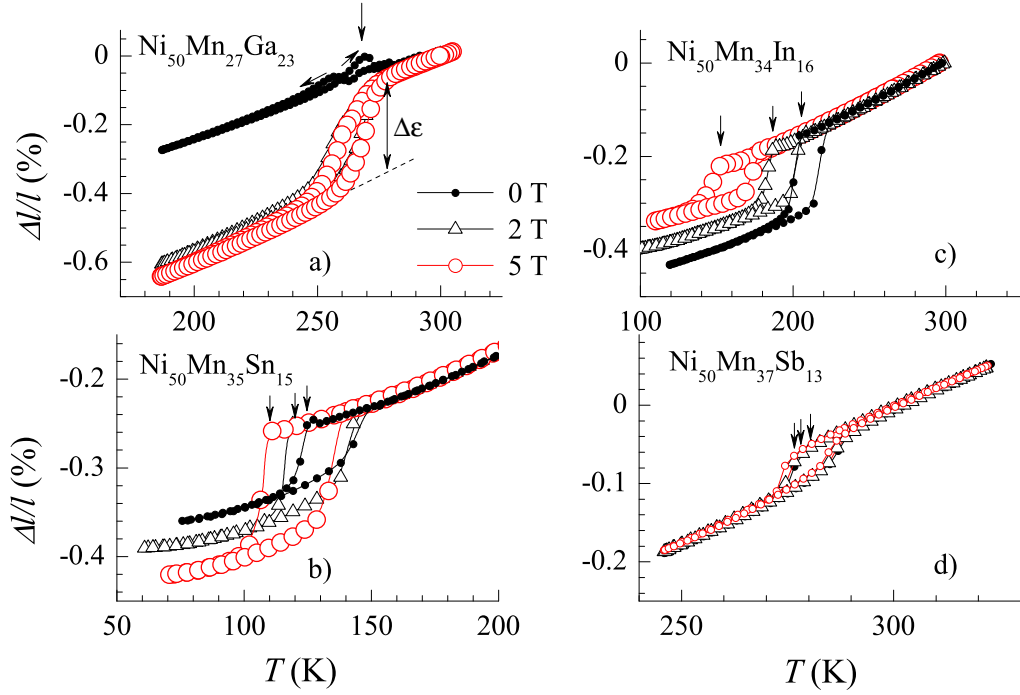
Figure 4.20: $\Delta l/l$ versus temperature under 0, 2, and 5 T for (a) $Ni_{50}Mn_{27}Ga_{23}$, (b) $Ni_{50}Mn_{35}Sn_{15}$, (c) $Ni_{50}Mn_{34}In_{16}$ and (d) $Ni_{50}Mn_{37}Sb_{13}$. Vertical arrows indicate M_s.

variants during their nucleation.

The behavior is opposite in $Ni_{50}Mn_{34}In_{16}$ as seen in Fig. 4.20(c). The cooling-field causes a decrease in $\Delta l/l$ between the austenitic and the martensitic states. The absolute value of $\Delta\varepsilon$ decreases from about 0.2% to 0.1%. The rate of change of M_s with applied field for this sample is about -10 KT^{-1}, which is nearly 3 times larger than for $Ni_{50}Mn_{35}Sn_{15}$. The data for $Ni_{50}Mn_{37}Sb_{13}$ is shown in Fig. 4.20(d). Here, the rate of decrease of M_s with applied field is about -1 KT^{-1}. There is a weak relative length-change of about -0.03% between the austenitic and martensitic states under an applied cooling-field of 5 T.

The relative length-change under a cooling-field in alloys where Ga and Sn are substituted for In is shown in Fig. 4.21. M_s, indicated with arrows in Fig. 4.21(a) and Fig. 4.21(b), decreases with increasing cooling-field. The substitution of 2% Ga shifts M_s from 275 K to about 257 K and 1% Sn shifts it from 250 K to 231 K in an applied field of 5 T with a rate about -3 KT^{-1} and -4 KT^{-1}, respectively. The influence of the external cooling-field on the nucleation is weaker in $Ni_{50}Mn_{34}In_{14}Ga_2$, and $\Delta\varepsilon$ increases
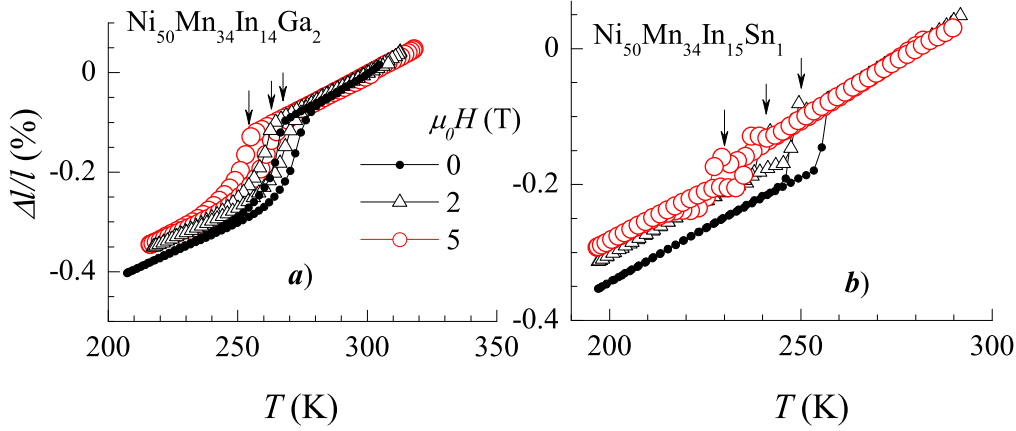
Figure 4.21: $\Delta l/l$ versus temperature under 0, 2, and 5 T for quaternary Heusler alloys (a) $Ni_{50}Mn_{34}In_{14}Ga_2$ and (b) $Ni_{50}Mn_{34}In_{15}Sn_1$. Vertical arrows indicate M_s.

slightly from -0.2% to -0.1%. Here, we observe that the decrease in $\Delta l/l$ below M_s is broader than in the case of $Ni_{50}Mn_{27}Ga_{23}$. In $Ni_{50}Mn_{34}In_{15}Sn_1$, $\Delta\varepsilon$ increases from -0.1% to -0.04%.

In general, when a martensitic material is cooled through M_s under zero applied field, the martensitic variants form as twin-related self-organized structures in order to minimize the elastic energy associated with the change of the unit-cell. When the material cools through M_s under an applied magnetic field, martensite variants can grow with a preferred orientation. Fig. 4.22 shows schematically the effect of a cooling-field on martensite nucleation. In this figure, each twin variant is represented by tetragonal units of length l, which themselves are built up of a tetragonal unit-cells. Twin structures with easy-direction[a] of magnetization along the long-axis and along the short-axis in the absence of field and under an applied cooling-field are taken into account in the upper and lower panels, respectively. If the easy-direction is the long-axis, the sample-length measured along the field direction increases by an amount δ to $l + \delta$. If the easy-direction is the short-axis, the sample-length decreases to $l - \delta$. Therefore, it is possible to obtain information on the easy direction of magnetization in the martensitic

---

[a]The easy-direction refers to the energetically favorable direction of the spontaneous magnetization in a ferromagnetic material. This direction is determined by various factors, including the magnetocrystalline anisotropy and the shape anisotropy in single crystalline materials. In the $L1_0$ tetragonal phase, having two a-axes and a c-axis, or in any modulated martensitic structure, the magnetization tends to lie either in a plane bounded by the a-axes or along the c-axis of the unit cell.
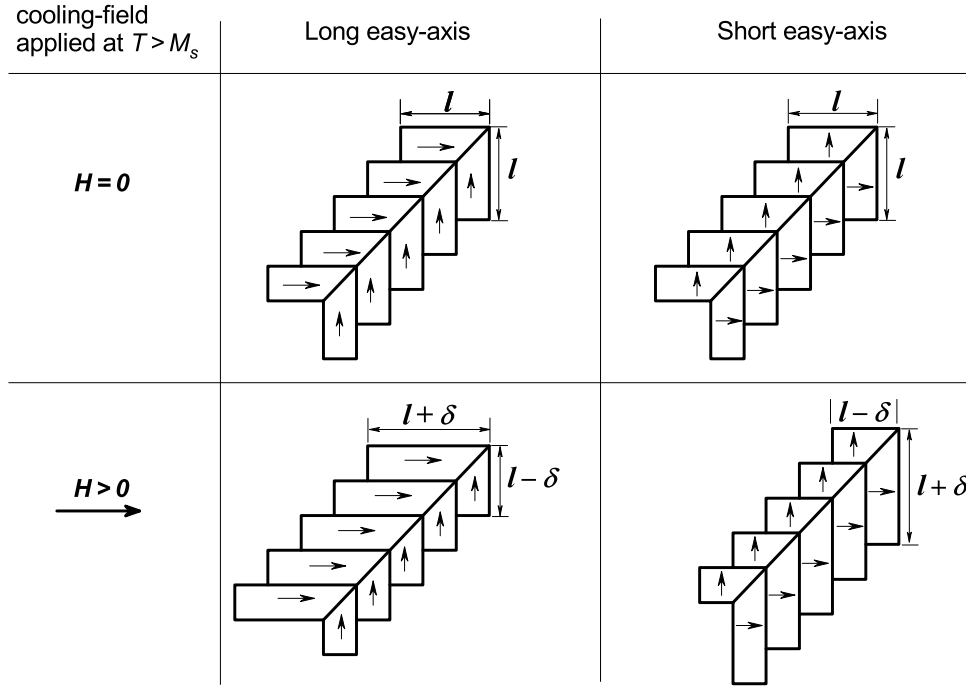
Figure 4.22: Schematic representation of ferromagnetic martensite nucleation with and without a cooling magnetic-field applied at $T > M_s$. Twins are represented with tetragonal units of length l built up of self-similar tetragonal unit-cells. There is no preferred variant growth during martensite nucleation when cooled in $H = 0$. Preferred variant growth during martensite nucleation occurs when the sample is cooled through M_s in $H > 0$, such that when the long-axis is the easy-axis, the length increases in field direction by δ. When the short-axis is the easy-axis the length decreases by δ in the field direction.

state by temperature-dependent strain measurements under a cooling-field.

Strain measurements in a single crystal of Ni-Mn-Ga had previously shown that in the martensitic state, the sample shrinks (or $\Delta\varepsilon$ increases) along the field direction due to the alignment of the short easy-direction of magnetization (c-axis) with the external magnetic field [1]. The high twin boundary mobility in Ni-Mn-Ga is the main cause of this effect (see section 2.2). When single and polycrystalline Ni-Mn-Ga alloys are compared, it is seen that the response of the strain under a cooling-field is similar for both as seen in Figs. 4.19 and 4.20(a). When Ni-Mn-Ga (single or polycrystalline) is cooled through M_s in the absence of a magnetic field, martensite variants grow without any preferred direction. Since the volume of the unit cell between the austenite and martensite phase are the same at the transition, a negligible strain change is observed. However, when a magnetic field is applied in the austenitic state and the sample is cooled through M_s, martensite variants nucleate and grow with a preferred orientation provided by the direction of the magnetic field. $\Delta l/l$ between austenite and marten-

site increases with respect to the zero-field measurement. The same increase of strain under magnetic field with respect to the zero-field measurement is also observed in $Ni_{50}Mn_{35}Sn_{15}$ (Fig. 4.20(b)). However, in the absence of a magnetic field, the sample shows a significant strain due to the difference in volume of the unit cells of austenite and martensite. Since $\Delta\varepsilon$ in $Ni_{50}Mn_{35}Sn_{15}$ increases with increasing magnetic field (or the sample-length decreases with increasing cooling-field), the easy-direction of magnetization in the martensitic state is expected to be along a short-axis as in $Ni_{50}Mn_{27}Ga_{23}$.

In $Ni_{50}Mn_{34}In_{16}$, $\Delta\varepsilon$ decreases under a cooling-field with respect to the strain in the absence of a magnetic field. This effect can be related to fact that the easy magnetization direction is along the long-axis. It can also be related to the austenite arrest effect which will be discussed in the next section.

4.2.2 Austenite arrest studied by neutron diffraction under magnetic field

The term kinetic arrest is used to describe the retarded growth of the low-temperature phase by the supercooled high-temperature phase in first-order transitions. An example for the kinetic arrest of magnetic phases can be given for the Ru-doped $CeFe_2$ pseudobinary alloy which exhibits a first-order FM/AF transition. When a magnetic field is applied in the FM phase, and the sample is cooled through the transition temperature to the AF phase, the FM phase is partially arrested [90]. Recently, kinetic arrest was found in FM Ni-Mn-In Heusler alloys where the martensitic transformation is arrested in the presence of magnetic cooling-fields [62]. Theoretical studies on Ni_2MnIn show that there is a strong tendency for the austenitic state to gain stability under an applied field [91].

In NiMnInCo, austenite arrest was reported from the results of temperature and field-dependent X-ray diffraction experiments [89]. Fig. 4.23 focuses on the (220) $L2_1$cubic
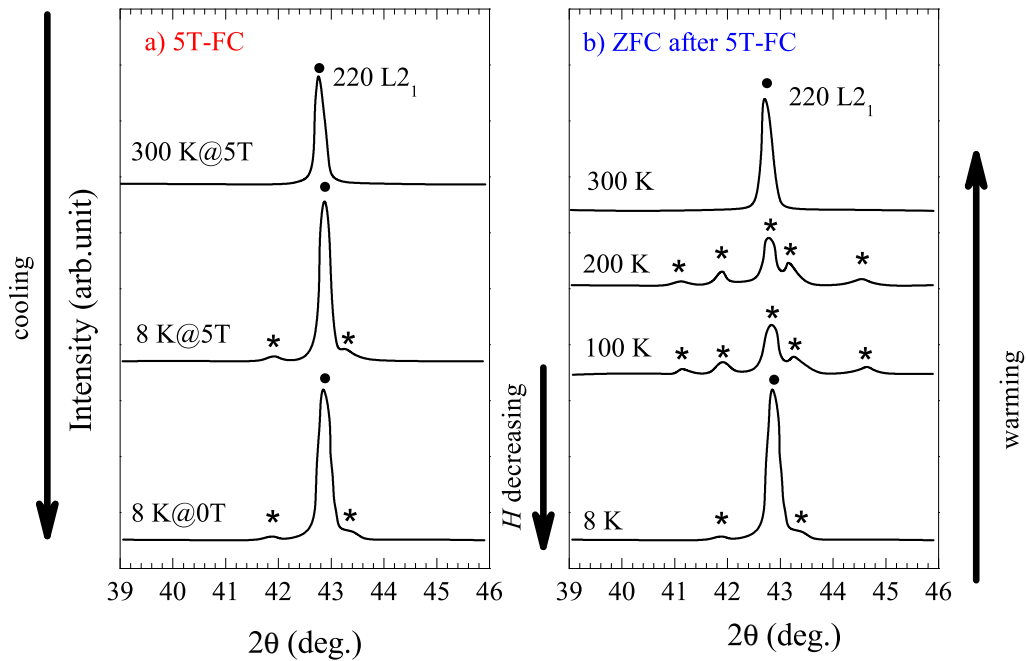
Figure 4.23: Temperature-dependent X-ray diffraction patterns (a) in 5 T field cooling and (b) ZFC after 5 T field cooling in NiCoMnIn (after [89]). The filled dotted symbols are related to the (220) reflection of $L2_1$ cubic structure, and the asteriks indicate the reflections related to the martensite phase.

reflection. During cooling under 5 T (FC), the austenite (220) reflection persists down to 8 K, where reflections related to the martensite phase are also present indicating that the martensitic transformation takes place partially (Fig. 4.23(b)). On removing the field and warming, the martensite quantity increases with increasing temperature, and at 100 K and 200 K, an increased number of reflections related to the martensite phase are observed in Fig. 4.23(b). At 300 K, the reverse transformation completes. The authors explain this freezing behavior at low temperatures to be due to the decrease of the mobility of the habit plane between the martensite and austenite phases and the loss of the driving force for the transformation on supercooling.

In this section, we present results on neutron diffraction for $Ni_{50}Mn_{27}Ga_{23}$, $Ni_{50}Mn_{35}Sn_{15}$, and $Ni_{50}Mn_{34}In_{16}$ at 300 K and 5 K in the absence of magnetic field and in 5 T cooling-field. The diffraction data are analyzed by the Fullprof program. The samples used in the following experiments have been prepared particularly for the neutron diffraction experiments, and the compositions are given in Table 3.1. The samples are individually characterized by magnetization experiments, which are also discussed briefly.

Magnetic characterization

Fig. 4.24 shows $M(T)$ in ZFC, FH, and FC states for the samples prepared for neutron diffraction studies. M_s, A_s and T_C^A are indicated by vertical arrows and are listed in Table 4.2 for each alloy. All alloys are in the ferromagnetic austenitic state at room temperature and in the martensitic state at 5 K. Below T_C^A, all samples order ferromagnetically. A splitting between FC and FH magnetization data occurs just below T_C^A for $Ni_{50}Mn_{27}Ga_{23}$ (Fig. 4.24(a)). The ferromagnetism extends down to M_s, and then the magnetization decreases rapidly for all samples. The martensitic state is also FM but a Curie temperature cannot be attributed for this composition.

Sample	M_s(K)	M_f(K)	A_s(K)	A_f(K)	T_C^A(K)
$Ni_{50}Mn_{27}Ga_{23}$	284	249	255	290	375
$Ni_{50}Mn_{35}Sn_{15}$	215	156	113	213	320
$Ni_{50}Mn_{34}In_{16}$	195	135	160	205	305

Table 4.2: Martensitic transformation temperatures M_s, M_f, A_s, and A_f and the austenite Curie temperature T_C^A obtained from $M(T)$ for the samples used in neutron diffraction studies.
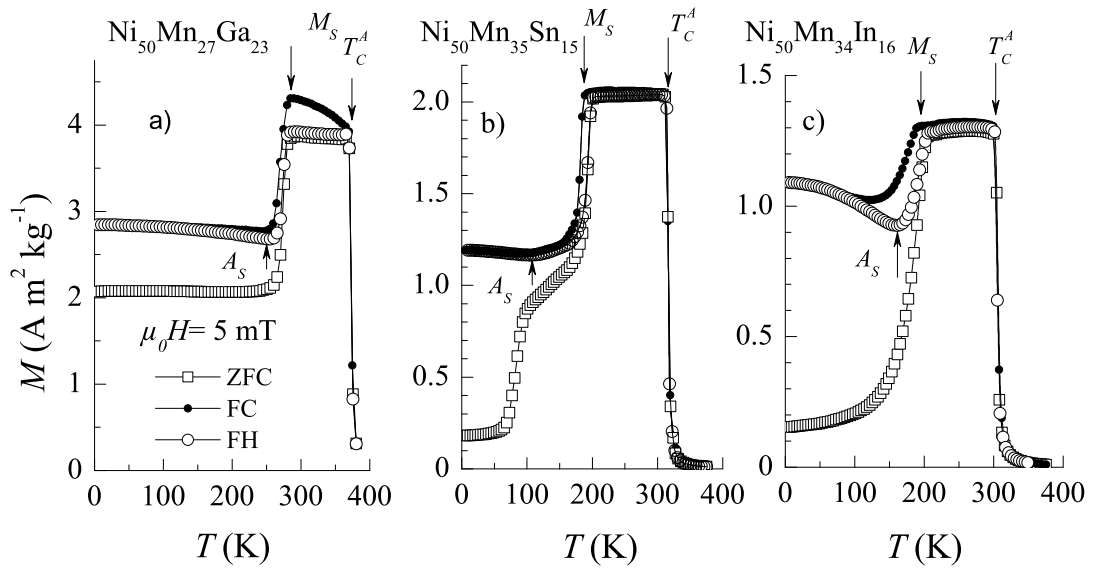
Figure 4.24: ZFC, FC, and FH-$M(T)$ in 5 mT of (a) $Ni_{50}Mn_{27}Ga_{23}$, (b) $Ni_{50}Mn_{35}Sn_{15}$, and (c) $Ni_{50}Mn_{34}In_{16}$. Vertical arrows indicate M_s, A_s, and T_C^A.

$\mathbf{Ni_{50}Mn_{37}Ga_{23}}$

The diffraction patterns of $Ni_{50}Mn_{27}Ga_{23}$ at 300 K are shown in Fig. 4.25(a). The crystal structure of the austenitic state is cubic, $L2_1$ with the space group $Fm\bar{3}m$. A lattice parameter of the austenite $a_{austenite} = 5.8348$ Å is calculated by profile matching using Fullprof program. The diffraction pattern at 300 K under 5 T in Fig. 4.25(b) shows the same cubic structure. However, some intensities which are related to the martensite structure indicate a second phase. The lattice parameters of the second orthorhombic phase are $a = 17.1159$ Å, $b = 9.9570$ Å, $c = 3.6580$ Å with the space group $Pnnm$.

The profile matching results for the spectrum at 5 K (Fig. 4.26(a)) show the presence of an orthorhombic crystal structure with space group $Pnnm$, and lattice parameters $b = 7a$ which is related to the 7-fold modulated martensitic structure (or 7M modulated) [92,93]. Fig. 4.26(b) shows the diffraction patterns at 5 K in the range of $20° \leq 2\theta \leq 40°$ in the absence of field (black line) and under 5 T cooling-field (red line). The crystal structures for both conditions are orthorhombic with 7-fold modulation. The lattice parameters are collected in Table 4.3 together with the reliability factor χ^2.

μ_0H (T)	a(Å)	b(Å)	c(Å)	χ^2
		300 K		
0	5.8348	5.8348	5.8348	4.7
5	5.8383	5.8383	5.8383	8.9
		5 K		
0	4.2269	29.3727	5.5426	6.2
5	4.2265	29.3579	5.5357	6.7

Table 4.3: Lattice parameters of $Ni_{50}Mn_{27}Ga_{23}$ at 300 K and 5 K in the absence of a cooling-field and in the presence of a 5 T cooling-field. χ^2 gives the profile matching parameter which is related to the quality of the calculated diffraction pattern.
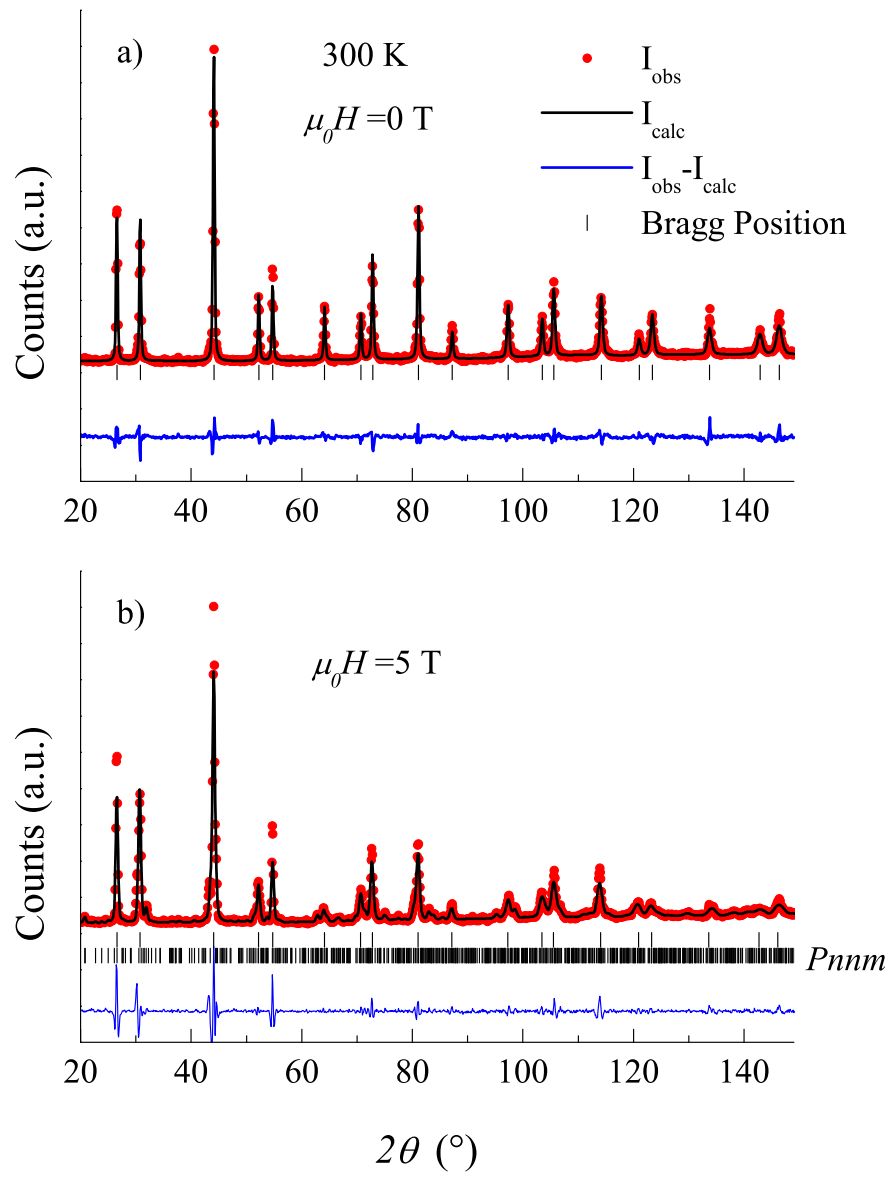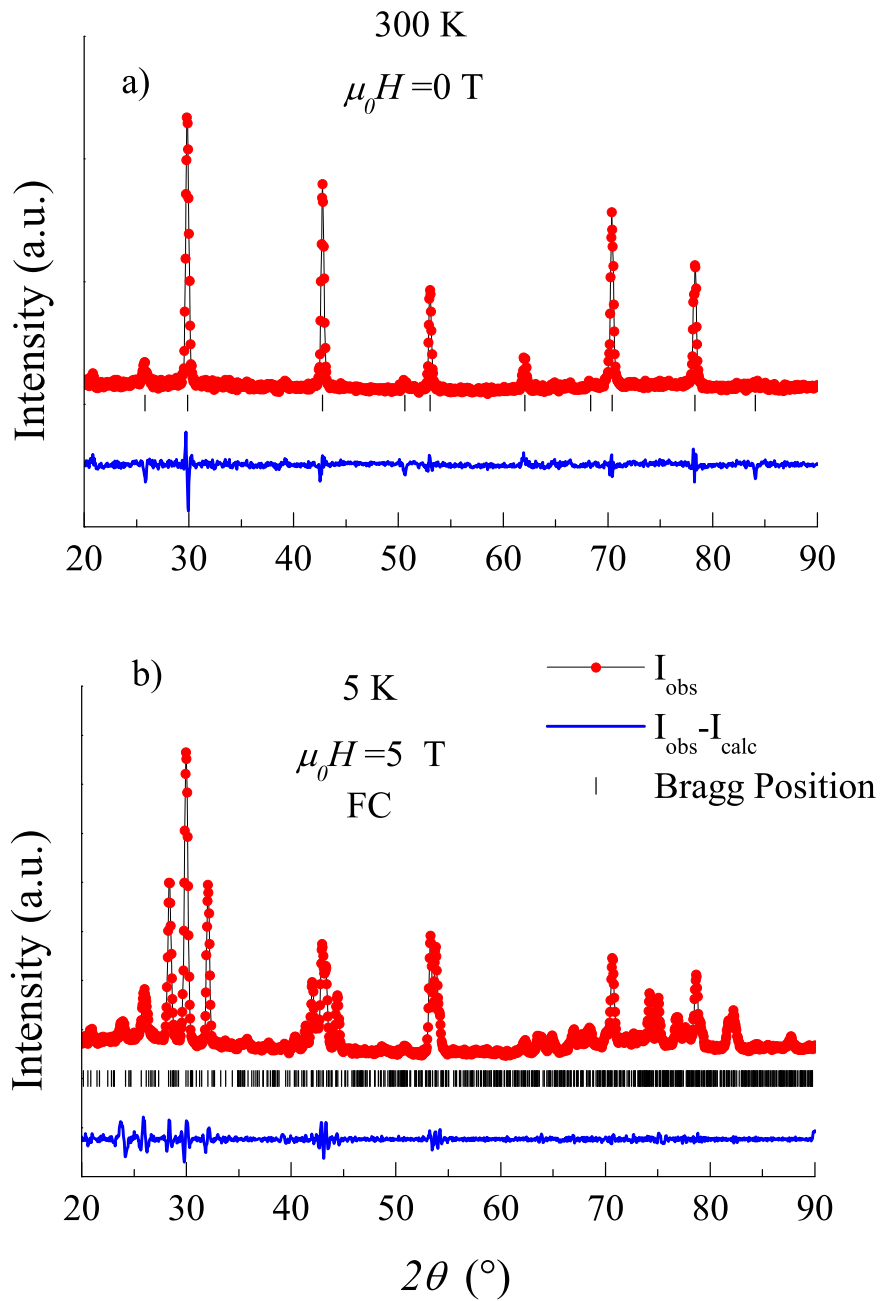
Figure 4.25: Neutron diffraction patterns at 300 K (a) in zero-field and (b) in 5 T for Ni$_{50}$Mn$_{27}$Ga$_{23}$ together with calculated patterns and the Bragg positions. In (b), the Bragg positions of the second orthorhombic phase *Pnnm* is also shown.
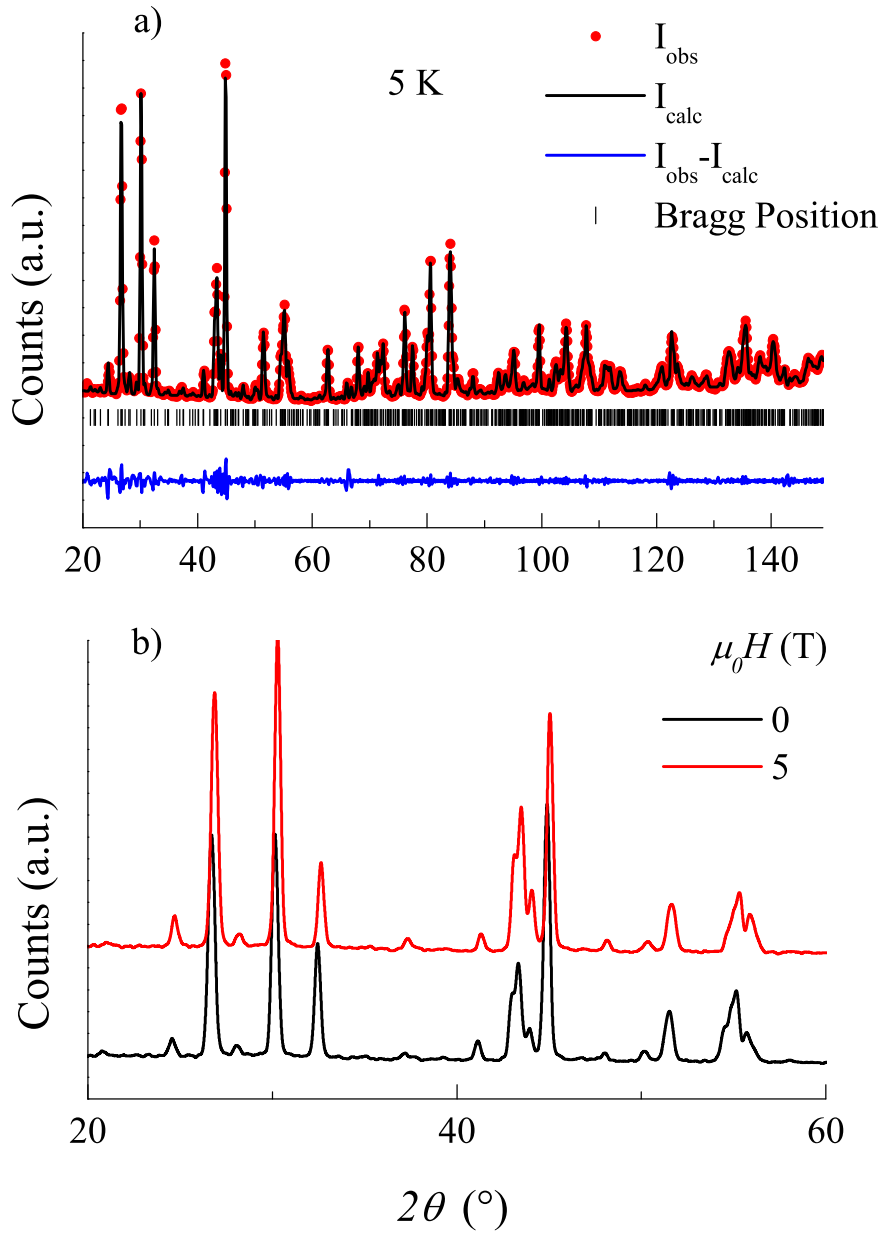
Figure 4.26: Neutron diffraction patterns (a) at 5 K in zero-field and (b) comparison of the 5 K-data under zero field and 5 T magnetic field for $Ni_{50}Mn_{27}Ga_{23}$. The crystal structure is orthorhombic with space group *Pnnm*.

Ni$_{50}$Mn$_{35}$Sn$_{15}$

The diffraction patterns for Ni$_{50}$Mn$_{35}$Sn$_{15}$ in Figs. 4.27(a) and (b) are related to a cubic crystal structure at 300 K with a space group $Fm\bar{3}m$ and an orthorhombic structure at 5 K with a space group $Pmma$. By applying a 5 T field at 300 K, the crystal structure remains the same with slightly increased lattice parameter. The results of the profile matching agree well with those obtained by Rietvelt analysis for Ni$_{50}$Mn$_{36}$Sn$_{14}$ [88]. The inset of Fig. 4.27(b) gives a comparison between 0 T and 5 T diffraction patterns at 5 K. The crystal structure is the same for both cases. The lattice parameters are collected in Table 4.4 for the martensitic and the austenitic states.

μ_0H (T)	a(Å)	b(Å)	c(Å)	χ^2
		300 K		
0	5.9946	5.9946	5.9946	4.2
5	5.9959	5.9959	5.9959	4.2
		5 K		
0	8.6023	5.6529	4.3616	7.6
5	8.6106	5.6523	4.3656	7.2

Table 4.4: Lattice parameters of Ni$_{50}$Mn$_{35}$Sn$_{15}$ at 300 K and 5 K in the absence of a magnetic field and in the presence of a 5 T cooling-field. χ^2 is the profile matching parameter which is related to the quality of the calculated diffraction pattern.
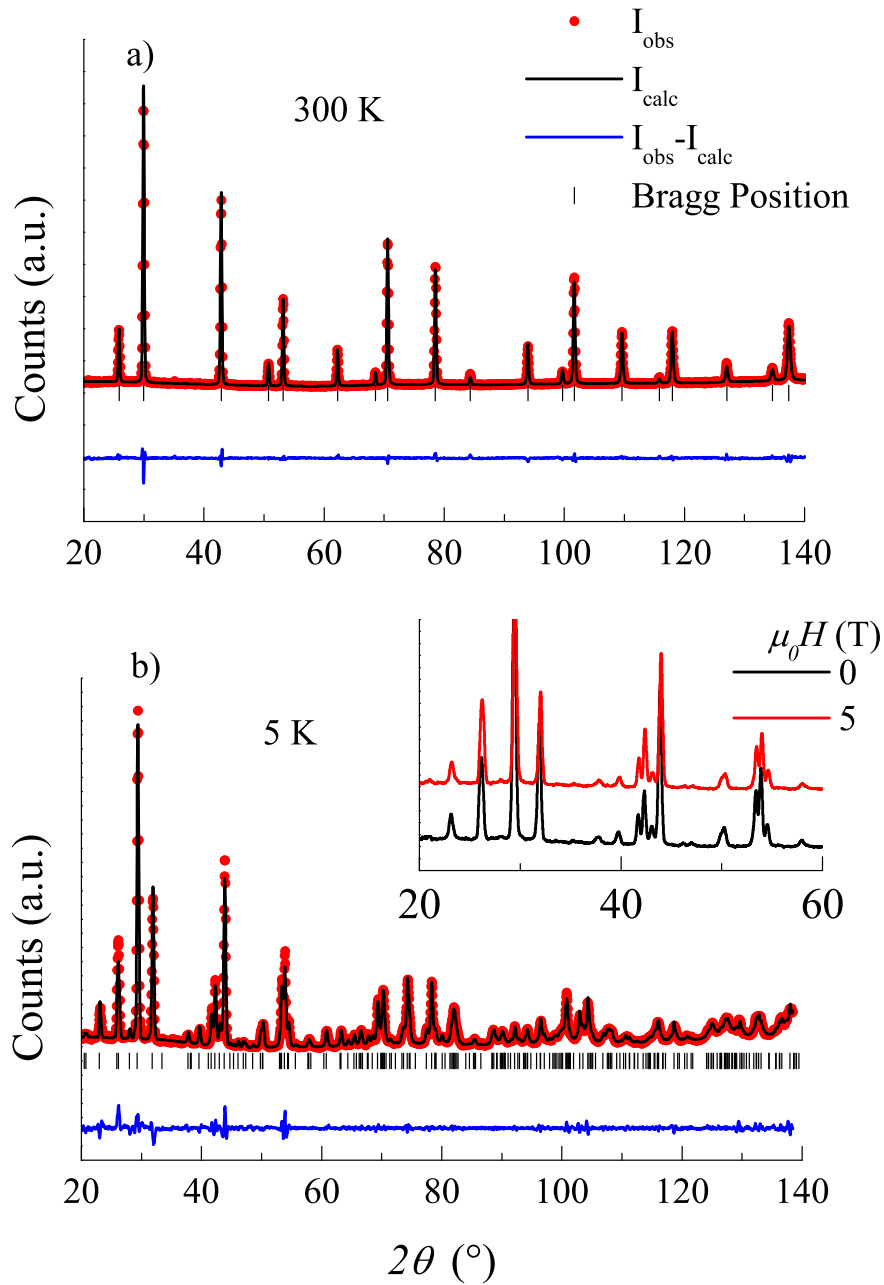
Figure 4.27: Neutron diffraction pattern at (a) 300 K and (b) 5 K for $Ni_{50}Mn_{35}Sn_{15}$ together with the calculated patterns and the Bragg positions of the crystal structure. Inset shows comparison of the observed patterns under an applied 5 T-magnetic field and zero-field at 5 K. The crystal structures are cubic $L2_1$ at 300 K and orthorhombic with space group *Pmma* at 5 K.

Ni$_{50}$Mn$_{34}$In$_{16}$

The diffraction pattern of Ni$_{50}$Mn$_{34}$In$_{16}$ at 300 K in Fig. 4.28(a) is related to a cubic L2$_1$ structure with space group $Fm\bar{3}m$, and a lattice parameter $a = 6.0013$ Å (Table 4.5). Under a 5 T magnetic field at 300 K, the crystal structure is the same as in the zero-field pattern. The martensitic crystal structure at 5 K under 5 T cooling-field is orthorhombic with a space group $P2_12_12_1$ shown in Fig. 4.28(b). The relations that appear on the lattice parameters in Ni$_{50}$Mn$_{34}$In$_{16}$ alloys are $a_{martensite} \approx 3a_{austenite}$ and $c \approx \sqrt{2}a_{austenite}$.

The patterns obtained at 5 K in the absence of a magnetic field and under a 5 T cooling-field are compared in two ranges in Fig. 4.29: (a) $20° \leq 2\theta \leq 90°$ and (b) $90° \leq 2\theta \leq 140°$. The red pattern, which is obtained under a 5 T cooling-field is related to a mixture of the orthorhombic martensite phase and the cubic austenite phase. The reflections associated with the cubic phase can be better distinguished in the higher range in Fig. 4.29(b). The Miller indices (hkl) of the austenite phase are given on the pattern.

μ_0H (T)	a(Å)	b(Å)	c(Å)	χ^2
		300 K		
0	6.0013	6.0013	6.0013	3.5
5	5.9986	5.9986	5.9986	2.8
		5 K		
0	17.3287	9.4975	10.8435	1.3
5	17.8033	9.7913	8.9430	1.7
5	5.9022	5.9022	5.9022	1.7

Table 4.5: Lattice parameters of Ni$_{50}$Mn$_{34}$In$_{16}$ at 300 K and 5 K in the absent of a magnetic field and in the presence of a 5 T cooling-field. χ^2 show the profile matching parameter which is related to the quality of the calculated diffraction pattern.

Figure 4.28: Neutron diffraction patterns at (a) 300 K at zero-field and (b) 5 K at 5 T field cooled for $Ni_{50}Mn_{34}In_{16}$ sample together with calculated pattern and the Bragg positions of the crystal structure.
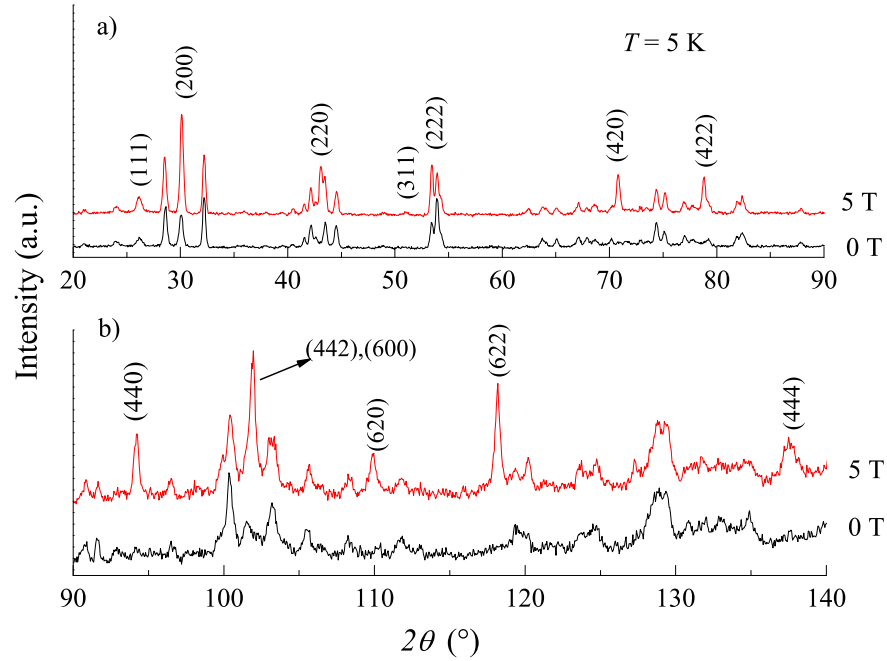
Figure 4.29: Neutron diffraction patterns in zero-field and 5 T applied field at 5 K for $Ni_{50}Mn_{34}In_{16}$ sample for (a) $20° \leq 2\theta \leq 90°$ and (b) $90° \leq 2\theta \leq 140°$. The Bragg reflections which belonging to the $L2_1$ cubic structure are indicated in the 5 T-pattern.

Previous studies on $Ni_{50}Mn_{34}In_{16}$ have shown that in the presence of a cooling-field greater than 4 T, the martensitic transformation from austenite to martensite is kinetically arrested, and this effect depends on the thermal magnetic history of the sample [62,94]. The coexistence of the martensite structure with the austenite structure at 5 K displays the arrested austenite phase in $Ni_{50}Mn_{34}In_{16}$ which is not found in $Ni_{50}Mn_{27}Ga_{23}$ and $Ni_{50}Mn_{35}Sn_{15}$.

To calculate the amount of rest-austenite phase in the martensitic state for $Ni_{50}Mn_{34}In_{16}$, we make use of the neutron diffraction patterns taken at 300 K and 5 K in 5 T cooling-field. In Fig 4.30, the vertically shifted patterns at 5 K (red) and 300 K (black) in 5 T cooling-field are shown in the neighborhood of the cubic (220) reflection in the range $35° \leq 2\theta \leq 50°$. The blue pattern is related to pure martensite obtained at 5 K in the absence of magnetic field. In the red pattern, the intensity resulting from the mixed austenite phase is located at about 43°. If we assume that the total intensity of the (220) reflection under 5 T at 300 K and 5 K remains the same, the amount of the rest-austenite phase can be estimated from the ratio I_M/I_A where I_A and I_M are the total intensities in the austenite and martensite phases. Approximately
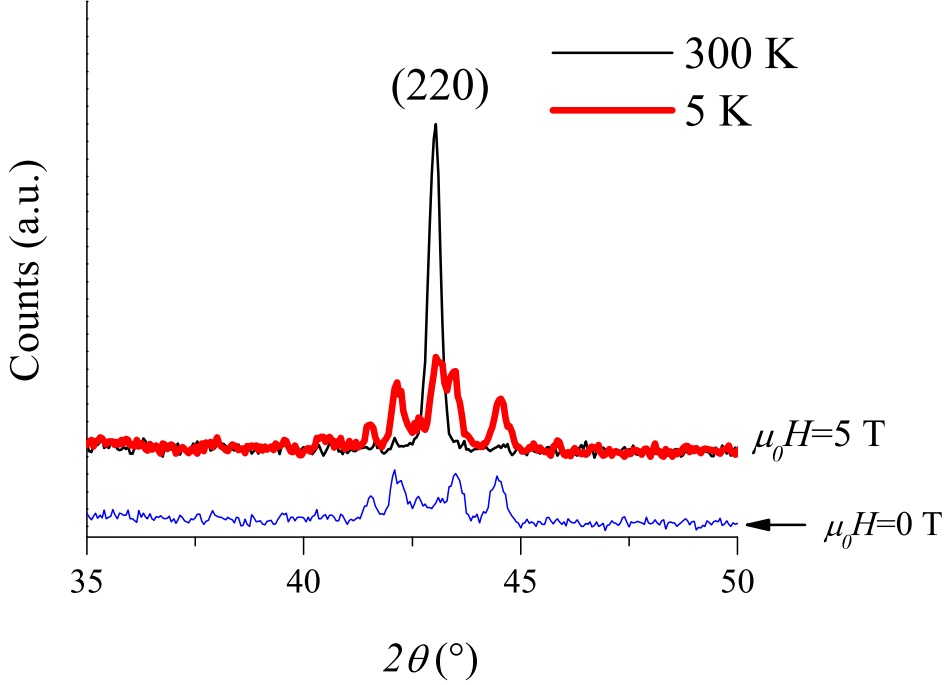
Figure 4.30: Neutron diffraction patterns around the (220) L2$_1$-cubic reflection in Ni$_{50}$Mn$_{34}$In$_{16}$. The black and red data are taken at 300 K and 5 K under a 5 T cooling-field. The vertically shifted blue data belong to the martensite phase at 5 K in ZFC state.

45% rest-austenite is found in Ni$_{50}$Mn$_{34}$In$_{16}$ at 5 K. On the basis of this estimation, we can better understand the temperature dependence of the strain under a cooling-field for this alloy. In Fig. 4.31, $\Delta l/l(T)$ is shown in the absence of a cooling-field and under a 5 T cooling-field. The extrapolated red dotted line represents $\Delta l/l(T)$ in the absence of the martensitic transformation. At point 1, $\Delta\varepsilon = 0$. Point 2 and point 3 represent strain-values in the pure martensite phase and in the mixed austenite/martensite phase, respectively. The "mixed" nature is verified by the results of neutron diffraction studies discussed above. The value of $\Delta\varepsilon^{H=0} = 0.19$ decreases under a 5 T cooling-field to $\Delta\varepsilon^{H=5T} = 0.11$. When a strain value arising from 45% austenite is substracted from the strain-value of the mixed phase, the strain decreases to point 4 as indicated by the arrow. This leads to an estimated increase in $\Delta\varepsilon^{H=5T}$ from 0.11 to 0.17. According to the discussion in 4.2.1, this would further confirm that the easy-direction of the magnetization is along the long-axis in Ni$_{50}$Mn$_{34}$In$_{16}$ even when the effect of austenite arrest is taken into account.
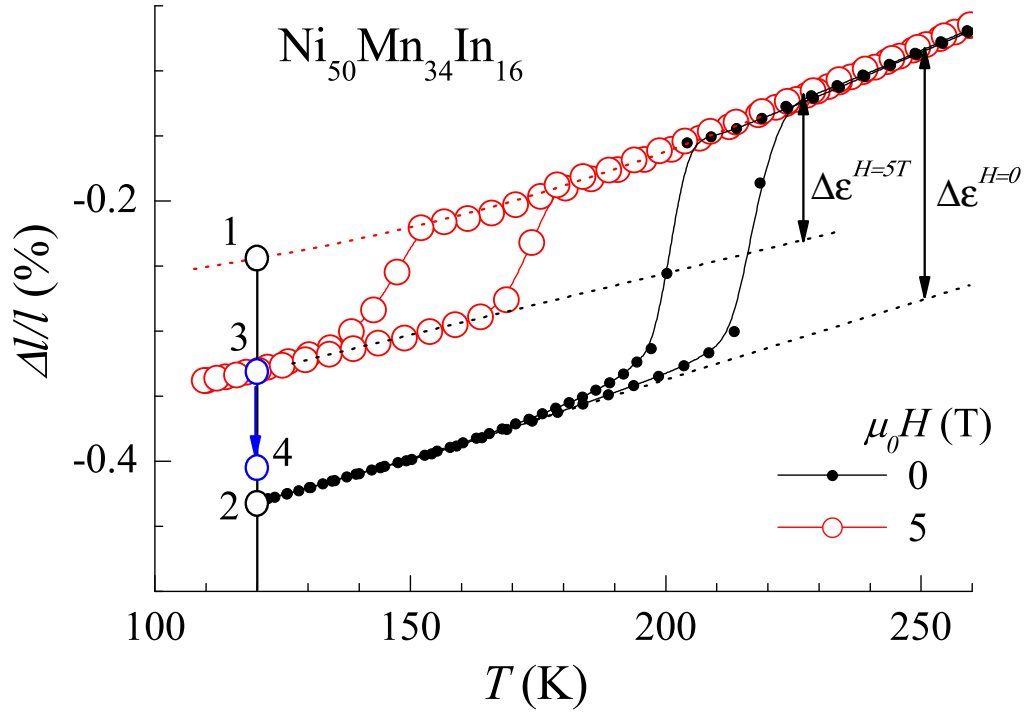
Figure 4.31: $\Delta l/l(T)$ in the absence of cooling-field and under a 5 T cooling-field in Ni$_{50}$Mn$_{34}$In$_{16}$. $\Delta\varepsilon$ indicates the strain difference between the austenitic and martensitic states.

When we consider that the shift of 10 KT^{-1} in M_s to lower temperatures under a cooling-field results from austenite arrest, one can expect that at higher magnetic cooling-fields, the martensitic transformation can be completely suppressed. In fact, in single crystalline Ni$_{50}$Mn$_{34}$In$_{16}$, the shift of the martensitic transformation has been reported to be 12 KT^{-1}, and the resistivity around M_s decreases under an external magnetic field with respect to the zero-field resistivity as a result of remaining rest-austenite under an applied cooling-field [10]. Studies on NiCoMnIn have also shown that an external magnetic field up to 8 T stabilizes the austenite phase completely [89].

The quaternary compounds of Ni$_{50}$Mn$_{34}$In$_{16}$ exhibit the similar relative length-change properties under a cooling-field which can be associated with the alignment of easy magnetization along the long-axis in these alloys. In Ga and Sn-substituted alloys, austenite arrest can be expected as well. However, in Ni$_{50}$Mn$_{36}$Sn$_{14}$ the shift of M_s has been reported to be around 2 KT^{-1} indicating that fields higher than 5 T are required for austenite arrest to occur [11].

4.3   Nature of Magnetism Around the Martensitic Transformation

Ni-Mn-based Heusler alloys undergo martensitic transformations in certain compositional ranges, and all such systems show a drop at M_s in $M(T)$ in small magnetic fields of about 10 mT or less [6,86]. The drop persists in higher measuring fields of about 5 T except in Ni-Mn-Ga alloys. In these alloys, the slope in $M(T)$ reverses sign around M_s above a certain measurement field [95]. The cause of the drop in $M(T)$ in Ni-Mn-based Heusler alloys is often thought to be related to the development of local AF ordering associated with changing distance of the Mn-Mn bonding [88].

To understand the cause of magnetic-field-induced effects in magnetic shape memory alloys, it is necessary to understand the nature of the magnetic ordering, particularly in the temperature-vicinity of the martensitic transformation. The following section presents results of neutron polarization analysis in $Ni_{50}Mn_{40}Sb_{10}$ and $Ni_{50}Mn_{37}Sn_{13}$ and the result of FMR studies in $Ni_{50}Mn_{34}In_{16}$ and $Ni_{50}Mn_{37}Sn_{13}$. These techniques are particularly useful for studying the nature of magnetic interactions.

4.3.1   Polarized neutron scattering

We study the nature of the magnetic interactions in the martensitic and austenitic states of Ni-Mn-based Heusler systems. In this section, we discuss the results of neutron polarization analysis experiments on $Ni_{50}Mn_{40}Sb_{10}$ and $Ni_{50}Mn_{37}Sn_{13}$ prototype systems. First, the magnetic characterization of these two samples is given briefly.

Magnetic characterization of the samples

The results of calorimetric measurements for $Ni_{50}Mn_{40}Sb_{10}$ given in Fig. 4.32 show that the structural transformation takes place at $M_s = 440$ K. The double peak structure observed in the heating and cooling curves suggests the presence of inter-martensitic transitions. The hysteresis width $\Delta T \approx 12$ K corresponds to the difference in the position of the shoulders or peaks in the heating and cooling curves.

Fig. 4.33 shows $M(T)$ in ZFC, FC and FH states, and the temperature-dependent flipping ratio $R_F(T)$ for both samples. In Fig. 4.33(a), FM ordering is not found in the austenitic state so that M_s cannot be resolved. The value of M_s determined from calorimetric measurements indicates that the martensitic transformation occurs
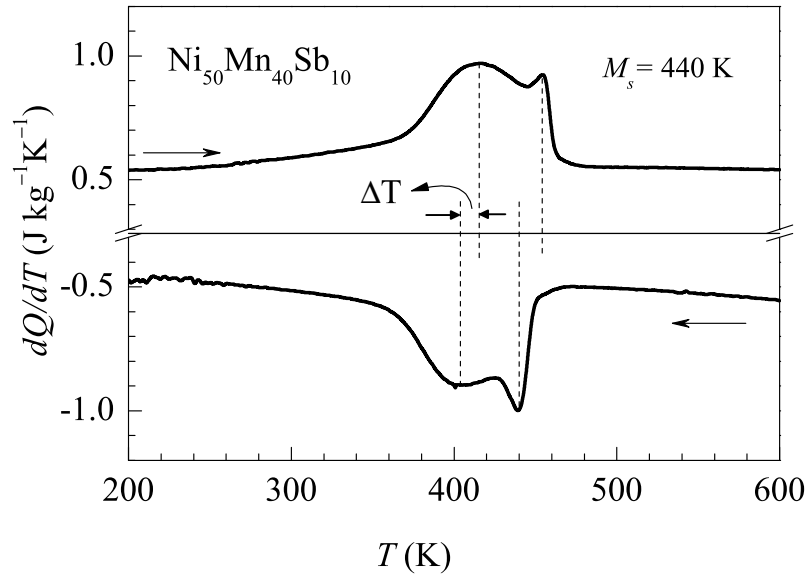
Figure 4.32: dQ/dT versus temperature for $Ni_{50}Mn_{40}Sb_{10}$ undergoing martensitic transformations. Horizontal arrows indicate the direction of temperature change. The width of the hysteresis ΔT shows the difference in temperature corresponding to the shoulder maxima on cooling and heating.
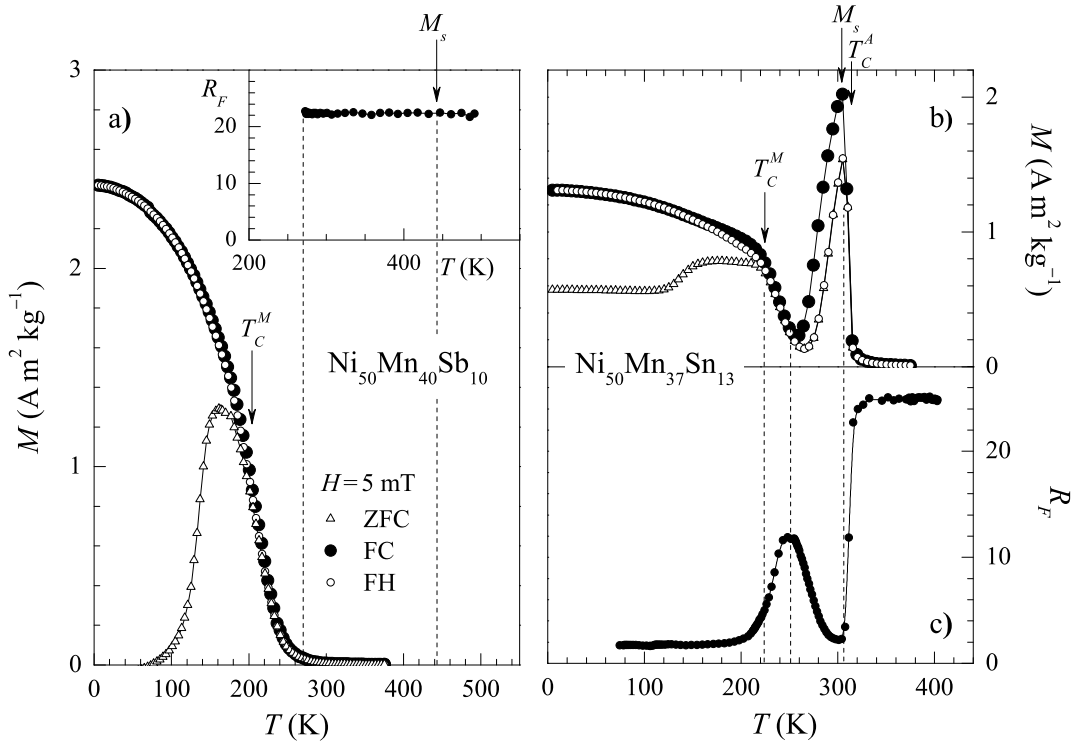
Figure 4.33: Characterization of the samples for the polarization analysis experiments of $Ni_{50}Mn_{40}Sb_{10}$ and $Ni_{50}Mn_{37}Sn_{13}$. (a) $M(T)$ in the ZFC, FC, and FH states for $Ni_{50}Mn_{40}Sb_{10}$. The inset shows $R_F(T)$ for $Ni_{50}Mn_{40}Sb_{10}$. (b) $M(T)$ in the ZFC, FC, and FH states and (c) $R_F(T)$ for $Ni_{50}Mn_{37}Sn_{13}$.

from a paramagnetic (PM) austenitic to a PM martensitic state in $Ni_{50}Mn_{40}Sb_{10}$. It orders ferromagnetically in the martensitic state at $T_C^M \approx 210$ K, where ZFC and FC curves split. In the inset of Fig. 4.33(a), the neutron depolarization measurement shows $R_F \approx 25$ and remains temperature-independent from the highest temperatures down to temperatures approaching T_C^M. This means that the net magnetization of $Ni_{50}Mn_{40}Sb_{10}$ is zero, and neutrons are not depolarized by the sample.

$Ni_{50}Mn_{37}Sn_{13}$ orders ferromagnetically in the austenitic state at $T_C^A = 310$ K as seen in Fig. 4.33(b). Just below T_C^A, the alloy undergoes a martensitic transformation at $M_s \approx 305$ K, and the magnetization rapidly drops below M_s. At $T_C^M \approx 220$ K, $Ni_{50}Mn_{37}Sn_{13}$ orders ferromagnetically again. $R_F(T)$ for this alloy is shown in Fig. 4.33(c). Above T_C^A, where the alloy is in the PM state, $R_F \approx 25$. The initial sharp drop with decreasing temperature in $R_F(T)$ is related to the beginning of FM order below T_C^A, whereby the neutrons are depolarized by the FM domains in the alloy. On the other hand, R_F begins to recover and increases just below M_s with decreasing temperature. This points out that the amount of FM austenite progressively decreases at $T < M_s$. Then, R_F passes through a maximum with $R_F \approx 12$ at a temperature corresponding to the local minimum in $M(T)$ at 250 K. However, R_F does not regain its maximum value of 25 as some FM rest-austenite remains below M_s. As the temperature further decreases, $R_F(T)$ decreases as well. The decrease progresses from 250 K to 200 K in a relatively broad temperature-range with respect to the decrease around T_C^A. This is an indication that the position of T_C^M is not well-defined. The broad nature of the FM transition in the martensitic state for $Ni_{50}Mn_{40}Sb_{10}$ and $Ni_{50}Mn_{37}Sn_{13}$ is also identified in $M(T)$ in Figs. 4.33(b) and 4.33(c). For a ferromagnet, $M(T)$ rises sharply to a value corresponding to the demagnetization limit at the Curie temperature when measured in a small external magnetic field such as 5 mT. Then, $M(T)$ continues relatively temperature-independent as the temperature decreases [6]. In the martensitic state, we see that this is not the case for $M(T)$ below T_C^M.

$M(H)$ for $Ni_{50}Mn_{40}Sb_{10}$ is shown in Fig. 4.34(a). At 350 K and 315 K, corresponding to temperatures within the martensitic state, $M(H)$ is linear, and only at temperatures $T < T_C^M$ is the sample FM. Substantial high-field susceptibility is also present indicating that non-ferromagnetic components are present at these temperatures.

$M(H)$ for $Ni_{50}Mn_{37}Sn_{13}$ is plotted in 4.34(b). At 330 K, the sample is PM, but the curvature suggests the presence of short-range FM correlations. At 300 K, the magnetization increases rapidly in lower magnetic fields showing ferromagnetism. However, the magnetization does not saturate. $M(H)$ decreases in overall as the temperature de-
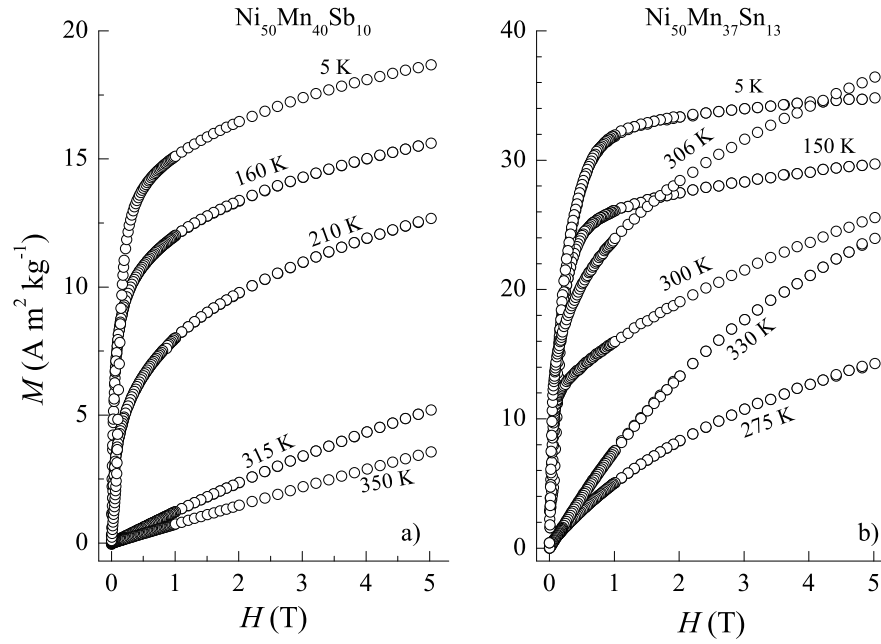
Figure 4.34: $M(H)$ plotted at selected temperatures for (a) $Ni_{50}Mn_{40}Sb_{10}$ and (b) $Ni_{50}Mn_{37}Sn_{13}$.

creases from 306 K to 275 K. In this temperature interval, the proportion of martensite increases with decreasing temperature, and along with it, the contribution of ferromagnetic exchange to the total magnetization from the austenite phase decreases. Below T_C^M the martensite phase becomes ferromagnetic; however, non-saturating properties of $M(H)$ suggest that non-FM entities persists for $T < 150$ K. At 5 K, $M(H)$ saturates above 5 T, and the saturation magnetization is smaller than that at 306 K.

Polarization analysis

The results of polarization analysis experiments on $Ni_{50}Mn_{40}Sb_{10}$ are shown in Fig. 4.35. $q-$dependent $(d\sigma/d\Omega)_{nuc}$ plotted in Fig. 4.35(a) shows diffraction patterns at 320 K and
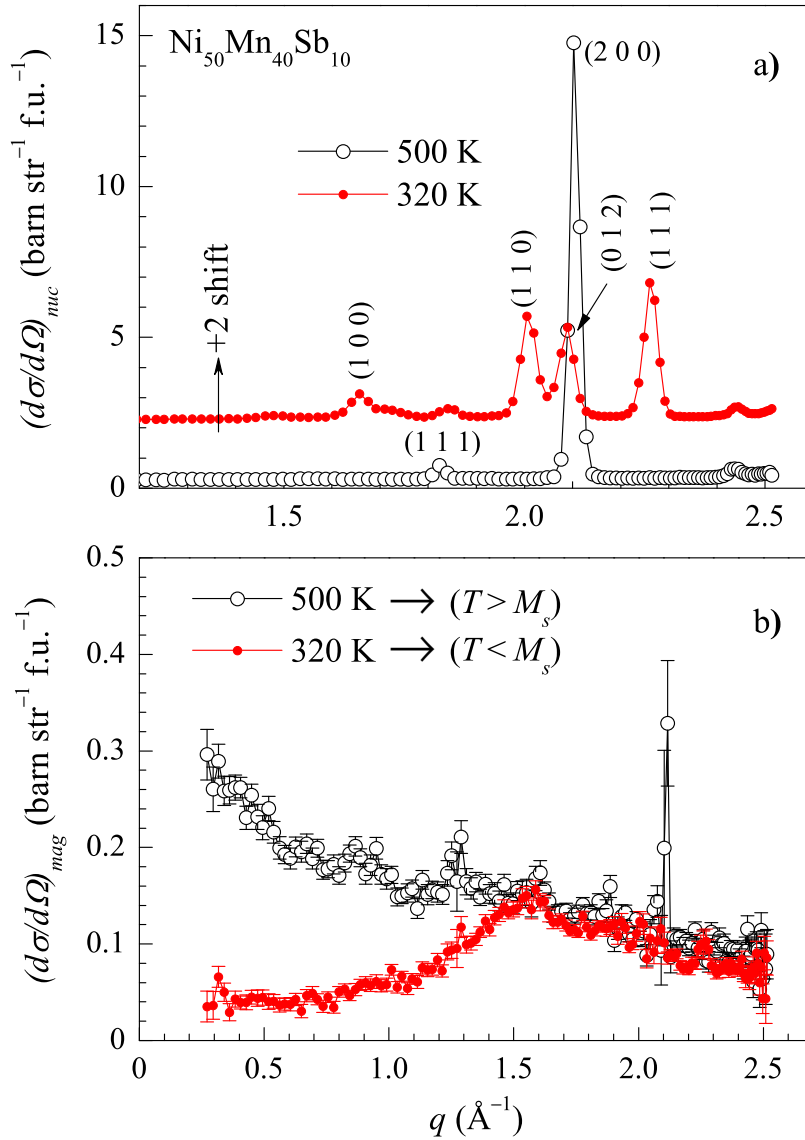
Figure 4.35: The q-dependence of the neutron scattering cross-sections in the austenitic (500 K) and martensitic (320 K) states of $Ni_{50}Mn_{40}Sb_{10}$ ($M_s = 440$ K). (a) The nuclear cross-section is plotted in the range $1.2 \leq q \leq 2.6$ Å^{-1}. Open circles: L2$_1$ (indexed horizontally); filled circles: 4O (indexed vertically). The data for 320 K are shifted vertically by +2 units for clarity. (b) The magnetic cross-section. The forward scattering, present in the austenitic state at 500 K, vanishes in the martensitic state (320 K).

500 K related to the martensitic and the austenitic structures, respectively. The data
for 320 K are shifted vertically by +2 units for clarity. The martensitic structure is
determined as 4O modulated orthorhombic with a *Pmma* space group, in agreement
with earlier studies [32]. $q-$dependent $(d\sigma/d\Omega)_{mag}$ is plotted in Fig. 4.35(b) at 500
K and 320 K. At low q-values, forward scattering is present at $T > M_s$ indicating
the presence of FM correlations. However, FM ordering is not found in the austenitic
state in $M(T)$. The narrow peak in the magnetic scattering at 500 K accompanied by
relatively large error bars at $q \approx 2.1$ Å^{-1} results probably from systematic errors due
to the difficulties in separating the nuclear and magnetic contributions of the scattering
at a position close to the strong (200) nuclear Bragg peak in Fig. 4.35(a). At 320 K,
within the martensitic state, the scattering at low q-values is very weak indicating that
FM correlations have practically vanished. However, strong and broad diffuse scattering
is observed above about 0.8 Å^{-1} up to the instrumental limit of 2.5 Å^{-1}. This broad
diffuse scattering is due to the presence of AF correlations.
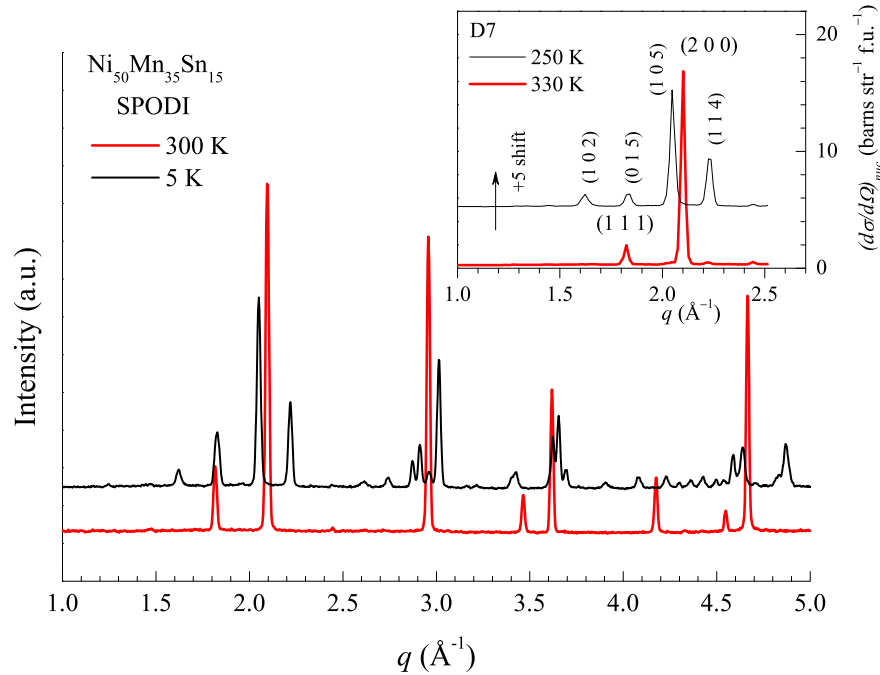
Figure 4.36: The q-dependence of the neutron diffraction spectrum of $Ni_{50}Mn_{35}Sn_{15}$-N
obtained on the SPODI spectrometer at 5 K (black line) and 300 K (red line). The inset shows
the nuclear cross-section in the austenitic (330 K) and martensitic (250 K) states obtained on
the D7 spectrometer for $Ni_{50}Mn_{37}Sn_{13}$. The data for 250 K are shifted vertically by +5 units
for clarity (austenite: indexed horizontally; martensite: indexed vertically).

The powder diffraction patterns in $Ni_{50}Mn_{35}Sn_{15}$ taken on the SPODI spectrometer at 5 K and 300 K are shown in Fig. 4.36 in the martensitic and austenitic states respectively. The reflections associated with the high symmetry austenitic cubic phase at 300 K split into a multitude of reflections at various zones in the low symmetry martensitic state at 5 K. The inset shows the q dependence of $(d\sigma/d\Omega)_{nuc}$ in the martensitic and austenitic states resulting from polarization analysis data taken on the D7 spectrometer. The data in the inset at 250 K are shifted vertically by +5 units for clarity. Data from SPODI and D7 spectrometers are in good agreement.

On the D7 spectrometer, the full XYZ-polarization analysis technique was employed at 500 K, whereas at 250 K, only Z-polarization was employed because of the lower value of $R_F \approx 12$ at this temperature, relative to the base flipping ratio of the instrument of $R_F \approx 25$. The analyzers are setup to count only non-spin-flip neutrons in the Z-direction on the D7 spectrometer. When the neutron-spin is rotated into the X-Y plane at low R_F, the presence of residual ferromagnetic austenite would give rise to uncertainties in the scattering information. However, R_F at 250 K is still sufficiently high to apply Z-
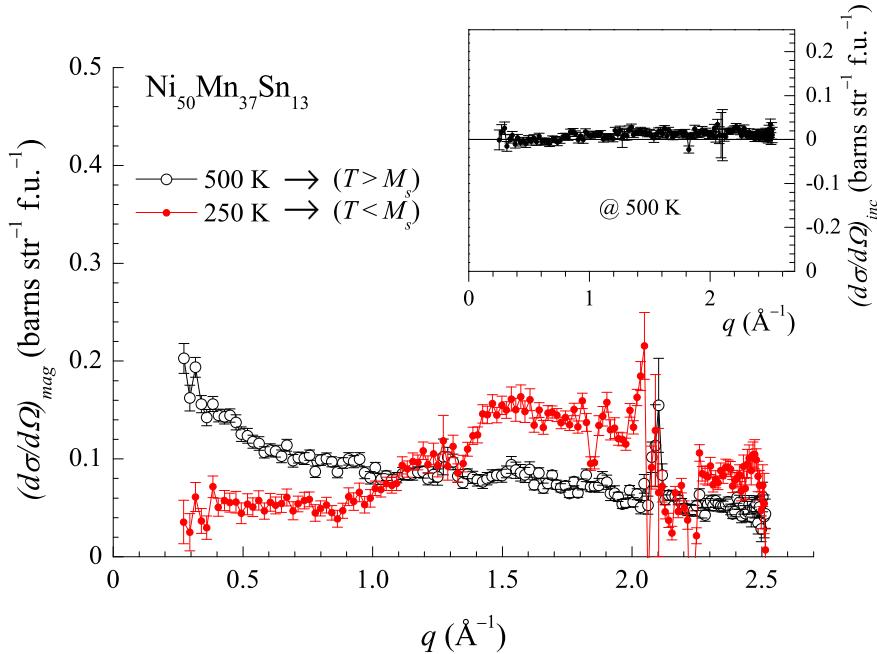
Figure 4.37: The q-dependence of the magnetic cross-section at 500 K and 250 K for $Ni_{50}Mn_{37}Sn_{13}$. The forward scattering, present in the austenitic state, essentially vanishes in the martensitic state ($M_s = 305$ K). The inset shows the q-dependence of spin incoherent cross-section at 500 K.

polarization analysis (Fig. 4.33(c)). For Z-polarization analysis at 250 K, $(d\sigma/d\Omega)_{inc}$ is assumed to be temperature-independent, and $(d\sigma/d\Omega)_{mag}$ is calculated using $(d\sigma/d\Omega)_{inc}$ at 500 K which was obtained using XYZ-polarization analysis [73].

q−dependent $(d\sigma/d\Omega)_{mag}$ for $Ni_{50}Mn_{37}Sn_{13}$ obtained at 250 K and 500 K is shown in Fig. 4.37. The magnetic scattering at 500 K is similar to that of $Ni_{50}Mn_{40}Sb_{10}$ for the same temperature (Fig. 4.35(b)). At this temperature, there is substantial forward scattering at low q values indicating the presence of FM correlations. $(d\sigma/d\Omega)_{inc}$ is shown in the inset of Fig. 4.37. The q-dependent $(d\sigma/d\Omega)_{mag}$ at 250 K is also similar to that of $Ni_{50}Mn_{40}Sb_{10}$ at 320 K. The FM correlations vanish and instead AF correlations are found at this temperature. The relatively large scattering in the data around $q = 2.1$ Å^{-1} (corresponding to the (200) Bragg position in the austenitic state and nearly the (105) Bragg position in the martensitic state) is related to the presence of FM rest-austenite that causes partial depolarization of the neutrons and leads to some difficulties
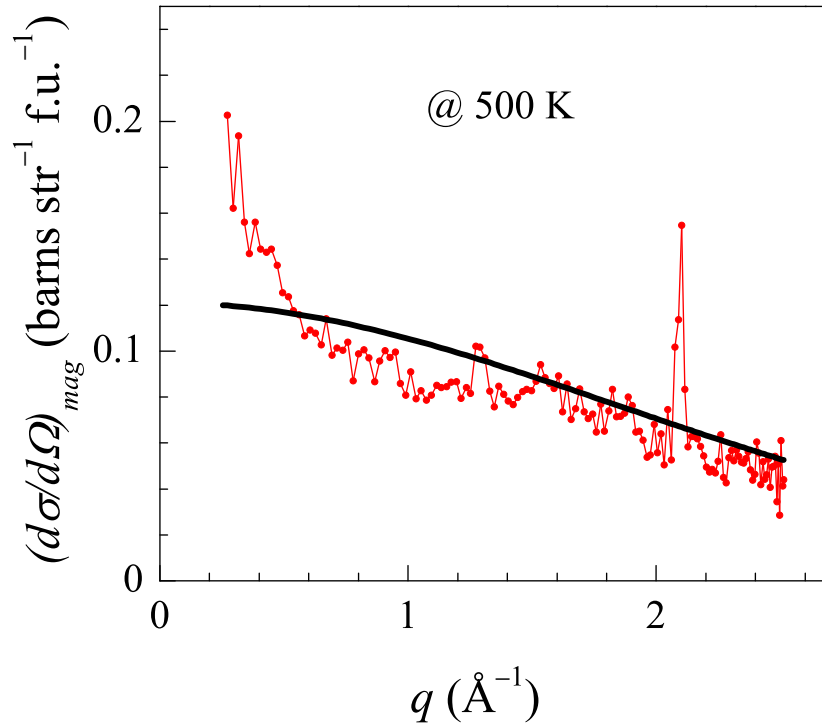
Figure 4.38: The comparison of the magnetic cross-section at 250 K and the q-dependence of the Mn form factor (heavy line) normalized to the value $(d\sigma/d\Omega)_{mag}$ at $q = 1.5$ Å^{-1} in $Ni_{50}Mn_{37}Sn_{13}$.

in separating nuclear and magnetic contributions.

Fig. 4.38 compares the q-dependence of the magnetic cross-section at 500 K to that of the single-ion Mn^{++} form factor normalized to the value of $(d\sigma/d\Omega)_{mag}$ at $q = 1.5$ Å^{-1}. The q-dependence of the form factor represents non-correlated behavior. The different behavior of the q-dependencies of the obtained data and that of the form factor, especially at low-q values, point out that the scattering at low-q is related to FM correlations.
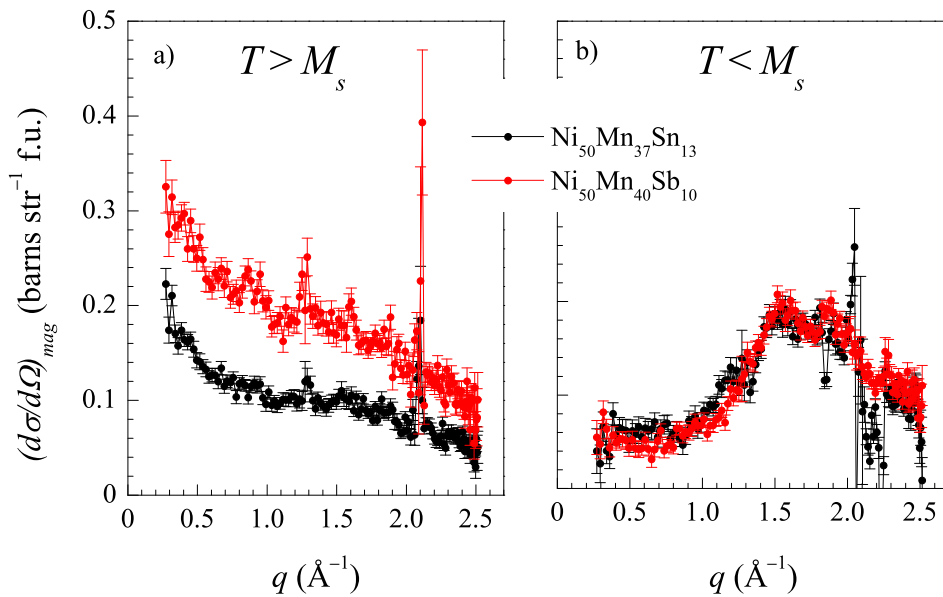
Figure 4.39: The q dependence of the magnetic cross-section at (a) $T > M_s$ and (b) $T < M_s$ for $Ni_{50}Mn_{37}Sn_{13}$ and $Ni_{50}Mn_{40}Sb_{10}$.

Figures 4.39(a) and (b) show the magnetic scattering as a function of q below and above M_s in $Ni_{50}Mn_{40}Sb_{10}$ and $Ni_{50}Mn_{37}Sn_{13}$, respectively. FM correlations are found at $T > M_s$, and persist well above T_C^A in both alloys, whereas the nature of AF short-range correlations are similar at $T < M_s$ for both alloys. For both $Ni_{50}Mn_{37}Sn_{13}$ and $Ni_{50}Mn_{40}Sb_{10}$, $(d\sigma/d\Omega)_{mag}$ for $T < M_s$ exhibits a broad shoulder beginning at about $q = 0.8$ Å^{-1} and extending up to the highest q-value of 2.5 Å^{-1} as seen in Fig. 4.39(b). The scattering profiles show a maximum nearly at the same value of about $q = 1.6$ Å^{-1}. This q-range includes the half-q positions of a multitude of Bragg-reflections appearing in the range of $1.5 < q < 5.0$ Å^{-1} as seen in Fig. 4.36. In an well ordered antiferromagnet, the magnetic scattering is observed as an intensity at the half position of the Bragg
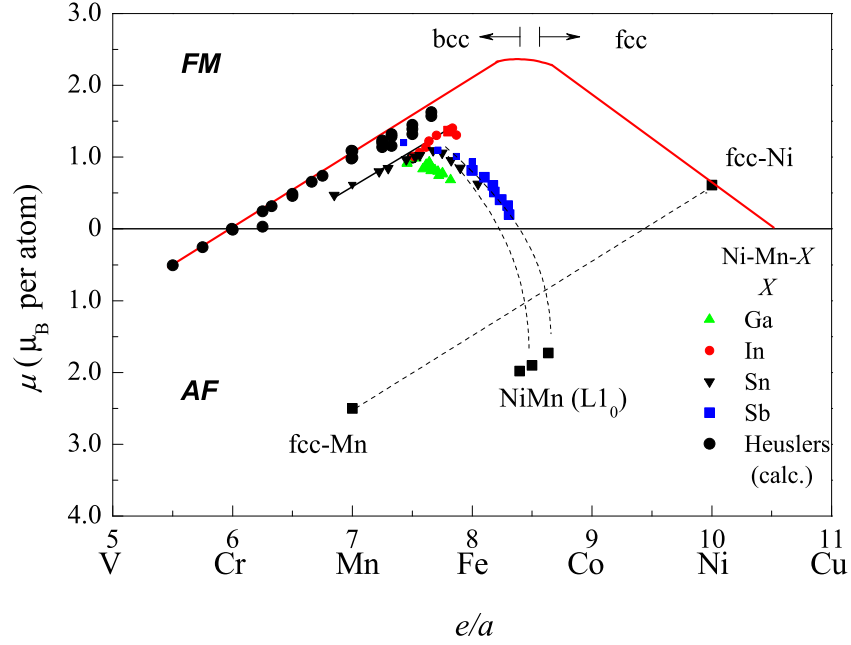
Figure 4.40: e/a dependence of the magnetic moment per atom in Heusler alloys. The decrease of magnetic moment μ in Ni-Mn-Sn- and Ni-Mn-Sb system by increasing e/a is caused by the presence of AF interactions.

intensities. Due to the doubled magnetic unit cell with respect to the crystallographic unit cell, AF correlations would be observed as weak, broad peaks centered at half-q positions of the various crystallographic zones. Such broad peaks can overlap and give rise to a broad shoulder in the magnetic scattering. Similar spectra exhibiting AF correlations have been previously observed in YMn_2 where diffuse scattering centered at half-Bragg positions develop into a single broad diffuse peak [96–98].

In NiMn-based Heusler alloys, because of the smaller cell-volume and therefore the smaller Mn-Mn separation in the modulated martensitic state with respect to the cubic austenitic state, FM exchange can be expected to weaken below M_s. Therefore, the drop in the $M(T)$ is caused by the loss of FM and the appearance of AF correlations in martensite phase.

For a general overview on the relationship between magnetic and electronic properties of Heusler alloys, we plot in Fig. 4.40 the magnetic moment μ of 3d FM and AF systems as a function of e/a. The red line represents the SlaterPauling (SP) curve for 3d FM materials. The bcc and fcc stability ranges for the FM systems are also shown. The

large black-filled circles represent calculated and experimental values of the moments of various stoichiometric Heusler and half-Heusler alloys [99,100], for which the structures are in principle bcc. μ increases with increasing e/a in the bcc range. The lower part of the curve is assigned to AF systems showing μ for fcc-Mn and the AF $Ni_{50}Mn_{50}$ alloy with $L1_0$ structure. AF-$Ni_{50}Mn_{50}$ is electronically intermediate between fcc-Mn and fcc-Ni, and the structure is close to being fcc, and one finds indeed that the magnetic moments of these alloys are accommodated approximately on the line joining the moments of fcc-Mn and fcc-Ni.

For Heusler alloys, μ can increase or decrease with increasing e/a. Off-stoichiometric Ni-Mn-based Heusler alloys show a decrease in μ-values that tend to the value of AF-$Ni_{50}Mn_{50}$. The decrease in μ with increasing e/a in the $L2_1$ phase can be understood to be caused by strengthening AF exchange. On the other hand, the sudden drop of magnetization below M_s and the broad feature of ferromagnetic ordering at T_C^M suggest the presence of non-ferromagnetic entities.

4.3.2 Ferromagnetic resonance

The limitations of the polarization analysis technique close and below to T_C^M, does not allow the nature of magnetic exchange to be determined at these temperatures. We have, therefore, employed the ferromagnetic resonance (FMR) technique to clarify this issue particularly in the temperature range below T_C^M.

The samples used in the FMR studies are first characterized by $M(T)$ measurements. $M(T)$ in an applied field of 5 mT for $Ni_{50}Mn_{35}In_{15}$ and $Ni_{50}Mn_{37}Sn_{13}$ are shown in Fig. 4.41(a) and (b), respectively. T_C^A, T_C^M, M_s, M_f, A_s and A_f are listed in Table 4.6. A_s and A_f are relevant to the discussion on FMR results and are also shown in Fig. 4.41. The alloys are FM above A_f and PM above T_C^A. A thermal hysteresis is observed between the FC and FH (and ZFC) data around the structural transition.
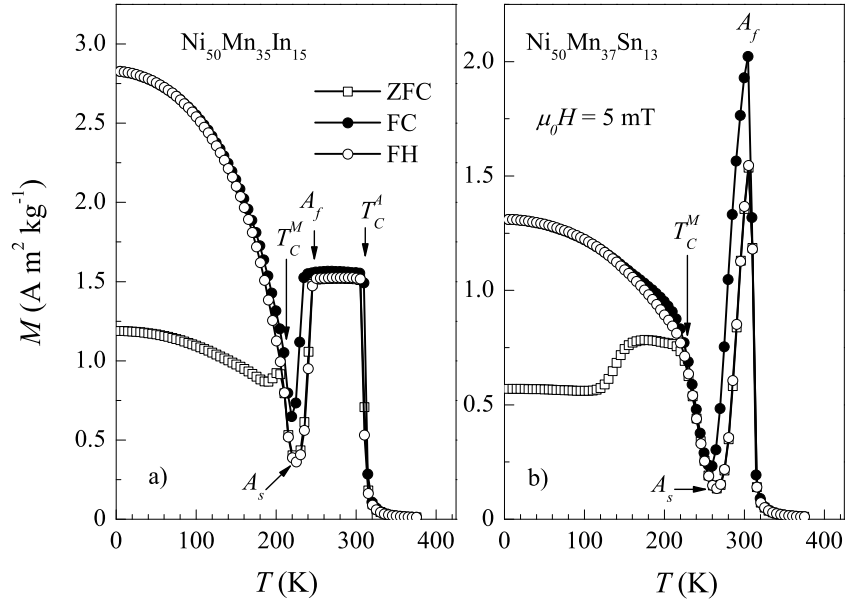
Figure 4.41: $M(T)$ in ZFC, FC and FH states under 5 mT of (a) $Ni_{50}Mn_{35}In_{15}$ and (b) $Ni_{50}Mn_{37}Sn_{13}$. T_C^A, A_f, A_s and T_C^M are indicated by arrows.

Fig. 4.42 shows the FMR spectra for both samples in their martensitic and austenitic states at 180 K and 300 K, respectively. There are three signals in the martensitic state in $Ni_{50}Mn_{35}In_{15}$ and $Ni_{50}Mn_{37}Sn_{13}$. These lines can originate from different domains in the sample or from three different magnetic sublattices. However, no angular dependence is observed, which would be expected for domains with different orientations of the

Alloy	T_C^A(K)	M_s(K)	M_f(K)	A_s(K)	A_f(K)	T_C^M(K)
$Ni_{50}Mn_{35}In_{15}$	310	250	219	220	260	205
$Ni_{50}Mn_{37}Sn_{13}$	310	305	255	265	305	230

Table 4.6:   The characteristic magnetic and structural transition temperatures of $Ni_{50}Mn_{35}In_{15}$ and $Ni_{50}Mn_{37}Sn_{13}$.

magnetization. At 180 K the signal at $\mu_0 H \leq 330$ mT (labeled as H_{res}^{III}) in $Ni_{50}Mn_{35}In_{15}$ is related to a FM component because it lies below the isotropic value. It is observed up to 300 K. The signals which are observed above ω/γ for both samples, labeled H_{res}^{II} and H_{res}^{I}, are related to non-FM components. The signal between $330 \leq \mu_0 H \leq 400$ mT in $Ni_{50}Mn_{35}In_{15}$ lies slightly above the isotropic value, so that it is also related to a non-FM component. The inset in Fig. 4.42 gives a comparison between the FMR spectra at 300 K where H_{res} lies below ω/γ in $Ni_{50}Mn_{37}Sn_{13}$ and $Ni_{50}Mn_{35}In_{15}$.
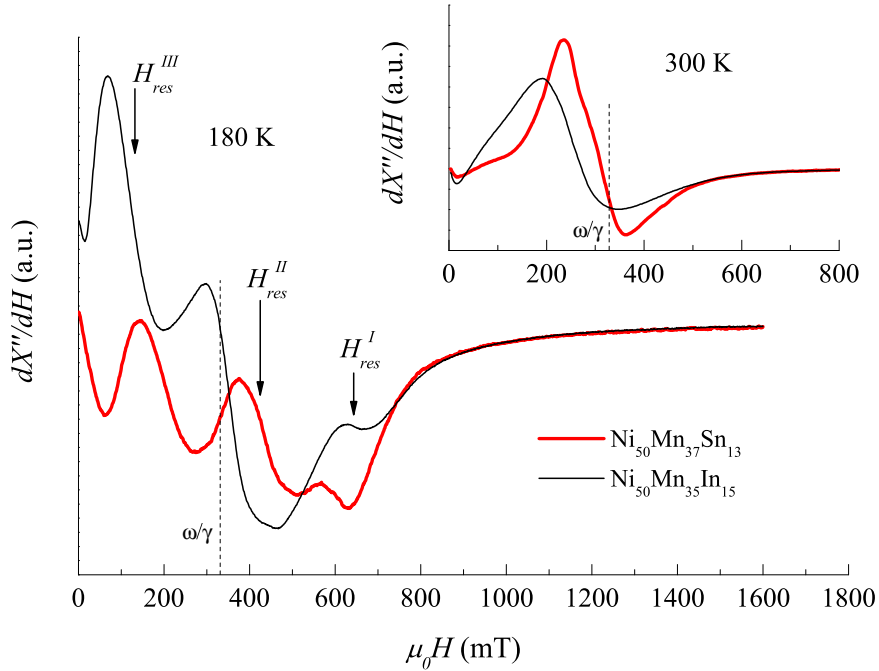
Figure 4.42: FMR measurements in the martensitic state at 180 K for $Ni_{50}Mn_{37}Sn_{13}$ and $Ni_{50}Mn_{35}In_{15}$. The H_{res}^{I}, H_{res}^{II} and H_{res}^{III} are shown by arrows. Inset shows the measurements in the martensitic state at 300 K.
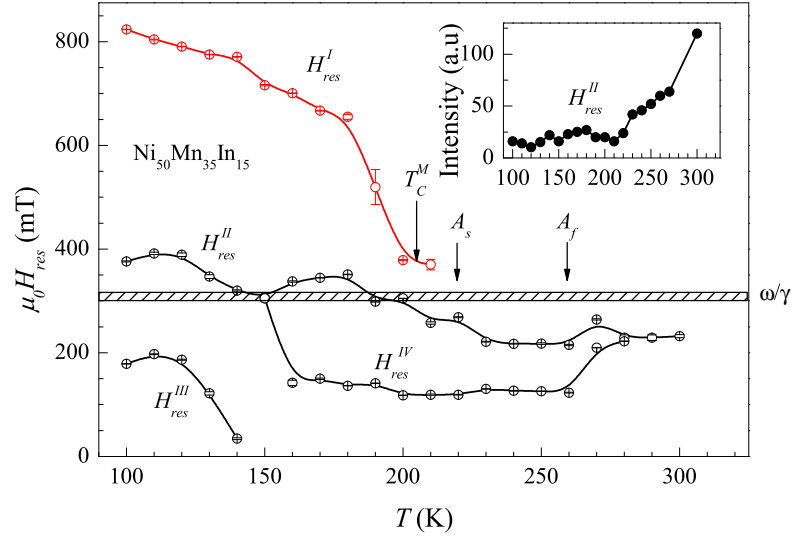
Figure 4.43: Temperature-dependence of the resonance field in $Ni_{50}Mn_{35}In_{15}$. Additional AF interactions appear below T_C^M. ω/γ indicates the isotropic value. Inset shows the temperature dependence of the intensity of the H_{res}^{II}. The errors are smaller than the symbol size.
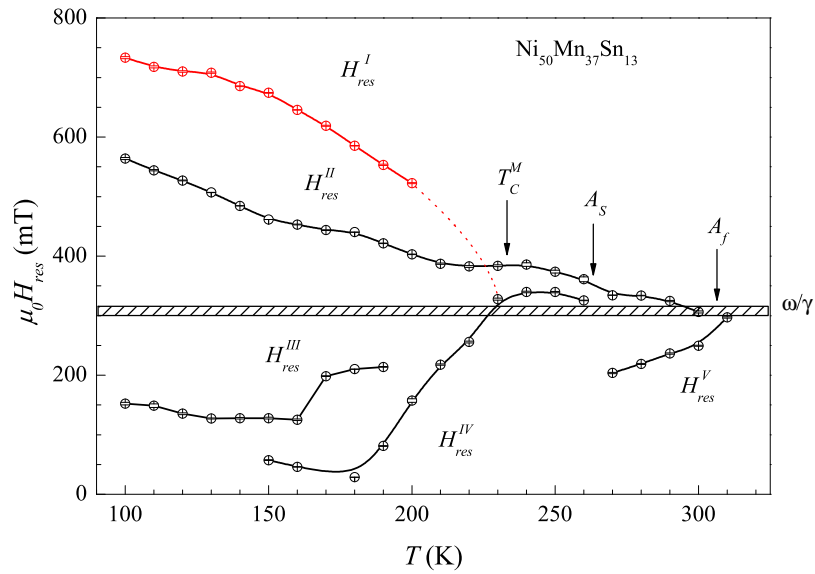
Figure 4.44: Temperature-dependence of the resonance field in $Ni_{50}Mn_{37}Sn_{13}$. Additional AF interactions appear below T_C^M. ω/γ indicates the isotropic value.

The temperature dependence of the resonance fields $\mu_0 H_{res}(T)$ extracted from Lorentzian lines fitted to the signals are shown in Fig. 4.43 and Fig. 4.44. The detailed fitting procedures is given in Appendix A2. The isotropic value is shown approximately with the horizontal bar. T_C^M, A_s and A_f are indicated with arrows. The sample is first cooled to the lowest temperature in the absence of magnetic field, and the data are taken on increasing temperature. At 100 K, in the martensitic state, the sample incorporates AF entities for which the spectra are labelled H_{res}^I and H_{res}^{II} and FM entities labelled as H_{res}^{III} (Fig. 4.43). Such a mixture of magnetic states is present up to about T_C^M. Above T_C^M, the AF component disappears and only FM components remain. The FM signals are observed in the temperature range $100 \leq T \leq 300$ K. $\mu_0 H_{res}(T)$, which is shown with H_{res}^I and has a higher resonance field than ω/γ, decreases monotonically with increasing temperature. The behavior of $\mu_0 H_{res}(T)$ can be understood when comparing it to the behavior of $M(T)$ in the ZFC state. The splitting of the ZFC and FC $M(T)$-curves below T_C^M is understood to be due to the pinning of the FM domains due to coexisting AF components. The AF exchange weakens with increasing temperature so that the FC and ZFC branches of $M(T)$ merge at T_C^M (Fig. 4.41(a)). This is reflected as a decrease in $\mu_0 H_{res}(T)$ with increasing temperature.

The intensity of the FMR signal is proportional to the magnetic susceptibility, and for H_{res}^{II} it is shown as a function of temperature in the inset of Fig. 4.43. From 100 K to a temperature close to A_s, the intensity is nearly constant with a low value and, then, increases with increasing temperature following a similar dependence in $M(T)$ as FM austenite develops.

The temperature-dependence of the resonance field $\mu_0 H_{res}(T)$ is seen in Fig. 4.44 for Ni$_{50}$Mn$_{37}$Sn$_{13}$. At 100 K, the alloy exhibits two magnetic contributions which are AF and FM located below and above ω/γ. Below T_C^M, the FMR signals H_{res}^I and H_{res}^{II} appear above ω/γ which are related to weak AF ordering. H_{res}^I is related to AF exchange which is consistent with the behavior of $M(T)$ as in the case of Ni$_{50}$Mn$_{35}$In$_{15}$. H_{res}^{II} is particularly significant for $100 \leq T \leq 300$ K. It approaches the isotropic value close to T_C^A. Closer details of the development of H_{res}^I and H_{res}^{II} can be seen in Fig. 4.45(a) for $T \leq 200$ K. H_{res}^{II} and H_{res}^{IV} are indicated in Fig. 4.45(b) for $T \geq 200$ K. H_{res}^I and H_{res}^{II} decrease with increasing temperature (Fig. 4.45(a)). The inset in Fig. 4.45(a) shows that H_{res}^{II} exists at 5 K as well. In Fig. 4.45(b), H_{res}^{II} decreases and H_{res}^{IV} increases with increasing temperature. Then, they superpose above 240 K, which lies above A_s. Angular dependence of FMR measurements have been performed at 160 K and 300 K. No angular-dependent signals in the austenitic and martensitic states have
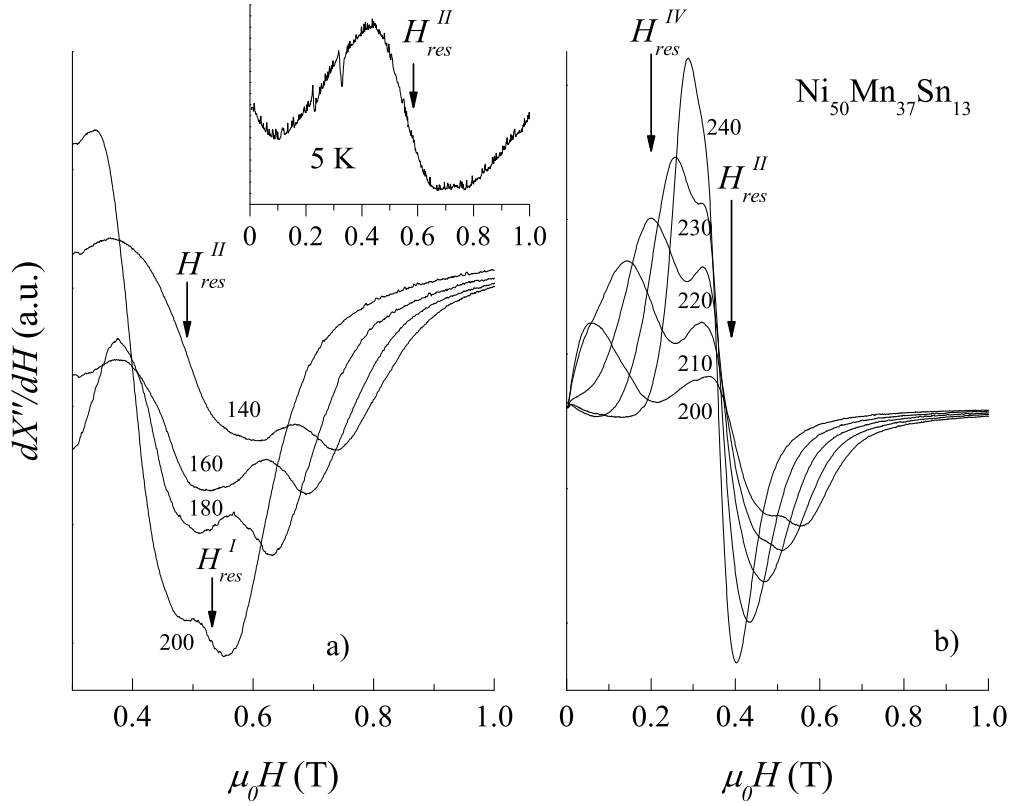
Figure 4.45: Temperature-dependence of the FMR signals for $Ni_{50}Mn_{37}Sn_{13}$. (a) H_{res}^{I} and H_{res}^{II} are shown at selected temperatures below T_C^M, and (b) the overlapping FMR signals H_{res}^{II} and H_{res}^{IV} between 200, and 240 K are shown. Inset in (a) shows the FMR signal at 5 K.

been detected indicating that there are no powder-related features arising coming from differently oriented domains.

The intensities of H_{res}^{II} (open circles) and the FM H_{res}^{IV} and H_{res}^{V} are shown in Fig. 4.46. The intensities of H_{res}^{II} and H_{res}^{IV} are almost temperature-independent at low temperatures up to 170 K, and both begin to gain intensity by further increasing the temperature. Around A_s, the intensities of the two signals reach their maximum values. Above 260 K, it becomes difficult to distinguish the signals. FM H_{res}^{IV}, reaches a maximum intensity at 250 K, and, above this temperature, the FM part diminishes, reflecting an overall decrease of the magnetic moment. At 270 K, the intensity of H_{res}^{V} starts to increase meaning that the magnetization increases as long-range FM ordering sets in and becomes dominant. The sharp decrease in $M(T)$ for $Ni_{50}Mn_{37}Sn_{13}$ just below M_s while cooling is revealed to be related to the loss of ferromagnetism and the first appearance
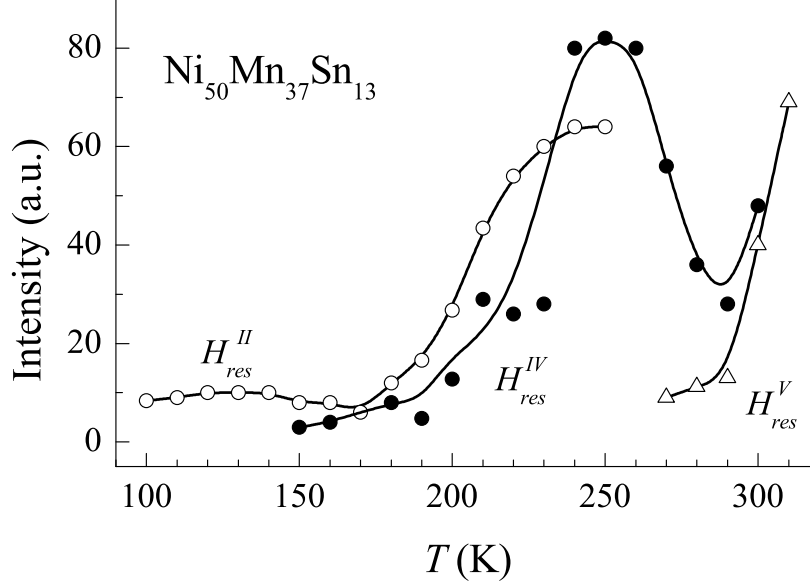
Figure 4.46: The intensity of the FMR signals related to the H_{res}^{II}, H_{res}^{IV} and H_{res}^{V} as a function of temperature in $Ni_{50}Mn_{37}Sn_{13}$. Open circles represent the intensity of AF H_{res}^{II}.

of AF correlations at 250 K. Here, neutron depolarization measurements show a local maximum in $R_F(T)$ (Fig. 4.33(c)). Analogously, one can observe the development of AF interactions in the present FMR data particularly through the temperature-behavior of H_{res}^{II} in $Ni_{50}Mn_{37}Sn_{13}$.

The results of the FMR experiments show the presence of mixed magnetic phases below M_s. Figures 4.47(a) and (b) show ZFC-$M(T)$ in $Ni_{50}Mn_{35}In_{15}$ and $Ni_{50}Mn_{37}Sn_{13}$ respectively. Different magnetic regions are separated by dotted lines according to the FMR results for $Ni_{50}Mn_{37}Sn_{13}$ and $Ni_{50}Mn_{35}In_{15}$. In Fig. 4.47(a), above T_C^A, Ni-Mn-In is PM, and between T_C^A and A_s, the magnetic state is FM. In a narrow region between A_s and T_C^M, a weak AF signal is accompanied by a FM signal in the FMR spectrum. Below T_C^M, the magnetic structure is more complex and two AF signals appear together with a FM signal.

In Fig. 4.47(b), the magnetic state of $Ni_{50}Mn_{37}Sn_{13}$ is PM above T_C^A, and ferromagnetism appears below T_C^A. In the region $A_s \leq T \leq A_f$, AF and FM signals coexist, however below A_s, only an AF signal is observed down to T_C^M. As in the case of $Ni_{50}Mn_{35}In_{15}$, mixed AF and FM magnetic structures coexist below T_C^M. The presence
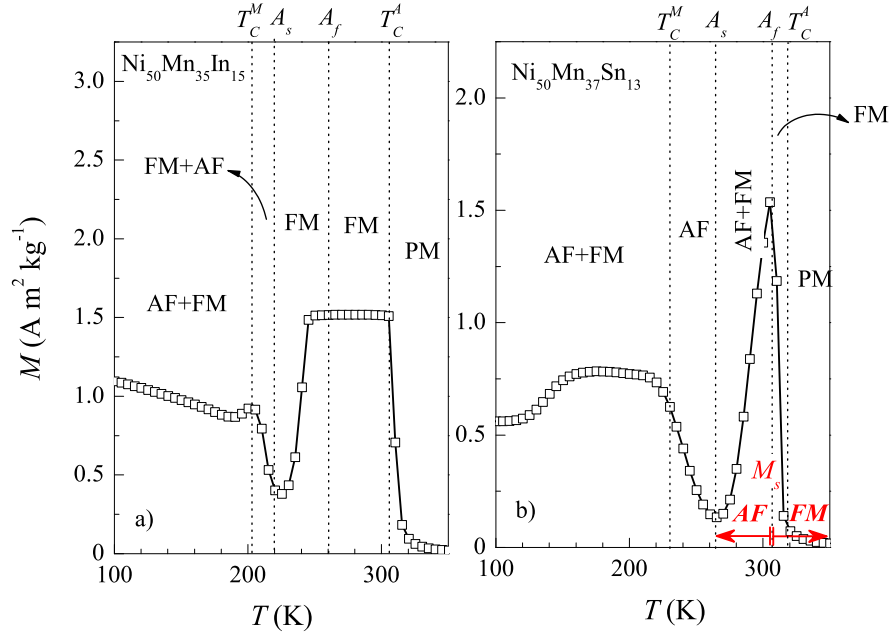
Figure 4.47: The ZFC $M(T)$ in the range $100 \leq T \leq 350$ K for (a) $Ni_{50}Mn_{35}In_{15}$ and (b) $Ni_{50}Mn_{37}Sn_{13}$. Different magnetic states obtained from the results of FMR data are separated by dotted lines. The result of polarization analysis above and below M_s are shown in red color. Arrows indicate AF and FM correlated regions.

of H_{res}^{I} and H_{res}^{II} above ω/γ indicates the occurrence of an AF phase in the martensitic state (see figure 4.44). The higher value of H_{res}^{II} than the one observed in Fig. 4.43 indicates that AF correlations may be weaker in $Ni_{50}Mn_{35}In_{15}$. The presence of H_{res}^{I} for both alloys is related to AF components appearing below T_C^M.

The results of the FMR and the polarized neutron scattering experiments for $Ni_{50}Mn_{37}Sn_{13}$ complement one another. The FMR measurements provide information on the nature of long-range magnetic ordering, whereas neutron polarization analysis provides information on short-range magnetic correlations within essentially paramagnetic states. In this manner the nature of magnetic interactions can be understood at all temperatures in martensitic Heusler alloys.

The observation of exchange bias in the martensitic state suggests the presence of AF interactions in Ni-Mn-In, Ni-Mn-Sn and Ni-Mn-Sb Heusler alloys [14–16,35]. AF interactions are revealed here directly by FMR experiments. Recently, the results of Mössbauer experiments had suggested the presence of a paramagnetic state below M_s [101,102]. The separation of ZFC and FC states in $M(T)$ below T_C^M under an mag-

netic field was interpreted as being due to the presence of magnetically inhomogeneous phases in the martensitic state [6]. On the other hand neutron diffraction studies on $Ni_2Mn(Mn_xSn_{1-x})$ alloys pointed out that Mn atoms which substitute for Sn atoms are coupled antiferromagnetically to the ferromagnetically coupled Mn sublattices [103].

4.4   Effect of the Hydrostatic Pressure on Martensitic Transformations

In the following, the effect of pressure on the magnetic and structural properties of Ni-Mn-In Heusler alloys is studied using magnetization, DSC and neutron depolarization measurements. Neutron polarization analysis is also performed for $Ni_{50}Mn_{40}Sb_{10}$ under pressure.

4.4.1   Magnetization and calorimetric measurements under pressure

$M(T)$ at selected applied pressures for $Ni_{50}Mn_{34}In_{16}$ is shown in Fig. 4.48 in a low external magnetic field of 5 mT. Data have been taken in ZFC, FC, and FH states. Results for ambient pressure agree with those previously shown in Fig. 4.2(a). On cooling, the cubic phase orders ferromagnetically at $T_C^A = 310$ K which causes a sharp increase in the magnetization in the austenitic state. At M_s, the martensitic transformation takes place, and the typical sharp drop in the magnetization is observed. Upon further cooling, the magnetization rises again, reflecting the increase in ferromagnetic order in the martensite phase. The application of pressure has little effect on the magnetic behavior of the high temperature cubic austenite phase. T_C^A increases slightly with increasing pressure, in agreement with earlier data reported for Heusler alloys [104–106] and are consistent with the predictions of first principles calculations [107]. Also, below about 150 K, well in the martensitic state, the temperature behavior of the magnetization remains nearly the same at all pressures. However, pressure has a significant effect on the magnetic behavior in the temperature region where the austenite and martensite phases coexist. All characteristic temperatures associated with the martensitic transition shift to higher values as the pressure is increased which is shown in the inset of Fig. 4.48 (M_s and A_f exhibit similar behavior with pressure). Another feature is that the difference in the magnetization between martensitic and austenitic states around the transition becomes larger with increasing pressure. As it was shown in section 4.3.1, AF interactions appear below M_s. It is expected that applied pressure would enhance the AF exchange in the martensite phase.

We have performed differential calorimetric measurements under pressure to obtain further information on pressure effects on the martensitic transition. The thermal curves for powder $Ni_{50}Mn_{35}In_{15}$ at selected hydrostatic pressures are shown in Fig. 4.49, where the exothermal and endothermal peaks corresponding to the forward and reverse tran-
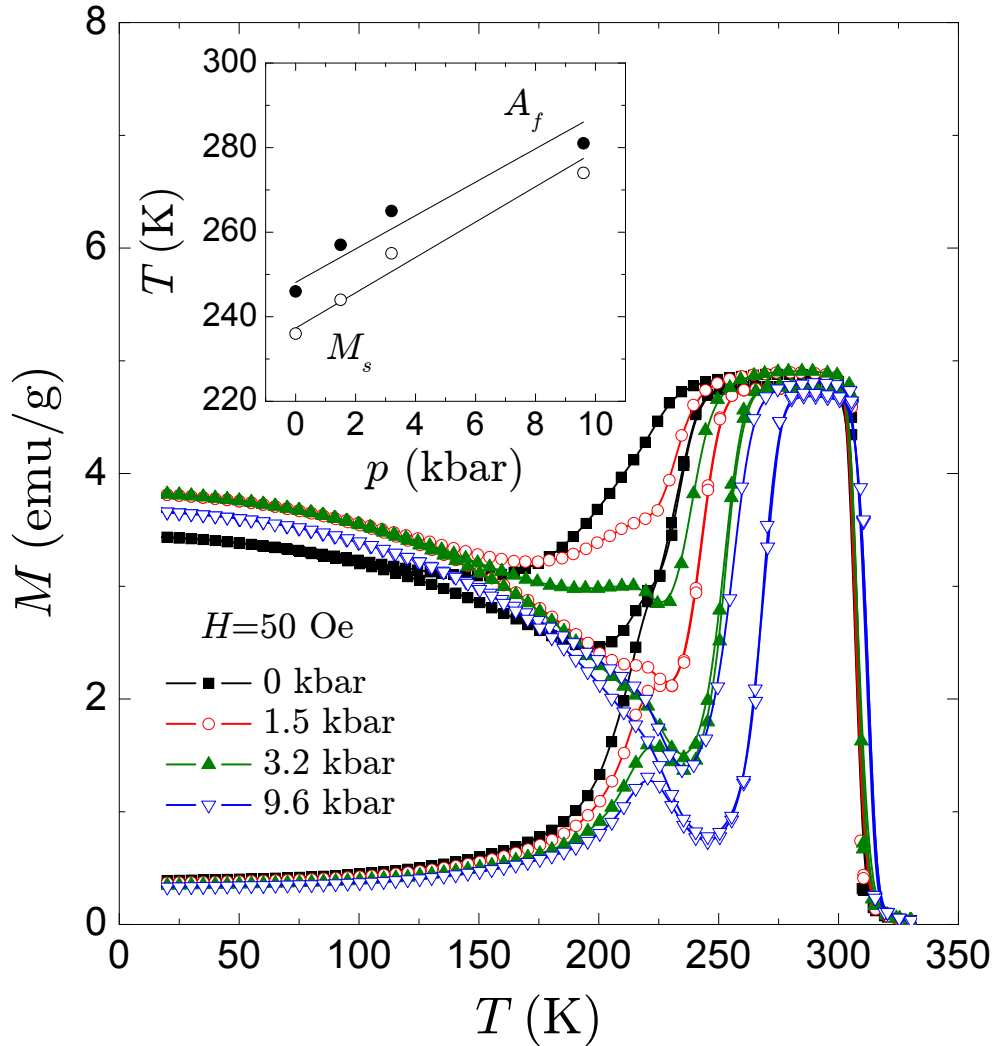
Figure 4.48: The temperature dependence of magnetization curves of $Ni_{50}Mn_{34}In_{16}$ for selected applied pressures under 5 mT magnetic field in ZFC, FC and FH states. The inset shows the change of M_s and A_f as a function of applied pressure.

sitions on cooling and heating, respectively, are seen. Application of pressure does not significantly alter the shape of the thermal peak, but both forward and reverse transitions shift towards higher temperatures as the pressure increases. The rate of shifts in the transition temperatures in $Ni_{50}Mn_{35}In_{15}$, $dT/dp \approx 2K$ kbar^{-1}, is lower than in $Ni_{50}Mn_{34}In_{16}$, $dT/dp \approx 4K$ kbar^{-1}.

4.4.2   Polarized neutron scattering under pressure

Application of pressure is expected to enhance AF exchange present in the martensitic state so that we have performed neutron depolarization measurements on $Ni_{50}Mn_{35}In_{15}$ under hydrostatic pressures on the D7 spectrometer. $M(T)$ in ZFC, FC and FH states
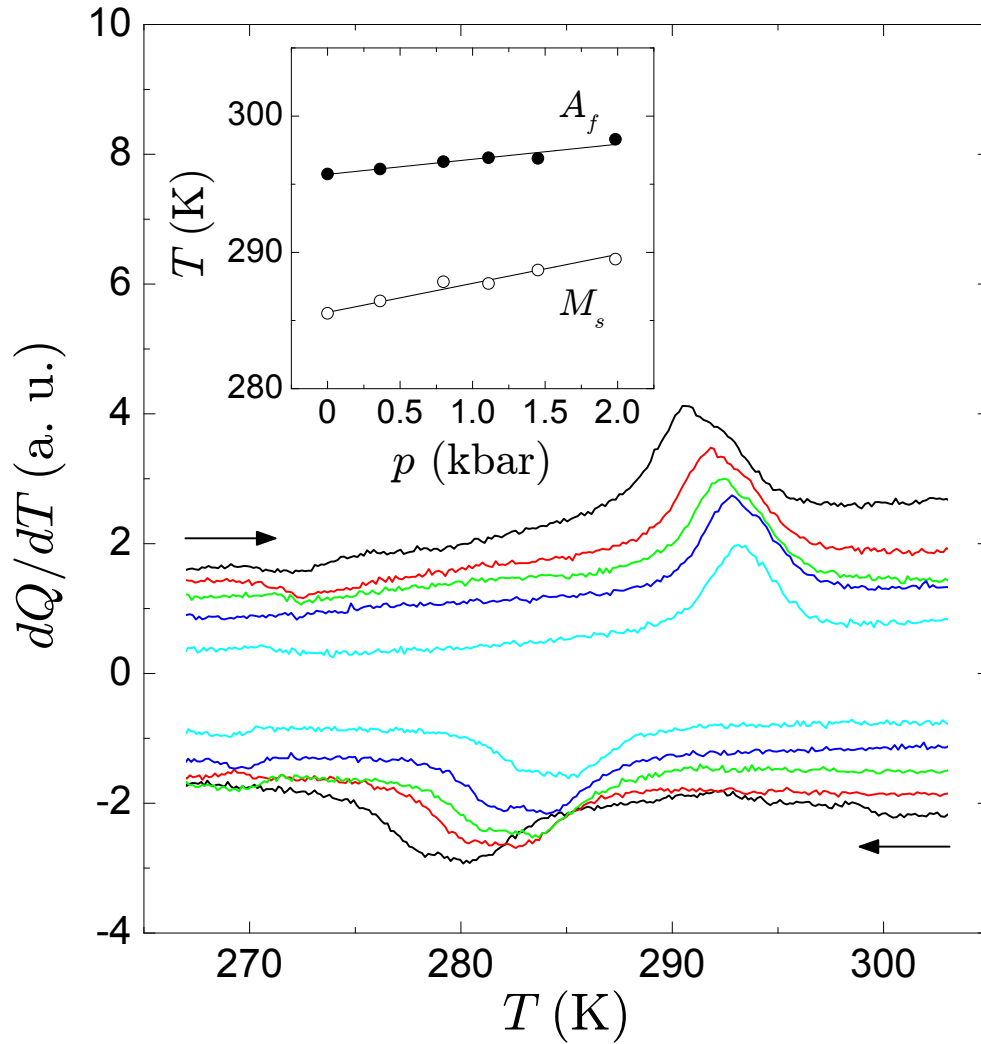
Figure 4.49: (a) Calorimetric measurements for selected values of applied pressure in $Ni_{50}Mn_{35}In_{15}$. From top to bottom (heating) and bottom to top (cooling) the applied pressures are: ambient, 0.36 kbar, 0.80 kbar, 1.11 kbar and 1.45 kbar. The inset shows M_s and A_f as a function of the applied pressure.

and $R_F(T)$ curves are shown in Fig. 4.50(a). FM ordering in the austenitic state occurs at $T_C^A = 295$ K, and the martensitic transformation takes place at $M_s = 274$ K. A sudden drop in magnetization below M_s is observed as in the case for $Ni_{50}Mn_{37}Sn_{13}$. However, here, the magnetization nearly vanishes in the range $200 \leq T \leq 225$ K. Below 200 K, long-range FM ordering develops gradually in the martensitic state until $T_C^M = 140$ K is reached. Figure 4.50(b) shows $R_F(T)$ taken on heating under 0.5 and 15 kbar hydrostatic pressure. Here 0.5 kbar is the pressure which is applied to close the pressure cell. Above T_C^A, R_F increases sharply to about 60 at 340 K when long-range FM ordering vanishes.
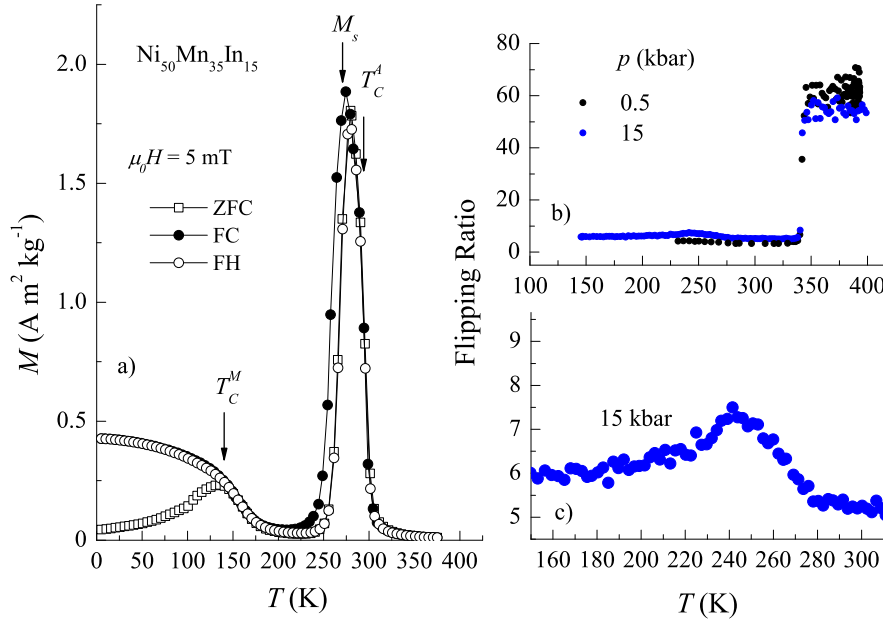
Figure 4.50: (a) $M(T)$ curve of $Ni_{50}Mn_{35}In_{15}$ alloy under 5 mT magnetic field. T_C^A, M_s and T_C^M are shown by arrows. (b) $R_F(T)$ for $Ni_{50}Mn_{35}In_{15}$ under 0.5 and 15 kbar pressures measured on heating. (c) $R_F(T)$ plotted in the range of $170 \leq T \leq 310$ K under 15 kbar.

Fig. 4.50(c) shows a detailed plot of $R_F(T)$ in the range $150 \leq T \leq 310$ K under 15 kbar. When the external pressure increases up to 15 kbar, R_F starts to increase and reaches a maximum value of 7.5 at 250 K which corresponds to a temperature just below M_s. This behavior shows that under pressure ferromagnetism can be suppressed and AF correlations may appear in Ni-Mn-In.

We carry out XYZ polarization analysis experiments under pressure in $Ni_{50}Mn_{40}Sb_{10}$ to investigate the pressure-dependence of the nature of magnetic coupling. Figure 4.51 shows the results of the polarization analysis at 320 K for $Ni_{50}Mn_{40}Sb_{10}$ under 0.5 and 10 kbar. The q-dependence of $(d\sigma/d\Omega)_{nuc}$ is given in Fig. 4.51(a). The diffraction pattern is similar to the pattern in Fig. 4.35(a) in the absence of pressure. The only difference is the additional nuclear scattering coming from Fluorinert which is used as the pressure-transmitting medium. Fluorinert gives amorphous-like scattering peaked around 1 Å^{-1} at 0.5 kbar, and it shifts to about 1.25 Å^{-1} at 15 kbar. The q-dependence of $(d\sigma/d\Omega)_{mag}$ is plotted in Fig. 4.51(b) for 0.5 kbar and 10 kbar at 320 K. The green line shows the magnetic scattering at ambient pressure (see Fig. 4.35(b)). The broad diffuse scattering centered at about 1.6 Å^{-1} exist also under pressure and is due to AF

correlations. However, in this case, when the pressure increases, the scattering at low q values also increases indicating that FM correlations also develop.
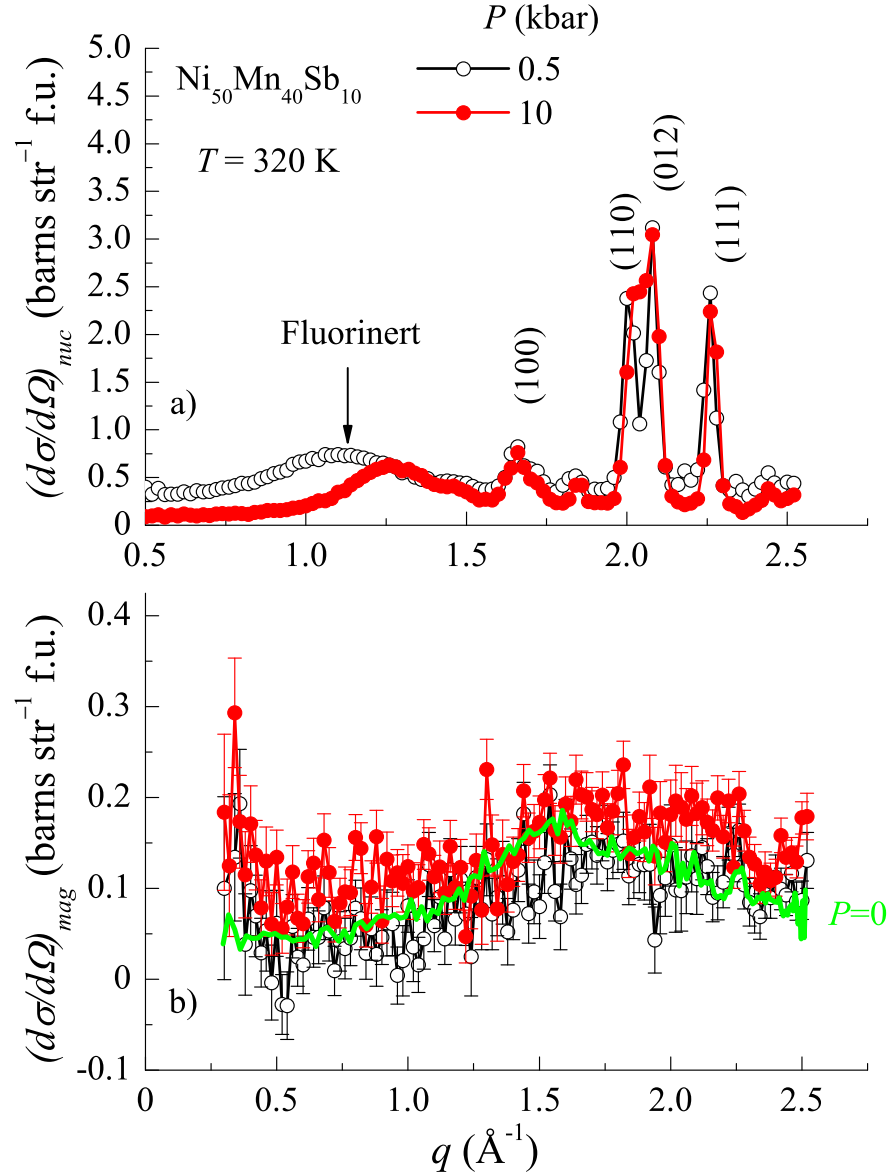
Figure 4.51: q-dependence of the neutron scattering cross-sections in the martensitic (320 K) states of $Ni_{50}Mn_{40}Sb_{10}$ ($M_s = 440$ K). (a) The nuclear cross-section plotted in the range $0.5 \leq q \leq 2.6$ Å^{-1} under 0.5 and 10 kbar pressure. At lower q, the nuclear scattering of fluorinert is seen. The structure is 4O orthorhombic. (b) The magnetic cross-section in the martensitic state at 320 K. The green line shows the magnetic scattering at ambient pressure.

The results of polarization analysis and FMR experiments are compared to the result of density functional theory (DFT) calculations. The magnetic exchange parameters have been calculated for Ni-Mn-Sb within DFT [108]. The exchange parameters for the cubic $L2_1$ phase is shown in Fig. 4.52 along with the $L2_1$ cubic structure of Ni-Mn-Sb. Ni, Mn and Sb sites are indicated by black, pink and blue spheres. It is assumed that Mn_1 and Mn_2 refer to Mn atoms located on the original Mn sites and on the Sb sites, respectively. We observe coexistence of strong FM Mn-Ni (Mn_1-Ni and Mn_2-Ni) interactions and AF interactions between nearest neighbor Mn_1-Mn_2 atoms. As a result of the larger number of the nearest neighbor Mn-Ni interactions, ferromagnetism can prevail and $Ni_2Mn_{1.6}Sb_{0.4}$ (corresponding to $Ni_{50}Mn_{40}Sb_{10}$) behaves as a ferromagnet in the austenitic state.
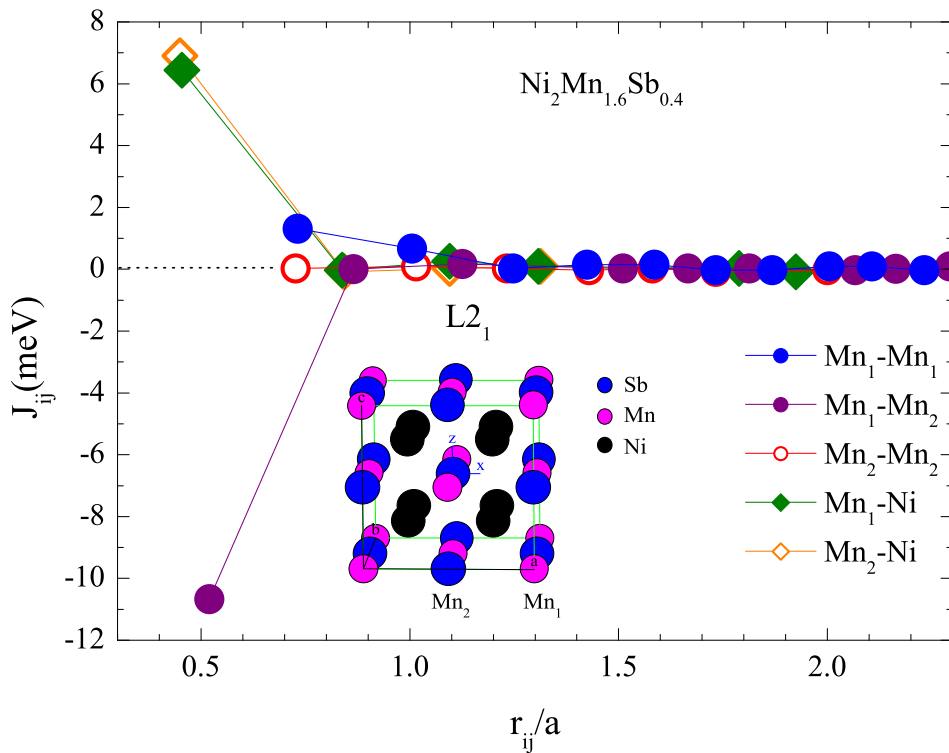
Figure 4.52: The exchange parameters J_{ij} between pairs of atoms i and j for different coordination shells obtained by DFT calculations for the cubic $L2_1$ austenite phase in $Ni_2Mn_{1.6}Sb_{0.4}$ ($Ni_{50}Mn_{40}Sb_{10}$) with the $L2_1$ cubic structure. The coordination shells are characterized by their interatomic distance r_{ij} given in units of the cubic lattice constant. The Ni-Ni contributions and the interactions with Sb-atoms are small and, thus, are omitted for clarity.
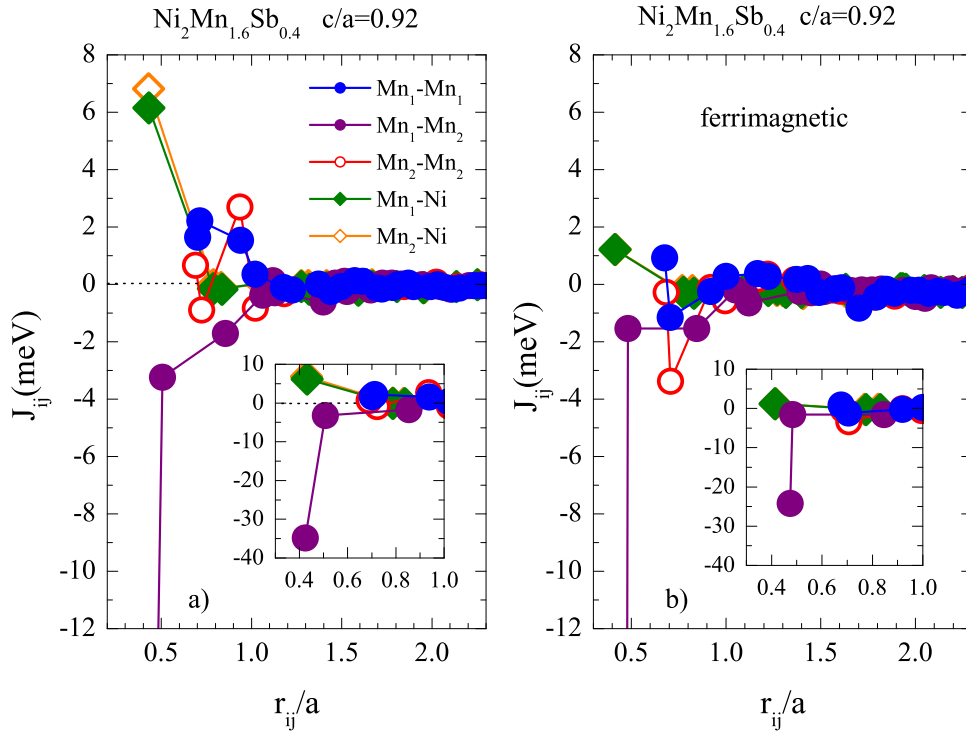
Figure 4.53: Comparison of the exchange parameters J_{ij} between pairs of atoms i and j for different coordination shells obtained by DFT calculations for a tetragonally distorted structure with the c-axis reduced by 8% relative to the *a*- and *b*-axis in $Ni_2Mn_{1.6}Sb_{0.4}$ ($Ni_{50}Mn_{40}Sb_{10}$) for (a) ferromagnetic and (b) ferrimagnetic configurations. The coordination shells are characterized by their interatomic distances r_{ij} given in units of the cubic lattice constant. The Ni-Ni contributions and the interactions with Sb-atoms are small and, thus, omitted for clarity.

In the martensitic state, a competition between FM, AF and even ferrimagnetic (FI) configurations can occur. The DFT calculations are done for a tetragonally distorted martensite structure by reducing the *c*-axis by 8% with respect to the *a*-axis (c/a=0.92) in $Ni_2Mn_{1.6}Sb_{0.4}$, and in the FI configuration, the Mn spins on the Sb sites (Mn_2) are assumed to be flipped. A comparison of the exchange parameters for the tetragonal case is shown in Figs. 4.53(a) and (b) for FM and FI configurations respectively. In the FM configuration, AF nearest neighbor Mn_1-Mn_2 interactions are stronger than FM Mn-Ni interactions, and as a result of large number of AF interactions in the martensitic state, the magnetic coupling in the tetragonally distorted state of $Ni_2Mn_{1.6}Sb_{0.4}$ can be AF. In Fig. 4.53(b), the FI configuration exhibits a significant decrease of the FM Mn-Ni contributions, which is caused by the breakdown of the induced moments on the Ni-sites. The Mn_1-Mn_2 interaction is stronger than the Mn-Ni interactions. In both AF and FI

cases, the tetragonal distortion leads to a significant strengthening of AF interactions in the martensitic state.

The results of these calculations suggest that AF interactions occur in $Ni_2Mn_{1.6}Sb_{0.4}$ in the tetragonally distorted state and are in agreement with the results of FMR and neutron scattering experiments.

5. Conclusion and Outlook

In this thesis various experimental techniques were used to understand magnetic and structural properties of Ni-Mn-based martensitic Heusler alloys under three main goals. The first goal was to design new Heusler materials and to investigate the basic properties. For this purpose, a method was provided based on the e/a dependence of M_s for different Ni-Mn-based Heusler alloys. At constant e/a, by Ga substitution for In in $Ni_{50}Mn_{34}In_{16}$, M_s shifted to higher temperatures so that favorable properties of $Ni_{50}Mn_{34}In_{16}$, such as the magnetocaloric effect and the magnetic-field-induced strain were brought to the vicinity of room temperature. At increased e/a, by partially substituting Sn for In, the magnetocaloric effect was improved from 8 to about 21 $Jkg^{-1}K^{-1}$, while the magnetic superelasticity was preserved. The adiabatic temperature-change was measured directly in these alloys using a magneto-calorimeter. ΔT_{ad} measurements showed that applying a magnetic field leads to a temperature increase of the material around T_C^A (conventional MCE), and a temperature decrease below M_s (inverse MCE). Table 5.1 summarizes the magnetocaloric properties of $Ni_{50}Mn_{34}In_{16}$ and its substituted alloys.

The second goal was to investigate the effect of a magnetic cooling-field. We proposed that the temperature dependence of strain under a magnetic cooling-field could be useful in providing information on the easy-direction of magnetization in the martensitic state using polycrystalline samples. The easy-direction of magnetization is found to be along the short-axis in $Ni_{50}Mn_{27}Ga_{23}$ and $Ni_{50}Mn_{35}Sn_{15}$, whereas in $Ni_{50}Mn_{34}In_{16}$ and $Ni_{50}Mn_{37}Sb_{13}$, the easy-direction is along the long-axis. The results were confirmed by comparing the well-known properties of single crystalline Ni_2MnGa Heusler alloys.

The structural properties of Ni-Mn based Heusler alloys were investigated in the absence of magnetic field and in the presence of a cooling-field. In $Ni_{50}Mn_{34}In_{16}$, the austenite and martensite phases coexisted in the martensitic state when the sample was cooled through M_s in a magnetic field. 45% rest-austenite phase was found at 5 K under 5 T cooling-field.

The third goal was to understand the nature of magnetic interactions in Ni-Mn based Heusler alloys. For this purpose neutron polarization analysis and ferromagnetic resonance experiment were undertaken. The presence of exchange-bias and the broad temperature range of the FM transition in the martensitic state suggested the presence of AF coupling below M_s. However, until now, no direct evidence has been provided for the presence of antiferromagnetism. We show here that the q-dependence of the magnetic scattering of $Ni_{50}Mn_{40}Sb_{10}$ below M_s shows features related to the presence

Sample	T_C^M(K)	M_s(K)	T_C^A(K)	ΔS(Jkg^{-1}K^{-1})	ΔT_{ad}(K)
Ni$_{50}$Mn$_{34}$In$_{16}$	225	243	308	8/-5	-2/3.5
Ni$_{50}$Mn$_{34}$In$_{14}$Ga$_2$	210	275	293	8/-5	-2/3.5
Ni$_{50}$Mn$_{34}$In$_{12}$Ga$_4$	135	347	–	–/–	–/–
Ni$_{50}$Mn$_{34}$In$_{15}$Sn$_1$	225	243	305	20.6/–	-7/–

Table 5.1: The characteristic temperatures T_C^M, M_s, T_C^A and ΔS and ΔT_{ad} for the inverse and conventional MCE are listed for Ni$_{50}$Mn$_{34}$In$_{16}$ and its quaternary alloys.

of short-range AF correlations. Above the martensitic transformation of this alloy, in spite of the absence of long-range FM ordering, we observed the presence of FM short-range correlations. Similar experiments on Ni$_{50}$Mn$_{37}$Sn$_{13}$ showed also the presence of FM correlations above M_s. However, just below M_s, only AF coupling was observed explaining the sudden drop in $M(T)$ below the martensitic transformation. In the PM region above T_C^A, the FM short-range correlations were still observed in the magnetic scattering. FMR results in Ni$_{50}$Mn$_{37}$Sn$_{13}$ showed in addition to the presence of AF correlations below M_s, the appearance of AF exchange concurrently with the appearance of long-range FM ordering below T_C^M. These results show the existence of a mixed magnetic state in the martensite phase. Similarly, in Ni$_{50}$Mn$_{35}$In$_{15}$, FMR experiments showed the presence of AF exchange coexisting together with long-range FM ordering below T_C^M.

The pressure dependence of $M(T)$ in Ni$_{50}$Mn$_{35}$In$_{15}$ showed the presence of a shift of M_s by about 4 K kbar^{-1}. It was found that the rate of change in the transition temperature with both pressure and magnetic field in this alloy was larger than in other Ni-Mn-Z Heusler alloys. In addition to the shift of M_s to higher temperatures, $M(T)$ decreased below M_s more quickly with increasing pressure, and reached smaller values than $M(T)$ at ambient pressure. $R_F(T)$ at ambient pressure showed no AF correlations in Ni$_{50}$Mn$_{34}$In$_{16}$ in the range $T_C^M \leq T \leq M_s$. This result is found to be consistent with those obtained from FMR studies. However, under 15 kbar, emerging AF interactions are suggested by the increase in R_F in this temperature range. This showed that by applying pressure, the spin orientation can be influenced in the martensitic state just below M_s in Ni$_{50}$Mn$_{34}$In$_{16}$. AF exchange was found to appear under ambient pressure only for $T < T_C^M$ by FMR studies.

Further studies under pressure were carried out also for Ni$_{50}$Mn$_{40}$Sb$_{10}$. The magnetic scattering shows that AF short-range correlations are still present under 10 kbar in the

martensitic state. The results were found to be in good agreement with those of DFT calculations. These results contribute to the understanding of the physical properties of martensitic Heusler alloys and can serve as guides to optimize their properties for applications.

The experimental results in this work on Ni-Mn based Heusler alloys find support from theoretical predictions. For further studies, one can now consider the results of theoretical calculations as a starting point to design new high-strain materials based on martensitic transitions and optimize their properties for promising technological applications.

A   Appendix

A1   Polarization Analysis

The total cross-section in the case of spin-flip and non-spin-flip scattering (SF and NSF) can be separated into the partial differential cross-section in the x, y and z directions. These include all kinds of scattering as, nuclear-coherent (COH), magnetic (MAG), nuclear spin-incoherent (N) and isotope incoherent(II) scattering.

$$\left(\frac{\partial^2\sigma}{\partial\Omega\partial E}\right)_{SF}^{z} = \frac{2}{3}\left(\frac{\partial^2\sigma}{\partial\Omega\partial E}\right)_{N} + \frac{1}{2}\left(\frac{\partial^2\sigma}{\partial\Omega\partial E}\right)_{MAG}, \tag{14}$$

$$\left(\frac{\partial^2\sigma}{\partial\Omega\partial E}\right)_{NSF}^{z} = \frac{1}{3}\left(\frac{\partial^2\sigma}{\partial\Omega\partial E}\right)_{N} + \frac{1}{2}\left(\frac{\partial^2\sigma}{\partial\Omega\partial E}\right)_{MAG} + \left(\frac{\partial^2\sigma}{\partial\Omega\partial E}\right)_{COH} + \left(\frac{\partial^2\sigma}{\partial\Omega\partial E}\right)_{II}, \tag{15}$$

$$\left(\frac{\partial^2\sigma}{\partial\Omega\partial E}\right)_{SF}^{y} = \frac{2}{3}\left(\frac{\partial^2\sigma}{\partial\Omega\partial E}\right)_{N} + \left(1+\sin^2\alpha\right)\frac{1}{2}\left(\frac{\partial^2\sigma}{\partial\Omega\partial E}\right)_{MAG}, \tag{16}$$

$$\left(\frac{\partial^2\sigma}{\partial\Omega\partial E}\right)_{NSF}^{y} = \frac{1}{3}\left(\frac{\partial^2\sigma}{\partial\Omega\partial E}\right)_{N} + \left(\cos^2\alpha\right)\frac{1}{2}\left(\frac{\partial^2\sigma}{\partial\Omega\partial E}\right)_{MAG} + \left(\frac{\partial^2\sigma}{\partial\Omega\partial E}\right)_{COH} + \left(\frac{\partial^2\sigma}{\partial\Omega\partial E}\right)_{II}, \tag{17}$$

$$\left(\frac{\partial^2\sigma}{\partial\Omega\partial E}\right)_{SF}^{x} = \frac{2}{3}\left(\frac{\partial^2\sigma}{\partial\Omega\partial E}\right)_{N} + \left(1+\cos^2\alpha\right)\frac{1}{2}\left(\frac{\partial^2\sigma}{\partial\Omega\partial E}\right)_{MAG}, \tag{18}$$

$$\left(\frac{\partial^2\sigma}{\partial\Omega\partial E}\right)_{NSF}^{x} = \frac{1}{3}\left(\frac{\partial^2\sigma}{\partial\Omega\partial E}\right)_{N} + \left(\sin^2\alpha\right)\frac{1}{2}\left(\frac{\partial^2\sigma}{\partial\Omega\partial E}\right)_{MAG} + \left(\frac{\partial^2\sigma}{\partial\Omega\partial E}\right)_{COH} + \left(\frac{\partial^2\sigma}{\partial\Omega\partial E}\right)_{II}. \tag{19}$$

By combining these cross sections one can separate the different contributions of the different cross-sections. In the absence of magnetic scattering, nuclear coherent and nuclear-spin incoherent cross-sections can be obtain in any direction from the measured SF and NSF cross sections.

$$\left(\frac{\partial^2\sigma}{\partial\Omega\partial E}\right)_N = \frac{3}{2}\left(\frac{\partial^2\sigma}{\partial\Omega\partial E}\right)^z_{SF},$$

$$\left(\frac{\partial^2\sigma}{\partial\Omega\partial E}\right)_{COH} + \left(\frac{\partial^2\sigma}{\partial\Omega\partial E}\right)_{II} = \left(\frac{\partial^2\sigma}{\partial\Omega\partial E}\right)^z_{NSF} - \frac{1}{2}\left(\frac{\partial^2\sigma}{\partial\Omega\partial E}\right)^z_{SF}.$$

Rearranging the measured six partial differential cross-sections (Eq. 14-19), the magnetic scattering can be obtained in two ways:

$$\left(\frac{\partial^2\sigma}{\partial\Omega\partial E}\right)_{MAG} = 2\left[\left(\frac{\partial^2\sigma}{\partial\Omega\partial E}\right)^x_{SF} + \left(\frac{\partial^2\sigma}{\partial\Omega\partial E}\right)^y_{SF} - 2\left(\frac{\partial^2\sigma}{\partial\Omega\partial E}\right)^z_{SF}\right],$$

$$\left(\frac{\partial^2\sigma}{\partial\Omega\partial E}\right)_{MAG} = 2\left[2\left(\frac{\partial^2\sigma}{\partial\Omega\partial E}\right)^z_{NSF} - \left(\frac{\partial^2\sigma}{\partial\Omega\partial E}\right)^x_{NSF} - \left(\frac{\partial^2\sigma}{\partial\Omega\partial E}\right)^y_{NSF}\right].$$

So that,the total spin-flip (TSF) and non-spin-flip (TNSF) cross-sections can be given as follows,

$$\left(\frac{\partial^2\sigma}{\partial\Omega\partial E}\right)_{TSF} = \left(\frac{\partial^2\sigma}{\partial\Omega\partial E}\right)^x_{SF} + \left(\frac{\partial^2\sigma}{\partial\Omega\partial E}\right)^y_{SF} + \left(\frac{\partial^2\sigma}{\partial\Omega\partial E}\right)^z_{SF},$$

$$\left(\frac{\partial^2\sigma}{\partial\Omega\partial E}\right)_{TNSF} = \left(\frac{\partial^2\sigma}{\partial\Omega\partial E}\right)^x_{NSF} + \left(\frac{\partial^2\sigma}{\partial\Omega\partial E}\right)^y_{NSF} + \left(\frac{\partial^2\sigma}{\partial\Omega\partial E}\right)^z_{NSF}.$$

The nuclear spin-incoherent (N) and nuclear coherent (COH) cross-sections can be defined as using the TSF and TNSF cross sections;

$$\left(\frac{\partial^2\sigma}{\partial\Omega\partial E}\right)_N = \frac{1}{2}\left(\frac{\partial^2\sigma}{\partial\Omega\partial E}\right)_{TSF} - \left(\frac{\partial^2\sigma}{\partial\Omega\partial E}\right)_{MAG},$$

$$\left(\frac{\partial^2\sigma}{\partial\Omega\partial E}\right)_{COH} + \left(\frac{\partial^2\sigma}{\partial\Omega\partial E}\right)_{II} = \frac{1}{6}\left[2\left(\frac{\partial^2\sigma}{\partial\Omega\partial E}\right)_{TNSF} - \left(\frac{\partial^2\sigma}{\partial\Omega\partial E}\right)_{TSF}\right].$$

The detailed derivation of these equations can be found in [72,109,110].

A2   The Fit Procedure of Ferromagnetic Resonance Signals

The data $(d\chi''/dH)$ were integrated to obtain $\chi''(\mu_0 H)$ which is characterized by a Lorentzian shape or a Dyson shape. After that, Lorentzian or Dyson function was fitted to the data using Origin program. In martenstic Heusler alloys, the analysis showed that the FMR signals can have a single or multiple Lorentzian lines. For example; in the paramagnetic austenite phase at 310 K, $Ni_{50}Mn_{37}Sn_{13}$ has a single Dyson line as shown in Fig. A1. However, in ferromagnetic austenite phase or in martensite phase FMR shows more than one signal. In Fig. A2(a) and (b) show FMR signals with a multiple structure at 180 K for $Ni_{50}Mn_{35}In_{15}$ and $Ni_{50}Mn_{37}Sn_{13}$ respectively. In Fig. A2(a), three and in (b) four signals are shown by green Lorentzian lines contributing to the signal. The location of the peaks gives H_{res}.
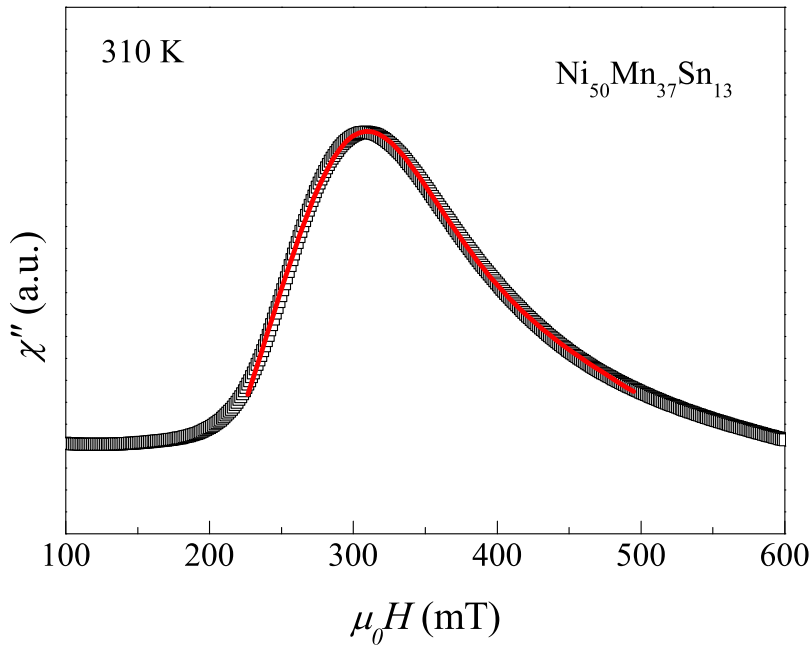
Figure A1: A Dyson line fitted to FMR signal at 310 K for $Ni_{50}Mn_{37}Sn_{13}$. Red line shows the calculated fit.
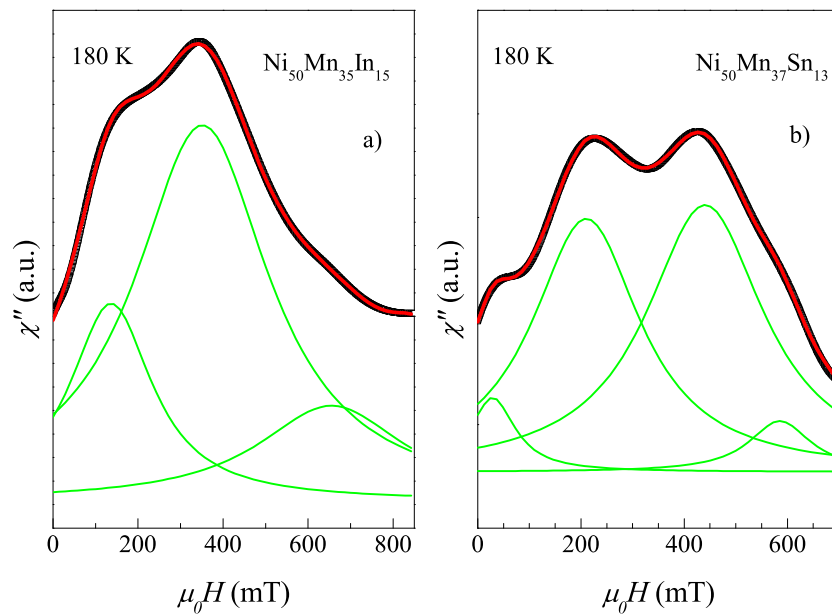
Figure A2: Multiple Lorentzian lines fitted to FMR signal at 180 K (a) for Ni$_{50}$Mn$_{35}$In$_{15}$ and (b) for Ni$_{50}$Mn$_{37}$Sn$_{13}$. Red lines show the calculated fits. The data are a sum of the Lorentzian lines.

List of Figures

List of Tables

References

[1] K. Ullakko, J. K. Huang, C. Kantner, R. C. O'Handley, and V. V. Kokorin, Large magnetic field induced strains in Ni_2MnGa single crystals, *Appl. Phys. Lett.* **69**, 1966 (1996).

[2] K. Ullakko, J. K. Huang, V. V. Kokorin and R. C. O'Handleyn, Magnetically controlled shape memory effect in Ni_2MnGa intermetallics, *Scripta Mater.* **36**, 1133 (1997).

[3] R. C. O'Handley, Model for strain and magnetization in magnetic shape-memory alloys, *J. Appl. Phys.* **83**, 3263 (1998).

[4] T. Krenke, *Untersuchung der martensitischen Umwandlung und der magnetischen Eigenschaften Mangan-reicher Ni-Mn-In- und Ni-Mn-Sn- Heusler-Legierungen*, Ph. D. thesis, Department of Physics, Universität Duisburg Essen (2007).

[5] T. Krenke, E. Duman, M. Acet, E. F. Wassermann, X. Moya, L. Mañosa, A. Planes, E. Suard and B. Ouladdiaf, Magnetic superelasticity and inverse magnetocaloric effect in Ni-Mn-In, *Phys. Rev. B* **75**, 104414 (2007).

[6] T. Krenke, M. Acet, E. F. Wassermann, X. Moya, L. Mañosa and A. Planes, Martensitic transitions and the nature of ferromagnetism in the austenitic and martensitic states of Ni-Mn-Sn alloys, *Phys. Rev. B* **72**, 014412 (2005).

[7] M. Khan, A. K. Pathak, M. R. Paudel, I. Dubenko, S. Stadler, and N. Ali, Magnetoresistance and field-induced structural transitions in $Ni_{50}Mn_{50-x}Sn_x$ Heusler alloys, *J. Magn. Magn. Mater.* **320**, L21 (2008).

[8] V. K. Pecharsky and K. A. Gschneider Jr., Giant magnetocaloric effect in $Gd_5(Si_2Ge_2)$, *Phys. Rev. Lett.* **78**, 4494 (1997).

[9] T. Krenke, E. Duman, M. Acet, E. F. Wassermann, X. Moya, L. Mañosa and A. Planes, Inverse magnetocaloric effect in ferromagnetic Ni-Mn-Sn alloys, *Nat. Mater.* **4**, 450 (2005).

[10] S. Y. Yu, Z. H. Liu, G. D. Liu, J. L. Chen, Z. X. Cao, G. H. Wu, B. Zhang and X. X. Zhang, Large magnetoresistance in single-crystalline $Ni_{50}Mn_{50-x}In_x$ alloys (x=14-16) upon martensitic transformation, *Appl. Phys. Lett.* **89**, 162503 (2006).

[11] K. Koyama, H. Okada, K. Watanabe, T. Kanomata, R. Kainuma, R. Kainuma, W. Ito, K. Oikawa and K. Ishida, Observation of large magnetoresistance of magnetic Heusler alloy $Ni_{50}Mn_{36}Sn_{14}$ in high magnetic fields, *Appl. Phys. Lett.* **89**, 182510 (2006).

[12] S. Y. Yu, L. Ma, G. D. Liu, Z. H. Liu, J. L. Chen, Z. X. Cao, G. H. Wu, B. Zhang and X. X. Zhang, Magnetic field-induced martensitic transformation and large magnetoresistance in NiCoMnSb alloys, *Appl. Phys. Lett.* **90**, 242501 (2007).

[13] Z. H. Liu, H. Liu, X. X. Zhang, X. K. Zhang, J. Q. Xiao, Z. Y. Zhu, X. F. Dai, G. D. Liu, J. L. Chen, and G. H. Wu, Large negative magnetoresistance in quaternary Heusler alloy $Ni_{50}Mn_8Fe_{17}Ga_{25}$ melt-spun ribbons, *Appl. Phys. Lett.* **86**, 182507 (2005).

[14] Z. Li, C. Jing, J. Chen, S. Yuan, S. Cao, and J. Zhang, Observation of exchange bias in the martensitic state of $Ni_{50}Mn_{36}Sn_{14}$ Heusler alloy, *Appl. Phys. Lett.* **91**, 112505 (2007).

[15] M. Khan, I. Dubenko, S. Stadler and N. Ali, Exchange bias behavior in Ni-Mn-Sb Heusler alloys, *Appl. Phys. Lett.* **91**, 072510 (2007).

[16] A. K. Pathak, M. Khan, B. R. Gautam, S. Stadler, I. Dubenko and N. Ali, Exchange bias in bulk Ni-Mn-In-based Heusler alloys, *J. Magn. Magn. Mater.* **231**, 963 (2009).

[17] http://www.magneticshape.de/

[18] C. M. Wayman, *Phase transformations, nondiffusive*, in *Physical Metallurgy; third, revised and enlarged edition*, Eds. R. W. Cahn and P. Haasen, P. 1031, Elsevier B. V., Amsterdam-The Netherlands (1983).

[19] T. Kakeshita, T. Fukuda and T. Kakeuchi, Magneto-mechanical evaluation for twinning plane movement driven by magnetic field in ferromagnetic shape memory alloys, *Mat. Sci. Eng. A* **438**, 12 (2006).

[20] O. Heczko, Magnetic shape memory effect and magnetization reversal, *J. Magn. Magn. Mater.* **290**, 787 (2005).

[21] A. Sozinov, A. A. Likhachev, N. Lanska and K. Ullakko, Giant magnetic-field-induced strain in NiMnGa seven-layered martensitic phase, *Appl. Phys. Lett.* **80**, 1746 (2002).

[22] O. Heczko, A. Sozinov and K. Ullakko, Giant field-induced reversible strain in magnetic shape memory NiMnGa alloy, *IEEE Trans. Magn.* **36**, 3266 (2000).

[23] S. J. Murray, M. Marioni, S. M. Allen, R. C. O'Handley and T. A. Lograsso, 6% magnetic-field-induced strain by twin boundary motion in ferromagnetic Ni-Mn-Ga, *Appl. Phys. Lett.* **77**, 886 (2000).

[24] A. E. Clark, *Ferromagnetic Materials, Vol. 1*, P. 531, North-Holland, Amsterdam (1980).

[25] G. H. Haertling, Ferroelectric Ceramics: History and Technology, *J. Amer. Chem. Soc.* **82**, 797 (1999).

[26] V. A. Chernenko, C. Segui, E. Cesari, J. Pons and V. V. Kokorin, Sequence of martensitic transformations in Ni-Mn-Ga alloys, *Phys. Rev. B* **57**, 2659 (1998).

[27] V. V. Kokorin, V. V. Martynov and V. A. Chernenko, Stress-induced martensitic transformations in nickel manganese gallium (Ni$_2$MnGa), *Scripta Matel. et Mater.* **26**, 175 (1992).

[28] J. Pons, V. A. Chernenko, R. Santamarta and E. Cesari, Crystal structure of martensitic phases in Ni-Mn-Ga shape memory alloys, *Acta Mater.* **48**, 3027 (2000).

[29] N. Lanska, O. Söderberg, A. Sozinov, Y. Ge, K. Ullakko and V. K. Lindroos, Composition and temperature dependence of the crystal structure of Ni-Mn-Ga alloys, *J. Appl. Phys.* **95**, 8074 (2004).

[30] A. Planes, L. Mañosa and M. Acet, Magnetocaloric effect and its relation to shape-memory properties in ferromagnetic Heusler alloys, *J. Phys.: Condens. Matter* **21**, 233201 (2009).

[31] S. Chatterjee, S. Giri, S. Majumdar, A. K. Deb, S. K. De and V. Hardy, Magneto-structural instability in Ni$_2$Mn$_{1.4}$Sb$_{0.6}$ alloy, *J. Phys.: Condens. Matter* **19**, 346213 (2007).

[32] Y. Sutou, Y. Imano, N. Koeda, T. Omori, R. Kainuma, K. Ishida, and K. Oikawa, Magnetic and martensitic transformations of NiMnX (X=In,Sn,Sb) ferromagnetic shape memory alloys, *Appl. Phys. Lett.* **85**, 4358 (2004).

[33] M. Khan, I. Dubenko, S. Stadler and N. Ali, Magnetostructural phase transitions in Ni$_{50}$Mn$_{25+x}$Sb$_{25-x}$ Heusler alloys, *J. Phys.: Condens. Matter* **20**, 235204 (2008).

[34] J. Du, Q. Zheng, W. J. Ren, W. J. Feng, X. G. Liu and Z. D. Zhang, Magneto-caloric effect and magnetic-field-induced shape recovery effect at room temperature in ferromagnetic Heusler alloy Ni-Mn-Sb, *J. Phys. D: Appl. Phys.* **40**, 5523 (2007).

[35] M. Khan, N. Ali and S. Stadler, Inverse magnetocaloric effect in ferromagnetic Ni$_{50}$Mn$_{37+x}$Sb$_{13-x}$ Heusler alloys, *J. Appl. Phys.* **101**, 053919 (2007).

[36] V. O. Golub, A. Y. Vovk, L. Malkinski, C. J. O'Connor, Z. Wang and J. Tang, Anomalous magnetoresistance in NiMnGa thin films, *J. Appl. Phys.* **96**, 3865 (2004).

[37] M. Kohl, Y. Liu, B. Krevet, S. Dürr and M. Ohtsuka, SMA microactuators for microvalve applications, *J. Phys. IV (France)* **115**, 333 (2004).

[38] K. Ullakko, Y. Ezer, A. Sozinov, G. Kimmel, P. Yakovenko, V. K. Lindroos, Magnetic-field-induced strains in polycrystalline Ni-Mn-Ga at room-temperature, *Scripta Mater.* **44**, 475 (2001).

[39] J. Feuchtwanger, S. Michael, J. Juang, D. Bono, R. C. O'Handley, S. M. Allen, C. Jenkins, J. Goldie and A. Berkowitz, Energy absorption in Ni-Mn-Ga polymer composites, *J. Appl. Phys.* **93**, 8528 (2003).

[40] N. Scheerbaum, D. Hinz, O. Gutfleisch, K. H. Müller and L. Schultz, Textured polymer bonded composites with Ni-Mn-Ga magnetic shape memory particles, *Acta Mater.* **55**, 2707 (2007).

[41] N. Scheerbaum, O. Heczko, J. Liu, D. Hinz, L. Schultz and O. Gutfleisch, Magnetic field-induced twin boundary motion in polycrystalline Ni-Mn-Ga fibres, *New J. Phys.* **10**, 073002 (2008).

[42] U. Gaitzsch, M. Pötschke, S. Roth, B. Rellinghaus and L. Schultz, A 1% magnetostrain in polycrystalline 5M Ni-Mn-Ga, *Acta Mater.* **57**, 365 (2009).

[43] M. Chmielus, X. X. Zhang, C. Witherspoon, D. C. Dunand and P. Müllner, Giant magnetic-field induced strains in polycrystalline Ni-Mn-Ga foams, *Nat. Mater.* **8**, 863 (2009).

[44] J. W. Dong, J. Q. Xie, J. Lu, C. Adelmann, C. J. Palmstrom, J. Cui, Q. Pan, T. W. Shield, R. D. James and S. McKernan, Shape memory and ferromagnetic shape memory effects in single-crystal Ni_2MnGa thin films, *J. Appl. Phys.* **95**, 2593 (2004).

[45] F. Bernard, C. Rousselot, P. Delobelle, L. Hirsinger and P. Burdet, Magnetic field-induced strains in ferromagnetic shape memory alloy $Ni_{55}Mn_{23}Ga_{22}$ deposited by rf-magnetron sputtering, *Plasma Process. Polym.* **6**, S822 (2009).

[46] M. Thomas, O. Heczko, J. Buschbeck, U. K. Rössler, J. McCord, N. Scheerbaum, L. Schultz and S. Fähler, Magnetically induced reorientation of martensite variants in constrained epitaxial Ni-Mn-Ga films grown on MgO(001), *New J. Phys.* **10**, 023040 (2008).

[47] K. Bhattacharya and R. D. James, The material is the machine, *Science* **307**, 53 (2005).

[48] H. E. Karaca, I. Karaman, B. Basaran, Y. Ren, Y. I. Chumlyakov and H. J. Maier, Magnetic field-induced phase transformation in NiMnCoIn magnetic shape-memory alloys - A new actuation mechanism with large work output, *Adv. Funct. Mater.* **19**, 983 (2009).

[49] E. Warburg, Magnetische Untersuchungen, *Ann. Phys. Chem.* **13**, 141 (1881).

[50] P. Langevin, Magnétisme et théorie des électrons, *Ann. Chim. Phys. Chem.* **5**, 70 (1905).

[51] P. Debye, Some observations on magnetisation at a low temperature, *Ann. Physik* **81**, 1154 (1926).

[52] W. F. Giauque, A thermodynamic treatment of certain magnetic effects. A proposed method of producing temperatures considerably below 1° absolute, *J. Amer. Chem. Soc.* **49**, 1864 (1927).

[53] W. F. Giauque and D. P. MacDougall, Attainment of temperatures below 1° absolute by demagnetization of $Gd_2(SO_4)_3 \cdot 8H_2O$, *Phys. Rev.* **43**, 768 (1933).

[54] A. M. Tishin, Magnetocaloric effect in high magnetic field, *Cryogenics* **30**, 127 (1990).

[55] V. K. Pecharsky and K. A. Gschneider Jr., Some common misconceptions concerning magnetic refrigerant materials, *J. Appl. Phys.* **90**, 4614 (2001).

[56] V. K. Pecharsky, K. A. Gschneider Jr., A. O. Pecharsky and A. M. Tishin, Thermodynamics of the magnetocaloric effect, *Phys. Rev. B* **64**, 144406 (2001).

[57] Y. I. Spichkin and A. M. Tishin, Magnetocaloric effect at the first-order magnetic phase transitions, *J. Alloys Comp.* **403**, 38 (2005).

[58] A. A. Cherechukin, T. Tagaki, M. Matsumoto and V. D. Buchelnikov, Magnetocaloric effect in $Ni_{2+x}Mn_{1-x}Ga$ Heusler alloys, *Phys. Lett. A* **326**, 146 (2004).

[59] F. X. Hu, B. G. Shen, J. R. Sun and G. H. Wu, Large magnetic entropy change in $Ni_{52.6}Mn_{23.1}Ga_{24.3}$ single crystal, *Phys. Rev. B* **64**, 132412 (2000).

[60] L. Pareti, M. Solzi, F. Albertini and A. Paoluzi, Giant entropy change at the co-occurence of structural and magnetic transitions in the $Ni_{2.19}Mn_{0.81}Ga$ Heusler alloy, *Eur. Phys. J. B* **32**, 303 (2003).

[61] J. Marcos, A. Planes, Ll. Mañosa, F. Casanova, X. Battle, A. Labarta and B. Martinez, Magnetic field induced entropy change and magnetoplasticity in Ni-Mn-Ga alloys, *Phys. Rev. B* **66**, 224413 (2002).

[62] V. K. Sharma, M. K. Chattopadhyay and S. B. Roy, Large inverse magnetocaloric effect in $Ni_{50}Mn_{34}In_{16}$, *J. Phys. D: Appl. Phys.* **40**, 1869 (2007).

[63] Z. D. Han, D. H. Wang, C. L. Zhang, S. L. Tang, B. X. Gu and Y. W. Du, Large magnetic entropy change in the $Ni_{45.4}Mn_{41.5}In_{13.1}$ ferromagnetic shape memory alloy, *Appl. Phys. Lett.* **89**, 182507 (2006).

[64] Ll. Mañosa, M. Bou, C. Calles and A. Cirera, Low-cost differential scanning calorimeter, *Am. J. Phys.* **64**, 283 (1996).

[65] V. K. Pecharsky and K. A. Gschneidner Jr., Magnetocaloric effect from indirect measurements: Magnetization and Heat Capacity, *J. Appl. Phys.* **86**, 565 (1999).

[66] V. K. Pecharsky and K. A. Gschneidner Jr., Magnetocaloric effect and magnetic refrigeration, *J. Magn. Magn. Mater.* **200**, 44 (1999).

[67] M. Földeaki, R. Chahine, and T. K. Bose, Magnetic Measurements: a powerful tool in magnetic refrigerator design, *J. Appl. Phys.* **77**, 3528 (1995).

[68] http://www.frm2.tum.de/wissenschaft/diffraktometer/spodi/index.html

[69] http://www.ill.eu/instruments-groups/instruments/d7/characteristics/

[70] F. Mezei, Novel polarized neutron devices: Supermirror and Spin Component Devices, *Comm. on Phys.* **1**, 85 (1976).

[71] O. Schärpf, Comparison of theoretical and experimental behaviour of supermirrors and discussion of limitations, *Physica B* **156** (1989).

[72] O. Schärpf and H. Capellmann, The XYZ-Difference Method with Polarized Neutrons and the Separation of Coherent, Spin Incoherent, and Magnetic Scattering Cross Sections in a Multidedector, *Phys. Stat. Sol. A* **135**, 359 (1993).

[73] J. R. Stewart, P. P. Deen, K. H. Andersen, H. Schober, J.-F. Barthlmy, J. M. Hillier, A. P. Murani, T. Hayes, and B. Lindenau, Disordered materials studied using neutron polarization analysis on the multi-dedector spectrometer, D7, *J. Appl. Cryst.* **42**, 69 (2009).

[74] http://www.3m.com/fluids

[75] R. M. Moon, T. Riste and W. C. Koehler, Polarization analysis of thermal-neutron scattering, *Phys. Rev.* **181**, 920 (1969).

[76] B. Heinrich and J. F. Cochran, Ultrathin metallic magnetic films: magnetic anisotropies and exchange interactions, *Adv. Phys.* **42**, 523 (1993).

[77] M. Farle, Ferromagnetic resonance of ultrathin metallic layers, *Rep. Prog. Phys.* **61**, 755 (1993).

[78] J. Lindner and K. Baberschke, In situ ferromagnetic resonance: an ultimate tool to investigate the coupling in ultrathin magnetic films, *J. Phys.: Condens. Matter* **15**, R193 (2003).

[79] K. Zakeri, T. Kebe, J. Lindner and M. Farle, Temperature-dependent correlation of magnetic anisotropy and magnetization in Fe monolayers on 4x6GaAs(001), *J. Magn. Magn. Mater.* **316**, e334 (2007).

[80] M. Khan, I. Dubenko, S. Stadler and N. Ali, Magnetic and structural phase transitions in Heusler type alloys $Ni_2MnGa_{1-x}In_x$, *J. Phys.: Condens. Matter* **16**, 5259 (2004).

[81] H. C. Xuan, D. H. Wang, C. L. Zhang, Z. D. Han, H. S. Liu, B. X. Gu and Y. W. Du, The large low-field magnetic entropy changes in $Ni_{43}Mn_{46}Sn_{11-x}Sb_x$ alloys, *Solid State Commun.* **142**, 591 (2007).

[82] T. Krenke, E. Duman, M. Acet, E. F. Wassermann, X. Moya, L. Mañosa and A. Planes, Effect of Co and Fe on the incerse magnetocaloric properties of Ni-Mn-Sn, *J. Appl. Phys.* **102**, 033903 (2007).

[83] R. Kainuma, Y. Imano, W. Ito, H. Morito, Y. Sutou, K. Oikawa, A. Fujita, K. Ishida, S. Okamoto, O. Kitakami and T. Kanomata, Metamagnetic shape memory effect in a Heusler-type $Ni_{43}Co_7Mn_{39}Sn_{11}$ polycrystalline alloy, *Appl. Phys. Lett.* **88**, 192513 (2006).

[84] D. H. Wang, C. L. Zhang, H. C. Xuan, Z. D. Han, J. R. Zhang, S. L. Tang, B. X. Gu and Y. W. Du, The study of low-field positive and negative magnetic entropy changes in $Ni_{43}Mn_{46-x}Cu_xSn_{11}$ alloys, *J. Appl. Phys.* **102**, 013909 (2007).

[85] T. Krenke, X. Moya, S. Aksoy, M. Acet, P. Entel, L. Mañosa, A. Planes, Y. Elerman, A. Yucel and E. F. Wassermann, Electronic aspects of the martensitic transition in Ni-Mn based Heusler alloys, *J. Magn. Magn. Mater.* **310**, 2788 (2007).

[86] T. Krenke, M. Acet, E. F. Wassermann, X. Moya, L. Mañosa and A. Planes, Ferromagnetism in the austenitic and martensitic states of Ni-Mn-In alloys, *Phys. Rev. B* **73**, 174413 (2006).

[87] O. Söderberg, A. Sozinov, Y. Ge, S. P. Hannula and V. K. Lindros, *Handbook of Magnetic Materials*, Elsevier (2006).

[88] P. J. Brown, A. P. Gandy, K. Ishida, R. Kainuma, T. Kanomata, K. U. Neumann, K. Oikawa, B. Ouladdiaf and K. R. A. Ziebeck, The magnetic and structural properties of the magnetic shape memory compound $Ni_2Mn_{1.44}Sn_{0.56}$, *J. Phys.: Condens. Matter* **18**, 2249 (2006).

[89] W. Ito, K. Ito, R. Y. Umetsu, R. Kainuma, K. Koyama, K. Watanabe, A. Fujita, K. Oikawa, K. Ishida and T. Kanomata, Kinetic arrest of martensitic transformation in the NiCoMnIn metamagnetic shape memory alloy, *Appl. Phys. Lett.* **92**, 21908 (2008).

[90] M. K. Chattopadhyay, S. B. Roy, and P. Chaddah, Kinetic arrest of the first-order ferromagnetic-to-antiferromagnetic transition in $Ce(Fe_{0.96}Ru_{0.04})_2$: Formation of a magnetic glass, *Phys. Rev. B* **72**, 180401 (2005).

[91] P. Entel, M. E. Gruner, W. A. Adeagbo and A. T. Zayak, Magnetic-field-induced changes in magnetic shape memory alloys, *Mat. Sci. Eng. A* **481** (2008).

[92] P. J. Brown, J. Crangle, T. Kanomata, M. Matsumoto, K. U. Neumann, B. Ouladdiaf and K. R. A. Ziebeck, The crystal structure and phase transitions of the magnetic shape memory compound Ni_2MnGa, *J. Phys.: Condens. Matter* **14**, 10159 (2002).

[93] R. Ranjan, S. Banik, S. R. Barman, U. Kumar, P. K. Mukhopadhyay and D. Pandey, Powder X-ray diffraction study of the thermoelastic transition in $Ni_2Mn_{1.05}Ga_{0.95}$, *Phys. Rev. B* **74**, 224443 (2006).

[94] M. K. Chattopadhyay, V. K. Sharma and S. B. Roy, Thermomagnetic history dependence od magnetocaloric effect in $Ni_{50}Mn_{34}In_{16}$, *Appl. Phys. Lett.* **92**, 022503 (2008).

[95] J. Marcos, L. Mañosa, A. Planes, F. Casanova, X. Batlle, and A. Labarta, Multi-scale origin of the magnetocaloric effect in Ni-Mn-Ga shape memory alloys, *Phys. Rev. B* **68**, 094401 (2003).

[96] J. Deportes, B. Ouladdiaf, and K. R. A. Ziebeck, Thermal-dependence of the longitudinal spin fluctuations in YMn_2, *J. Phys. (Paris)* **48**, 1029 (1987).

[97] M. Shiga, H. Wada, Y. Nakamura, J. Deportes, B. Ouladdiaf, and K. R. A. Ziebeck, Giant spin fluctuations in $Y_{0.97}Sc_{0.03}Mn_2$, *J. Phys. Soc. of Japan* **57**, 3141 (1988).

[98] T. Freltoft, P. Böni, G. Shirane, and K. Motoya, Neutron scattering of the itinerant-electron magnet YMn_2, *Phys. Rev. B* **37**, 3454 (1988).

[99] I. Galanakis, P. H. Dederichs and N. Papanikolaou, Slater-Pauling behavior and origin of the half-metallicity of the full-Heusler alloys, *Phys. Rev. B* **66**, 174429 (2002).

[100] J. Rusz, L. Bergqvist, J. Kudrnovsky and I. Turek, Exchange interactions and Curie temperatures in $Ni_{2-x}MnSb$ alloys: First-principles study, *Phys. Rev. B* **73**, 214412 (2006).

[101] R. Y. Umetsu, R. Kainuma, Y. Amako, Y. Taniguchi, T. Kanomata, K. Fukushima, A. Fujita, K. Oikawa, and K. Ishida, Mössbauer study on martensite phase in $Ni_{50}Mn_{36.5}{}^{57}Fe_{0.5}Sn_{13}$ metamagnetic shape memory alloy, *Appl. Phys. Lett.* **93**, 042509 (2008).

[102] V. V. Khovaylo, T. Kanomata, T. Tanaka, M. Nakashima, Y. Amako, R. Kainuma, R. Y. Umetsu, H. Morito and H. Miki, Magnetic properties of $Ni_{50}Mn_{34.8}In_{15.2}$ probed by Mössbauer spectroscopy, *Phys. Rev. B* **80**, 144409 (2009).

[103] C. V. Stager and C. C. M. Campbell, Antiferromagnetic order in the Heusler $Ni_2Mn(Mn_xSn_{1-x})$, *Can. J. Phys.* **56**, 674 (1978).

[104] T. Kaneko, H. Yoshida, S. Abe and K. Kamigaki, Pressure effect on the Curie point of the Heusler alloys Ni_2MnSn and Ni_2MnSb, *J. Appl. Phys.* **52**, 2046 (1981).

[105] S. Kyuji, S. Endo, T. Kanomata and F. Ono, Pressure dependence of the Curie temperature in Ni_2MnSn Heusler alloy, *Physica B* **237**, 523 (1997).

[106] F. Albertini, J. Kamarad, Z. Arnold, L. Pareti, E. Villa and L. Righi, Pressure effects on the magnetocaloric properties of Ni-rich and Mn-rich Ni_2MnGa alloys, *J. Magn. Magn. Mater.* **316**, 364 (2007).

[107] E. Sasioglu, L.M. Sandratskii and P. Bruno, Pressure dependence of the Curie temperature in Ni_2MnSn Heusler alloy: A first-principles study, *Phys. Rev. B* **71**, 214412 (2005).

[108] Dr. M. E. Gruner, Private communication.

[109] J. Schweizer, *Polarized Neutrons and polarization Analysis*, in *Neutron Scattering from Magnetic Materials*, Ed. Tapan Chatterji, P. 153, Elsevier B. V., Amsterdam-The Netherlands (2006).

[110] O. Schärpf, *The Spin of the Neutron as a Measuring Probe*, ILL, France (1996).

Acknowledgments

I would like to thank all who have contributed to my studies in various ways.

First of all, I would like to express appreciation to Prof. Dr. M. Farle for giving me the opportunity to be a part of his research group in my doctoral study and also many thanks for beneficial discussions.

I would like to offer my sincerest gratitude to Prof. Dr. Mehmet Acet, who has supported me throughout my thesis with his patience, knowledge and friendship. I would like to thank him for giving a very interesting research topic. He provided me with constructive criticism and review at every phase of my study and guided me throughout my research.

I would like to thank Prof. Dr. E. F. Wassermann for beneficial discussions.

I would like to thank Prof. Dr. L. Mañosa and Prof. Dr. A. Planes for their friendly and supportive cooperation during my doctoral study. I would like to thank my friend Dr. X. Moya for assisting me with DSC measurements at the University of Barcelona.

It is pleasure to thank;

Dr. A. Senyshyn and Dr. J. Neuhaus at the FRM-II Forschungs-Neutronenquelle Heinz Maier-Leibnitz in Munich for their assistance with the neutron diffraction experiments and the analysis,

Dr. P. Deen at the Institute Lauve-Langevine in France for her help in the neutron polarization experiments and for the valuable discussions on the results,

Dr. M. E. Gruner for the DFT calculations and beneficial discussions,

Dr. O. Gutfleisch and Dr. J. Lyubina, for the pressure dependence of magnetization measurements,

Dr. R. Meckenstock and Dr. J. Lindner for beneficial discussions on FMR measurements,

Dipl. Phys. O. Posth, for assisting me in SEM and FMR measurements,

Dr. T. Kammermeier for his help about everything and "Deutsch stunden",

Dr. T. Krenke for continuous encouragement during my study and proofreading my german abstract,

D. Schädel for the construction of all the small and big tools and devices, Dipl. Ing. H. Zähres for valuable suggestions and discussions about the technical problems, Dipl. Ing. M. Vennemann and W. Kunze for solving technical problems.

I would like to thank to our team assistants; S. Grubba and H. Mundt, for their friendly help in all topics.

I would like to acknowledge the whole working group of Prof. M. Farle (all unnamed employees, students, Phd students, Post-Docs) for a pleasant and prolific working atmosphere.

Curriculum vitae

Name	:	Seda Aksoy	
Date/Place of Birth	:	24.07.1979/Ankara	
Nationality	:	Turkisch	
Marital Status	:	Single	

Education	:	2006-present	Ph.D candidate, Faculty of Physics University of Duisburg-Essen Duisburg, Germany
		2004-2006	M.Sc., Department of Physics Engineering Ankara University, Ankara, Turkey Thesis Titel: *"The investigation of structural and magnetic properties of $Gd_5Si_{2-y}Ge_{2-y}Ga_{2y}$ alloy"*
		1998-2003	Bachelor of Physics Engineering Department of Physics Engineering Hacettepe University, Ankara, Turkey
		02.1997	High School in Ankara

List of publications

1. **S. Aksoy**, M. Acet, A. Synyshyn, *Kinetic arrest in $Ni_{50}Mn_{34}In_{16}$ ferromagnetic shape memory alloy*, in preparation, 2009.

2. **S. Aksoy**, M. Acet, X. Moya, L. Mañosa, A. Planes, *Magnetic and magnetocaloric properties of Sn substituted $Ni_{50}Mn_{34}In_{16}$ Heusler alloy*, in preparation, 2009.

3. **S. Aksoy**, O. Posth, M. Acet, R. Meckenstock, J. Lindner, M. Farle and E. F. Wassermann, *Ferromagnetic resonance in Ni-Mn based ferromagnetic Heusler alloys*, Journal of Physics: Conference Series, **200** (2010) 092001.

4. **S.Aksoy**, M. Acet, P. Deen, L. Mañosa and A. Planes, *Magnetic correlations in martensitic Ni-Mn-based Heusler shape memory alloys: Neutron polarization analysis*, Physical Review B, **79** (2009) 212401.

5. **S. Aksoy**, M. Acet, E. F. Wassermann, T. Krenke, X. Moya, L. Mañosa, A. Planes and Pascal P. Deen, *Structural properties and magnetic interactions in martensitic Ni-Mn-Sb alloys*, Philosophical Magazine, **89** (2009) 2093.

6. X. Moya, L. Mañosa, A. Planes, **S. Aksoy**, M. Acet, E. F. Wassermann and T. Krenke, *Effect of external fields on the martensitic transformation in Ni-Mn based Heusler alloys*, Advance Material Research, **52** (2008) 189.

7. Planes, L. Mañosa, X. Moya, J. Marcos, M. Acet, T. Krenke, **S. Aksoy** and E. F. Wassermann, *Magnetocaloric and shape-memory properties in magnetic Heusler alloys*, Advance Material Research, **52** (2008) 221.

8. L. Mañosa, X. Moya, A. Planes, **S. Aksoy**, M. Acet, E. Wassermann, T. Krenke, *Magnetostrain in multifunctional Ni-Mn based magnetic shape memory alloys*, Materials Science Forum, **583** (2008) 111-117.

9. L. Mañosa, X. Moya, A. Planes, O. Gutfleisch, J. Lyubina, M. Barrio, J. Tamarit, **S. Aksoy**, T. Krenke, M. Acet, *Effects of hydrostatic pressure on the magnetism and martensitic transition of Ni-Mn-In magnetic superelastic alloys*, Applied Physics Letters, **92** (2008) 012515.

10. **S. Aksoy**, T. Krenke, M. Acet, E. F. Wassermann, X. Moya, L. Mañosa, A. Planes, *Tailoring magnetic and magnetocaloric properties of martensitic transitions in ferromagnetic Heusler alloys*, Applied Physics Letters, **91** (2007) 241916.

11. **S. Aksoy**, T. Krenke, M. Acet, E. F. Wassermann, X. Moya, L. Mañosa, A. Planes, *Magnetization easy-axis in martensitic Heusler alloys estimated by strain measurements under magnetic-field*, Applied Physics Letters, **91** (2007) 251915.

12. X. Moya, L. Mañosa, A. Planes, **S. Aksoy**, M. Acet, E. F. Wassermann and T. Krenke, *Cooling and heating by adiabatic magnetization in the $Ni_{50}Mn_{34}In_{16}$ magnetic shape-memory alloy*, Physical Review B, **75** (2007) 184412.

13. T. Krenke, X. Moya, **S. Aksoy**, M. Acet, P. Entel, L. Mañosa, A. Planes, Y. Elerman, A. Yucel and E. F. Wassermann, *Electronic aspects of the martensitic transition in Ni-Mn based Heusler alloys*, Journal of Magnetism and Magnetic Materials, **310** (2007) 2788-2789.

The following publications are not included in this thesis.

1. L. Mañosa, D. Gonzalez-Alonso, A. Planes, E. Bonnot, M. Barrio, J. L. Tamariz, **S. Aksoy**, and M. Acet, *Giant solid-state barocaloric effect in the Ni-Mn-In magnetic shape-memory alloy*, Nature Materials, accepted.

2. J. Liu, **S. Aksoy**, N. Scheerbaum, M. Acet and O. Gutfleisch, *A quarter percent of magnetostrain in polycrystalline Ni-Mn-In-Co*, Applied Physics Letter, **95** (2009) 232515.

3. Z. Liu, **S. Aksoy** and M. Acet, *Influence of Sb on the magnetic and magnetocaloric properties of ferromagnetic shape memory alloy NiMnIn*, Journal of Applied Physics, **105** (2009) 033913.

4. X. Moya, D. G. Alanso, L. Mañosa, A. Planes, V. O. Garlea, T. A. Lograsso, D. L. Schlagel, J. L. Zarestky, **S. Aksoy** and M. Acet, *Lattice dynamics in magnetic superelastic Ni-Mn-In alloys: Neutron scattering and ultrasonic experiments*, Physical Review B, **79** (2009) 214118.

5. B. Emre, **S. Aksoy**, O. Posth, M. Acet, E. Duman, J. Lindner, Y. Elerman, *Antiferromagnetic-ferromagnetic crossover in $La_{0.5}Pr_{0.5}Mn_2Si_2$ and its consequences on magnetoelastic and magnetocaloric properties*, Physical Review B, **78** (2008) 144408.

6. D. Soto, F. A. Hernandez, H. Flores, X. Moya, L. Mañosa, A. Planes, **S. Aksoy**, M. Acet, T. Krenke, *Phase diagram of Fe-doped Ni-Mn-Ga ferromagnetic shape-memory alloys*, Physical Review B, **77** (2008) 184103.

7. **S. Aksoy**, A. Yucel, Y. Elerman, T. Krenke, M. Acet, X. Moya and L. Mañosa, *The influence of gallium on the magnetocaloric properties of $Gd_5Si_2Ge_2$*, Journal of Alloys and Compounds, **460** (2007) 94.

8. A. Yucel, Y. Elerman and **S. Aksoy**, *Changes in the phase structure and magnetic characteristics of $Gd_5Si_2Ge_2$ when alloyed with Mn*, Journal of Alloys and Compounds, **420** (2006) 182-185.